EUROPEAN MECHANICAL SCIENCE

2022
VOLUME: 6
ISSUE: 2

E-ISSN: 2587-1110

"EDITOR IN CHIEF
PROF. DR. MUSTAFA ÖZCANLI"

EUROPEAN MECHANICAL SCIENCE
e-ISSN: 2587-1110

Indexed / Abstracted in:

TR-Dizin, CrossRef, Index Copernicus, Journal Factor, Rootindexing, ResearchBip, JournalFactor, JIFACTOR, Google Scholar, I2OR, Cosmos Impact Factor, International Innovative Journal Impact Factor (IIJIF), Scientific Indexing Services, InfoBase Index, Scientific Journal Impact Factor

Aims and Scopes

European Mechanical Science (EMS) is an international, peer reviewed journal which publishes full length original research papers, reviews related to all areas of Mechanical Engineering such as: Solid Mechanics, Materials Engineering, Automotive Engineering, Fluid Mechanics, Thermal Engineering, Engine and Power Engineering, Dynamics & Control, Robotics & Mechatronics, Transportation Engineering, Computational Mechanics, Design, Systems, Manufacturing, Bio-Medical Engineering; Process Engineering, Aerospace Engineering. No charges are required from the Authors to publish the articles.EMS is a quarterly published journal operating an online submission and peer review system. It allows authors to submit articles online and track their progress via its web interface.

Contents

EUROPEAN MECHANICAL SCIENCE
e-ISSN: 2587-1110

CONTENTS

EUROPEAN MECHANICAL SCIENCE
e-ISSN: 2587-1110

RESEARCH ARTICLE

Analytical investigation of a new approach to calculation for effective length of the rolling element used in closed end needle roller bearings of driveshaft

Onur Şen[1,2*], Enver Atik[2]

[1]Tirsan Kardan A.Ş., Manisa, Turkey
[2]Manisa Celal Bayar University, Mechanical Engineering Department, Manisa, Turkey

Orcid: O. Şen (0000-0001-8763-3246), E. Atik (0000-0001-8250-1957)

Abstract: The presence of oscillating motion in a mechanical system is highly critical in terms of its service life. The service life of the bearings which are one of the common machine elements is calculated according to international standard ISO 281 with the equation depending on several variables such as basic dynamic load rating (C). One of the applications where bearings are used is universal joints on the driveshafts. The bearings for universal joints (universal joint bearing) are special bearings called as closed end needle roller bearings. The rolling elements used in a universal joint bearing are the needle rollers. They have a larger contact surface when compared to the ball elements, and this makes a positive difference on the service life of the universal joint bearings. Needle roller on a universal joint bearing is supported partially along its length, unlike a needle roller used in basic applications such a round bar. Because the universal joint bearing is pressed into a housing bore on the yoke part, and the trunnions of the cross shaft which acts as an inner raceway is mounted into the bearing. In this context, the length of the needle roller supported by the trunnion of the cross shaft and housing bore, which is called effective length should be considered to compute the dynamic load rating. In this paper, an approach to determine the effective length of the rolling element used in the closed end needle roller bearing of a driveshaft has been investigated analytically. And then, the effects of the said approach on the basic dynamic load rating and bearing life have been revealed by considering ISO 281.

Keywords: Driveshaft, universal joint bearing, rolling element, needle roller, effective length, analytical investigation

1. Intorduction

One of the most common mechanical systems is the rotating systems which consist of several elements such as bearing, housing, shaft, pulley etc. And bearings play an important role in this kind of machinery systems. Determining what kind of bearing to be used is the key for the service life of the whole system and the bearing life as well. The bearings can be considered in two subdivides as ball bearings and roller bearings. The roller bearings are categorized by their ability of motion and how they operate [1]. The motion of the bearings can be handled in three ways: rotary, linear, and combined motion. An oscillating motion which is a kind of rotary motion is the result of the cyclic movement of back and forth or start and stop. One of the areas where oscillating motion is common and critical is the drivetrain components of a motor vehicle. The drivetrain is a set of interrelated components such as transmission, driveshaft, and axles which transmit the generated power to the driving wheels [2].

The universal joint which consists of two opposed yoke parts and an intermediate element (cross shaft assembly) among the yokes (Fig.1.) is a part of a driveshaft. The yokes are not parallel. But they intersect at a point. The angle among the yokes is called as operating angle. Another universal joint element, cross shaft assembly is an intermediate element located to provide a mechanical connection among the yokes which are at right angles to each other. The cross shaft assembly includes a cross shaft having four arms at the right angle to each other and four closed end needle roller bearings. Each arm of a cross shaft is supported by needle roller bearings mounted into a housing bore on the yoke part [3]. The needle roller is a kind of cylindrical roller having a smaller diameter when compared to their length [4]. Although there are five different rolling elements (balls, cylindrical rollers, spherical

* Corresponding author.
Email: o.sen@tirsankardan.com.tr

European Mechanical Science (2022), 6(2): 83-89
https://doi.org/10.26701/ems.970278
Received: July 12, 2021 — Accepted: October 18, 2021

rollers, tapered rollers, and needle rollers), the needle rollers are used in the universal joint bearings. The main reason for using needle rollers is the cyclic loading due to the oscillating motion. Because needle roller bearings have a line contact which increases the rigidity and maximum load capacity of the universal joint while the ball bearings have a single point contact which limits the strength [5]. Additionally, the needle roller is the one suitable rolling element for the universal joints when considered that the internal space of the bearing is limited [6].

The universal joint on the driveshaft rotates in oscillatory motion. And it was proved by Poncelet in early years that the rotational movement of a universal joint on a driveshaft is non-uniform [7].

The difference of the angular displacement $\Delta\phi$ between the driving yoke and the driven yoke which results from the oscillatory motion for a universal joint with an operating angle β of 15° has been computed by means of both equations below, and then illustrated in Fig. 2.

$$\tan \varphi_2 = \frac{\tan \varphi_1}{\cos \beta} \quad (1)$$

$$\Delta_\varphi = \varphi_1 - \varphi_2 \quad (2)$$

The angular displacement of the driven yoke is $\phi 2$ when the angular displacement of the driving yoke is $\phi 1$ in the equations.

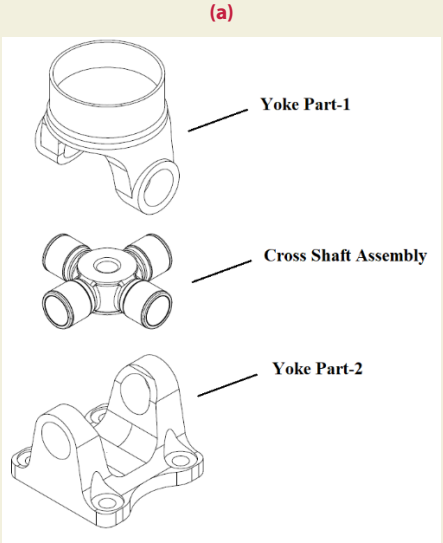

(a)

(b)

Figure 1. Typical universal joint configuration. (a) Assembled view, (b) Exploded view

The service life also known as useful life of a product is important for companies in terms of competition while it is important for end users in terms of the investment cost. Thus, a competitive manufacturer tends to improve the current service life. Therefore, the effect of the oscillating motion is vital for the service life of a universal joint bearing as well as universal joint and a driveshaft.

When the subjects of service life and optimization of bearings are reviewed in the literature, it is seen that the needle roller bearings and the ball bearings are mostly discussed and examined issues. In the literature review, it is observed that the needle roller and the cylindrical roller bearings are handled alone as an individual component without adjacent components such as a simple shaft in some papers.

Poplawski et al. (2001) investigated the effect of the roller profile on cylindrical roller bearing life prediction [8]. Basically, they took into consideration four different profiles for a rolling element: flat, tapered crown, aerospace crown and full crown profile. Different models of bearing life were chosen for this investigation: Weibull, Lundberg and Palmgren, Ioannides and Harris and Zaretsky. But in this study, only the bearing and the roller geometry were considered, not the housing bore where the bearing is mounted into.

Gupta et al. (2007) optimized the roller bearing by considering the basic static and dynamic load capacity [9]. In

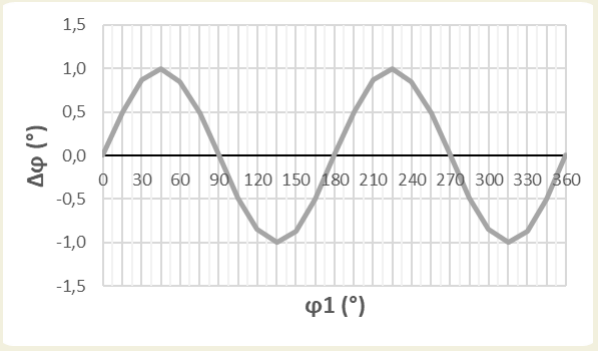

(a)

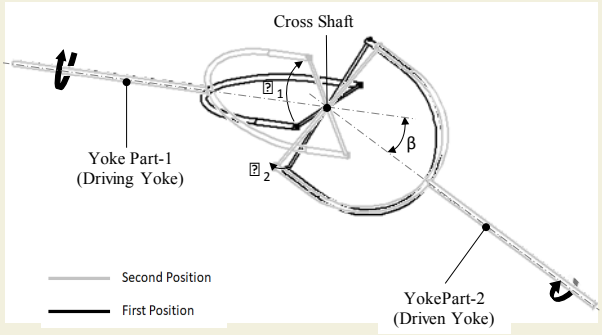

(b)

Figure 2. Angular difference Δφ between the driving and the driven yokes. (a) The difference of the angular displacement, (b) An illustration of driving and driven yokes motion

this optimization, a kind of genetic algorithm was used. The ball bearing was considered in the study.

Kumar et al. (2008) presented an optimum design procedure depending on the geometric design variables for the cylindrical roller bearings [10]. The basic dynamic load capacity calculated to reach the bearing fatigue life. The effective length of the roller is one of the variables used in the equation of basic dynamic load capacity.

Shimizu at al. (2012) developed a new life theory for the rolling bearings [11]. In the study, the effective load length was used in the formulas based on Lundberg and Palmgren for an ideal stress distribution of load rating and so service life. The rollers examined in the paper are supported by an inner and outer ring.

Oswald et al. (2014) examined the effect of the roller geometry on the service life by considering different life estimation models [12]. The rollers of the bearing used in the study are supported along its length by an inner and outer ring. Thus, effective roller length is calculated by subtracting the value of crown radius from the total length of the roller, due to its fully supported length.

Waghole et al. (2014) have optimized the dynamic capacity of the needle roller bearing by using various algorithms and a hybrid method derived from them [13]. The roller diameter, roller length, pitch diameter and number of rollers have been considered in the study. The needle rollers in the bearing subjected to the study are supported by an inner and an outer ring. Thus, the effective roller length is calculated by subtracting the value of the corner radius from the total length of the roller.

Kalyan et al. (2015) have optimized the needle roller bearings considering the long fatigue life and the wear resistance. In this context, the dynamic capacity of the bearing has been examined in terms of seven variables including effective roller length since fatigue life is related to dynamic capacity [14].

Dragoni (2016) developed an optimization procedure for tapered roller bearings by considering maximum rating life [15]. The rollers are supported by inner and outer rings as in the cylindrical rolling elements. Therefore, the effective roller length for the calculation of the dynamic load capacity can be calculated by considering the total length only and chamfers of the roller.

Panda et al. (2018) presented an optimum design approach for the rolling element bearing in their study [16]. Optimum design approach considers the multi-objective constraints for deep groove ball bearings, weight, dynamic load capacity, and minimum elastohydrodynamic film thickness.

Dandagwhal et al. (2019) proposed an approach to optimum design for both cylindrical roller bearing and deep groove ball bearing [17]. In the calculation of dynamic capacity, the effective length of the roller was obtained by subtracting the chamfer dimensions at both ends from the total length of the rolling element. Because the rollers are supported by inner and outer rings of the bearing.

The rolling elements in the bearing structures which are subjected to the studies above are supported by inner and outer rings of the bearing. Additionally, the contact surface between the rolling elements and the supporting members has full contact along the bearing length due to the structure of the bearing which consists of rollers, inner ring, and outer ring. Thus, the effective roller length used to calculate dynamic load capacity and so service life, is calculated by subtracting the corner radius or the chamfer values from the total length of the roller. But this method is inadequate for the calculation of the effective roller length and the dynamic load rating of the closed end needle roller bearing mounted into a housing bore on a yoke part of a driveshaft. Because, the housing bore where the closed end needle roller bearing is mounted, does not have a continuing cylindrical form due to the angular yoke geometry (Fig. 3). In this paper, an approach to calculation of the effective length of a closed end needle roller bearing, has been presented through a case study, to fill the gap mentioned above.

2. Methodology

The methods for calculating the bearing life considering the oscillatory motion were presented by Houpert [18], Harris [19] and ISO 281:2007 standard [20]. Each approach depends on the basic dynamic load rating which

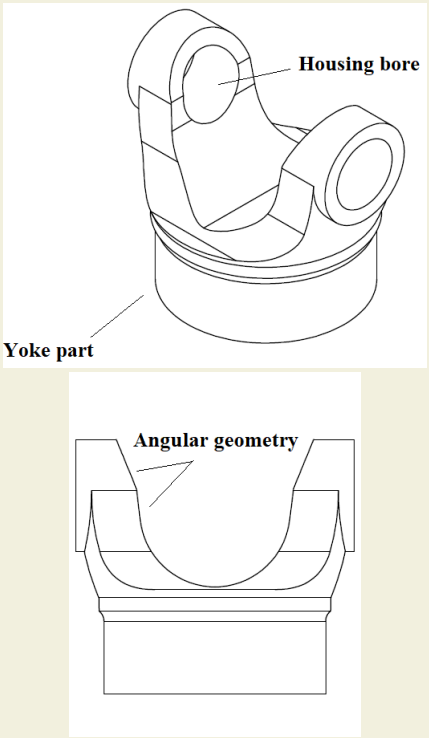

Figure 3. A yoke part and the angular housing bore geometry on the yoke part

is an expression of the load allowing 1 million revolutions before any fatigue failure is developed on the bearing elements. It is merely a radial load for the needle roller bearings. The dynamic load rating of the rolling bearings which affects the service life is defined in ISO 281:2007. The basic dynamic load rating and the basic rating life for the needle roller bearings can be calculated by the Eq. (3) and Eq. (4) below [20].

$$C_r = b_m f_c (i L_{we} \cos\alpha)^{7/9} z^{3/4} D_{we}^{29/27} \quad (3)$$

$$L_{10} = \left(\frac{C_r}{P_r}\right)^{10/3} \quad (4)$$

According to the Eq. (3), basic dynamic load rating for a radial load C_r depends on rating factor b_m (which varies with bearing type and design), bearing coefficient f_c, number of rows of rolling elements i, effective roller length L_{we}, nominal contact angle α (zero for needle roller bearings in driveshafts), number of rolling elements per row z and roller diameter D_{we} while L_{10} and P_r are respectively designated for basic rating life giving a 90 percent reliability, and equivalent radial load on the bearing in Eq. (4).

Table 1 and Table 2 are used to obtain the values of bm and fc in the radial roller bearings. Table 1 gives the value of bm for the relevant bearing type such as drawn cup, cylindrical and spherical rollers. Table 2 gives the maximum value of fc, as the value corresponding to $(D_{we} \cos\alpha)/D_{pw}$. Here, D_{pw} is pitch diameter of roller set which is calculated by Eq. (5). D_{we} and D_t are respectively the diameter of the rolling element and the trunnion diameter of the cross shaft.

$$D_{pw} = D_{we} + D_t \quad (5)$$

It is obvious that the dynamic load rating directly depends on the effective roller length L_{we} as it can be understood from the Eq. (3).

Table 1. Values of bm for radial roller bearings [20]

Bearing Type	b_m
Drawn cup needle roller bearings	1,00
Cylindrical roller bearings, tapered roller bearings and needle roller bearings with machined rings	1,10
Spherical roller bearings	1,15

Table 2. Maximum values of fc for radial roller bearings [20]

$\frac{D_{we}\cos\alpha}{D_{pw}}$	f_c	$\frac{D_{we}\cos\alpha}{D_{pw}}$	f_c	$\frac{D_{we}\cos\alpha}{D_{pw}}$	f_c
0,01	52,1	0,11	85,4	0,21	88,5
0,02	60,8	0,12	86,4	0,22	88,2
0,03	66,5	0,13	87,1	0,23	87,9
0,04	70,7	0,14	87,7	0,24	87,5
0,05	74,1	0,15	88,2	0,25	87,0
0,06	76,9	0,16	88,5	0,26	86,4
0,07	79,2	0,17	88,7	0,27	85,8
0,08	81,2	0,18	88,8	0,28	85,2
0,09	82,8	0,19	88,8	0,29	84,5
0,10	84,2	0,20	88,7	0,30	83,8

The rolling elements in the closed end needle roller bearing are supported by the housing bore on the yoke part, and the trunnion of the cross shaft. Therefore, unlike the rolling elements in a bearing with an inner and an outer ring on a straight shaft, the rolling elements in the needle roller bearing used on a driveshaft are not supported along their lengths. In universal joints, taking the total length of the rolling element as the effective roller length misleads the calculation of the dynamic load rating. An approach which handles the effective roller length from a different viewpoint has been developed to fill this gap. The difference between the effective roller length obtained with the current calculation regardless of housing bore geometry and the effective roller length obtained with the said approach considering the housing bore geometry has been demonstrated and compared to each other in terms of the calculation of dynamic load rating for the closed end needle roller bearing.

2.1. Calculation of the dynamic load rating: regardless of the geometry of housing bore

Basically, the calculation below can be implemented to determine the effective length of the roller by only considering the closed end needle roller bearing. In this method, the housing bore which supports the closed end needle roller bearing is not considered. For the calculation, a closed end needle roller bearing has been sectioned along a plane passing through the center of the bearing (Fig. 4).

The effective roller length L_{we} is calculated by considering four parameters, respectively the length of the trunnion L_w and the radius r at the corner of rolling element, the number of the rows of rolling elements i and the thickness

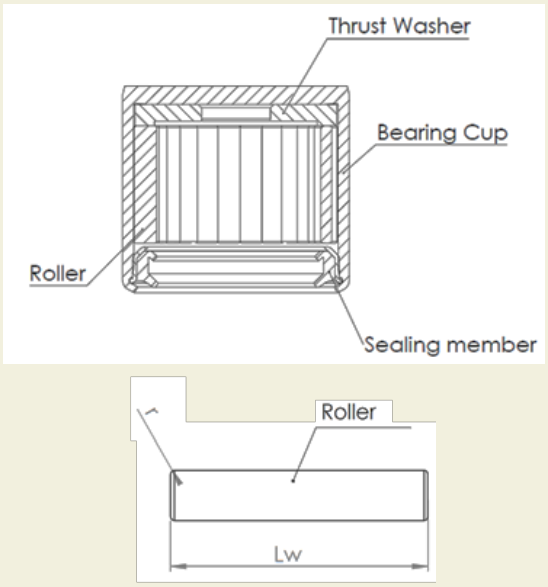

Figure 4. Cross sectioned view of the closed end needle roller bearing

of the washer t used between two rows, Eq. (6).

$$L_{we} = L_w - (2\,i)\,r - (i-1)\,t \quad (6)$$

2.2. New calculation of the dynamic load rating: depending on the housing bore geometry

The needle roller bearing is mounted into a housing bore on the yoke part of the driveshaft. The moment on the driveshaft results in a radial force on the yoke part, housing bore (Fig.5) and roller bearing (Fig.6).

Figure 5. Illustration of (a) driveshaft assembled view, (b) the radial force acting on the yoke part

The housing bore and the closed end needle roller bearing have been investigated by sectioning along the plane which is through the center of the housing bore and parallel to the radial force (Fig. 6). The relationships among the sub-components of the closed end needle roller bearing, and between the closed end needle roller bearing and housing bore have been analyzed by means of the view of Detail H in Fig. 6.

The contact surfaces between the housing bore and the bearing have been revealed with a cross-section given by Detail-H in Fig. 6. The closed end needle roller bearing is supported by the housing bore. It is an important constructive point, and the key which should be considered for the calculation of the effective roller length L_{we}. Thus, intersection length L_i of projections of the trunnion and housing bore is one of the parameters to be used in the calculation of L_{we} in the approach.

Thrust washer have U-shaped cylindrical geometry. Its center is in contact with the trunnion end face while the protrusion of its U-shaped geometry is in contact with the rolling element's end face. Thus, the height of the trust washer h which is relative to the trunnion end should be considered as well for the calculation of the effective roller length L_{we} in the said approach.

In addition to the parameters h and L_i, the radius r at the corner of the rolling element is another parameter affecting the effective roller length because the radius shortens the roller length supported by the housing bore.

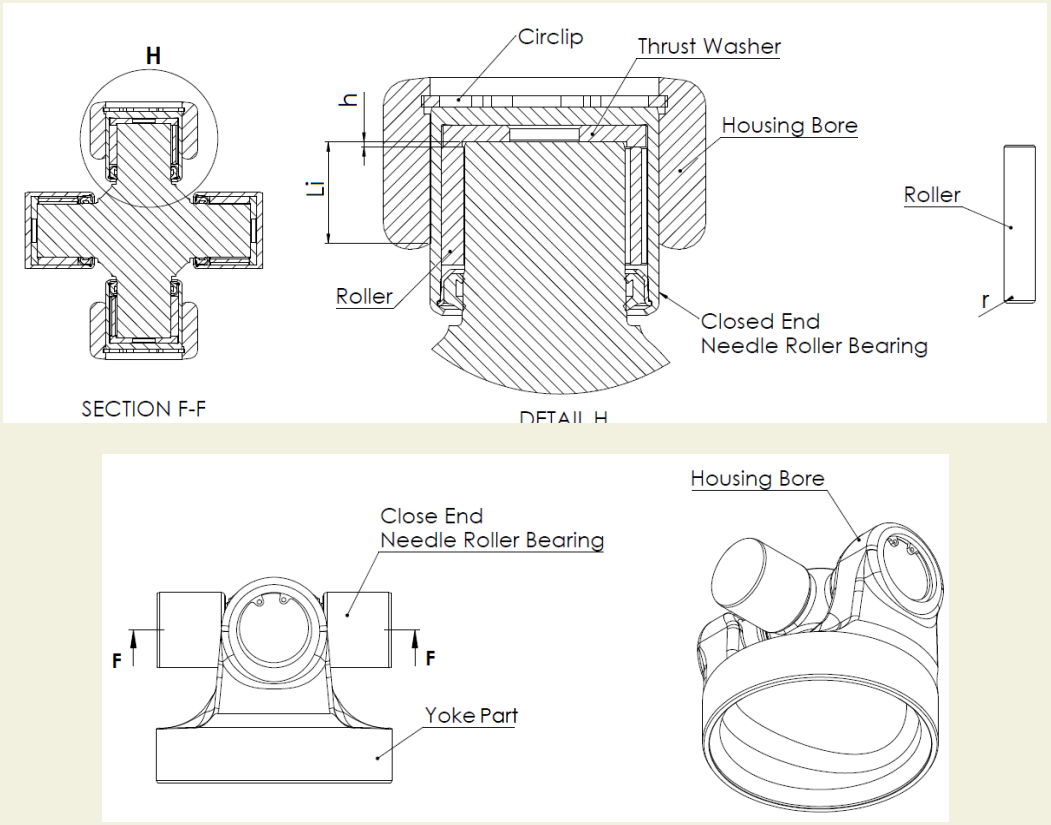

Figure 6. Cross sectioned view of the assembly (closed end needle roller bearing, cross shaft and yoke part)

Consequently, effective roller length L_{we} has been obtained by the Eq. (7):

$$L_{we} = L_i - h - (2\,i - 1)\,r - (i - 1)\,t \quad (7)$$

In the equation, the number of the rows for the rolling elements i has been included in the equation in case the needle roller bearing may consist of multiple rows. Depending on the usage of multiple rows, a washer may be used between two rows. In this situation, the thickness of the washer t has been included in the equation.

3. Results

In this section, dynamic load rating of the closed end needle roller bearing has been calculated as a case study, by using the presented approach and the existing calculation. Just after, the basic rating life has been calculated to reveal the effect of the presented approach on the estimated bearing life.

The data used in the calculations, which are based on the case study have been given in Fig. 7. The needle roller bearing includes 1 row and 25 rolling elements.

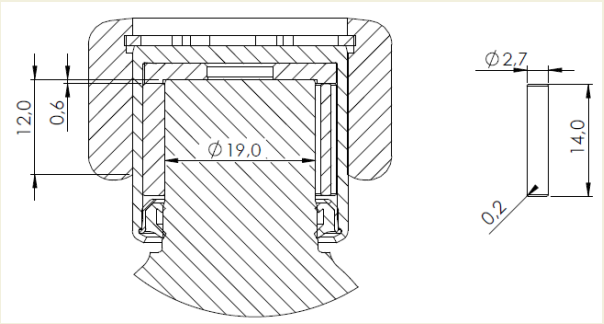

Figure 7. The data of assembly group and the needle roller

3.1. Results of the calculation regardless of geometry of the housing bore

This method in which the housing bore supporting the closed end needle roller bearing is not considered, uses Eq. (6) to calculate the effective roller length. The inputs required for Eq. (6), have been taken from Fig.7. And so, the effective roller length has been calculated as below.

$$L_{we} = L_w - (2\,i)\,r - (i - 1)\,t \quad (6)$$

L_{we}= 13,6 mm

The basic dynamic load rating has been calculated by Eq. (3).

$$C_r = b_m\, f_c\, (i\, L_{we} \cos\alpha)^{7/9}\, Z^{3/4}\, D_{we}{}^{29/27} \quad (3)$$

b_m has been obtained as 1,00 for the drawn cup needle roller bearings on Table 1., and f_c has been obtained from Table 2. The other values have been taken from Fig.7. All values have been substituted in the Eq. (3). As a result, C_r is obtained as below.

C_r = 21,4 kN

Basic rating life can be calculated in terms of millions of revolutions by using the Eq. (4) for the equivalent bearing load of 8 kN.

$$L_{10} = \left(\frac{C_r}{P_r}\right)^{10/3} \quad (4)$$

L_{10} = 26,8 M rev.

3.2. Results of calculation according to the presented new approach

The new approach considering that the rolling elements of the closed end needle roller bearing are supported by both the housing bore and the trunnion of the cross shaft uses Eq. (6) to calculate effective roller length. The inputs required for the Eq. (6), have been taken from Fig.7. And so, the effective roller length has been calculated as below.

$$L_{we} = L_i - h - (2\,i - 1)\,r - (i - 1)\,t \quad (6)$$

L_{we}= 11,2 mm

The basic dynamic load rating has been calculated by Eq. (3).

$$C_r = b_m\, f_c\, (i\, L_{we} \cos\alpha)^{7/9}\, Z^{3/4}\, D_{we}{}^{29/27} \quad (3)$$

b_m has been obtained as 1,00 for the drawn cup needle roller bearings on Table 1., and f_c has been obtained from Table 2. The other values have been taken from Fig.7. All values have been substituted in Eq. (3). Finally, C_r is obtained as below.

C_r = 18,4 kN

Basic rating life can be calculated in terms of millions of revolutions, by using the Eq. (4) for the equivalent bearing load of 8 kN.

$$L_{10} = \left(\frac{C_r}{P_r}\right)^{10/3} \quad (4)$$

L_{10} =16,2 M rev.

4. Discussion

The effect of the presented approach on the dynamic load rating and, also the bearing rating life is shown in Fig. 8 by the comparison. If we consider both results respectively, it has been observed that:

1. The effective roller length which is required for the calculation of dynamic load rating according to ISO 281 varies depending on the calculation method. The new approach considering the housing of the yoke part of the driveshaft gives a more effective roller length compared to the current method.
2. The new approach gives the higher dynamic load rating which is calculated according to ISO 281.
3. It is obvious that the current method gives the lower service life which is calculated according to ISO 281 when compared with the new method.

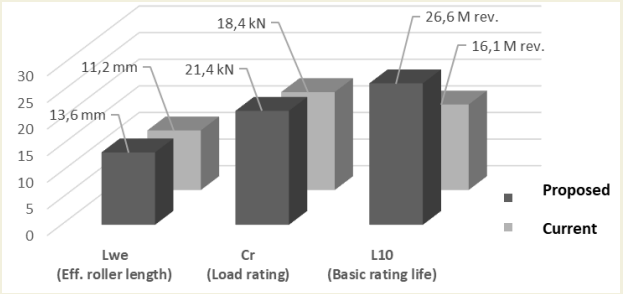

Figure 8. The effect of the new approach on the dynamic load rating and bearing life

5. Conclusions

In the driveshaft, the rolling elements of the closed end needle roller bearings are supported by the housing bore on the outside and cross shaft trunnion on the inside. The housing bore on the yoke part has an angular end because the yoke part of the driveshaft has an angular geometry. Therefore, unlike the rolling elements in the bearing with an inner and an outer ring, the rolling elements in the closed end needle roller bearing of driveshaft are not supported along their length. But the total length of the roller element is considered in the calculation of the effective roller length. In this context, a new approach handling the effective length of the rolling element from a different viewpoint has been developed to fill this gap.

The basic dynamic load rating has been calculated by using the formulation provided from ISO 281 to reveal the differences between both methods. Two different methods have been used in the calculation of the effective roller length and so the dynamic load rating. The new approach considers the housing bore geometry while the other ignores it.

The calculated dynamic load ratings by both methods, have been compared to each other. As a result of this study, it is obvious that the dynamic load rating obtained by the proposed approach is 14% lower than the other calculation method. Additionally, considering the feedbacks from the field, it is pointed out that the service life of the closed end needle roller bearing was higher than the estimated value by the current calculation. In this situation, considering the effective roller length as the total length of the roller in the universal joints misleads the calculation of the dynamic load rating. Therefore, the presented approach is suggested for the calculation of the dynamic load rating as well as service life of the closed end needle roller bearing used in the driveshaft.

6. References

[1] Jat, A., Tiwari, R. (2020). Multi-objective optimization of spherical roller bearings based on fatigue and wear using evolutionary algorithm. Journal of King Saud University-Engineering Sciences, 32: 58-68.

[2] Bauer, H., Cypra, A., Beer, A. (1993). Automotive Handbook, 3rd ed. Robert Bosch GmbH, Stuttgart.

[3] Heisler, H. (2002). Advanced Vehicle Technology, Butterworth, Heinemann, Oxford.

[4] Shinde, D.S., Solanki, P.M., Chaudhari, J.R. (2013). Wear Analysis of U- Joint Needle Bearing. International Journal of Science, Environment and Technology, 2(2): 162-167.

[5] Harris, P.M., Kotzalas, M.N. (2006). Essential Concepts of Bearing Technology, CRC Taylor & Francis, New York.

[6] Lazovic, T., Marinkovic, A., Markovic, S. (2012). Mathematical Background of U-joint Repair. IFAC Proceedings Volumes, 45(2): 1249-1253.

[7] Seherr-Thoss, H.Chr., Schmelz, F., Aucktor, E. (2006). Universal Joints and Driveshafts, Springer-Verlag, Berlin.

[8] Poplawski, J.V., Peters, S.M., Zaretsky, E.V. (2001). Effect of Roller Profile on Cylindrical Roller Bearing Life Prediction-Part II Comparison of Roller Profiles. Tribology Transactions, 44(3):417-427.

[9] Gupta, S., Tiwari, R., Nair, S.B. (2007). Multi-Objective Design Optimization of Rolling Bearings Using Genetic Algorithms. Mech. Mach. Theory, 42(2):1418-1443.

[10] Kumar, S.K., Tiwari, R., Reddy, R.S. (2008). Development of an Optimum Design Methodology of Cylindrical Roller Bearing Using Genetic Algorithm. Int. J. Comput. Methods Eng. Sci Mech, 9(6):321-41.

[11] Shimizu, S., (2012). A New Life Theory for Rolling Bearings by Linkage between Rolling Contact Fatigue and Structural Fatigue. Tribology Transactions, 55:558-570.

[12] Oswald, F.B., Zaretsky, E.V., Poplawski J.V. (2014). Effect of Roller Geometry on Roller Bearing Load–Life Relation. Tribology Transactions, 57(5):928-938.

[13] Waghole, V., Tiwari, R. (2014). Optimization of Needle Roller Bearing Design Using Novel Hybrid Methods. Mechanism and Machine Theory, 72:71-85.

[14] Kalyan, M., Tiwari, R. (2016). Multi-Objective Optimization of Needle Roller Bearings Based on Fatigue and Wear Using Evolutionary Algorithm. Proceedings of the Institution of Mechanical Engineers, Part J: Journal of Engineering Tribology, 230(2):170-185.

[15] Dragoni, E., (2017). Optimal Design of Tapered Roller Bearings for Maximum Rating Life under Combined Loads. Mechanics & Industry, 18(1).

[16] Panda, S., Panda, S.N. (2018). A Multi Objective Optimum Design Approach for Rolling Element Bearing. Int. J. Interact Des. Manuf., 12:1095-1108.

[17] Dandagwhal, R.D., Kalyankar, V.D. (2019). Design Optimization of Rolling Element Bearings Using Advanced Optimization Technique. Arab J Sci Eng., 44:7407-7422.

[18] Houpert, L. (1999). Bearing Life Calculation in Oscillatory Applications. Tribology Transactions, 42:136-143.

[19] Harris, T.A., Rumbarger, J.H., Butterfield, C.P. (2009). Wind Turbine Design Guideline: Yaw and Pitch Rolling Bearing Life. Technical Report NREL/TP-500-42362. Colorado, USA.

[20] International Organization for Standardization (2007). Rolling Bearings—Dynamic Load Ratings and Rating Life, ISO 281:2007.

EUROPEAN MECHANICAL SCIENCE
e-ISSN: 2587-1110

RESEARCH ARTICLE

FEA analysis and optical measurement of city bus composite floor structure

Mislav Tujmer[1], Franjo Tadić[2], Ana Pilipović[1], Petar Ilinčić[1*]

[1]University of Zagreb, Faculty of Mechanical Engineering and Naval Architecture; Croatia;
[2]Novatec d.o.o.; Croatia;

Orcid: M. Tujmer (0000-0003-1060-6973), F. Tadić (0000-0002-8546-9101), A.Pilipović (0000-0003-1330-6458), P. Ilinčić (0000-0003-4354-6188)

Abstract: Polymer composites have various application in a automotive industry. Achieving vehicle efficiency in public transportation, among other goals, is often done by lightweight materials like fibre reinforced plastics as structural elements of the vehicle. A concept solution for a V shaped structural floor element of a city bus is proposed in this paper. CAD model of floor structural element has been designed from which, in later phases, construction of complete composite floor will be optimized and designed. Test sample made of hybrid (carbon and glass) fibre composite was produced and tested under the flexural load for comparison with a FEA model. Test sample displacement was measured using a GOM Tritop optical measurement system. Comparison showed that difference between real measurement and FEA for maximal displacement is only 11.7%.

Keywords: carbon fibre, flexural displacement, FEM, glass fibre, hybrid composites, optical measurement

1. Introduction

Weight reduction and improvement in efficiency in public transport vehicles can be achieved with the application of composite materials. Composite materials are widely used for parts of the interior such as passenger seats[1] or side walls [2] but also they can be used for structural elements of the vehicle body such as side panels and superstructure profiles [3,4]. Potential to reduce weight in the chassis has been recognized by several leading bus manufactures in the last few decades [5,6].

Penetration of electric drive systems, driven by environmental concerns, results in additional weight of the vehicles due to battery systems having relatively low specific energy capacities. Possible solution to that challenge is a complete composite monocoque chassis in addition to other composite parts[7,8]. Additionally, application of lightweight composite materials in electric vehicles could improve performance in terms of vehicle range and battery size containment [9]

Such an approach has been used in the development of a modular electric low floor city bus. In this paper, concept of lightweight composite structure as a part of vehicle superstructure is considered in which conventional steel frame floor structure was replaced with the hybrid composite material (Figure 1). As a part of the design process application of modern measuring techniques like optical measuring was used for verification of CAD design and FEM calculation results.

2. Methods

2.1. V-shaped structural element model

Proposed lightweight composite vehicle floor, as a part of the supporting structure, consists of an upper and a lower plate which are joined by V-shaped structural elements that form a honeycomb-shaped reinforcement as shown in Figure 2.

Design of structural element in V-shape was chosen because it enables different ways of forming the entire structure and allowing various profile combinations to be considered in the following design stages. For such profile, first, a CAD model was made, which was also used for FEM calculations (Figure 3). FEM analysis was made in *Autodesk Inventor Professional 2022*. For analysis, following boundary conditions in the supports were used: only rotation in the x-axis direction is allowed, while other are constrained. Regarding translations, one support was set as fixed, and another allows translation in the z-axis. Material was set as isotropic and five different load cases (from 200 to 1000 N) were analysed.

In this early phase of design, the properties of only that

* Corresponding author.
Email: petar.ilincic@fsb.hr

European Mechanical Science (2022), 6(2): 90-96
https://doi.org/10.26701/ems.1060138
Received: Januray 19, 2022 — Accepted: April 13, 2022

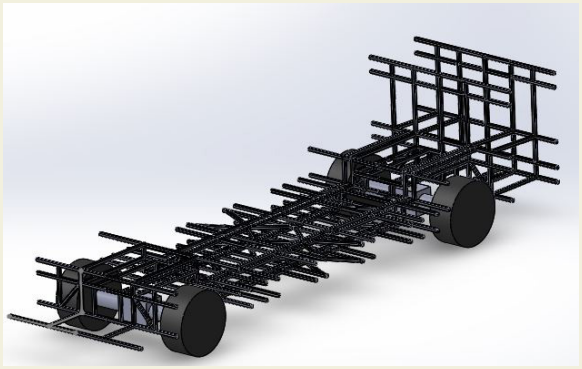

a)

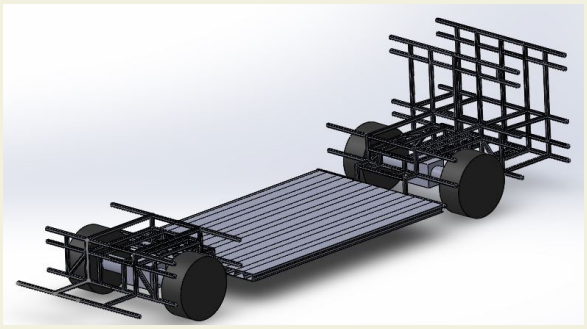

b)

Figure 1. Conventional steel frame (a) and composite passenger carrying module (b)

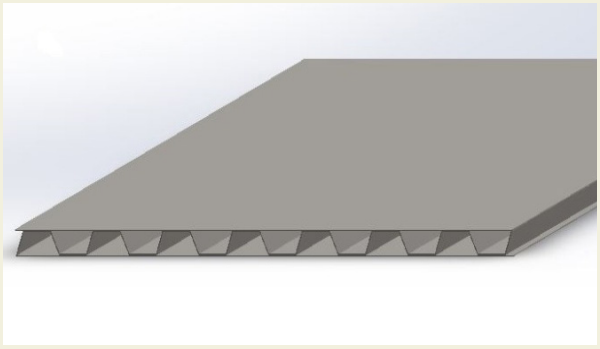

Figure 2. Floor panel with V shaped structural floor element

one element will be analyzed, and in the later phases, the design of that element and the entire composite floor will be optimized to obtain the appropriate strength and rigidity with the lowest mass possible. In addition to the design, in the process of optimization, as influencing factors type of composite, stacking and thickness of the composite will be considered.

2.2. Profile production

Glass fibre composites, due to the relatively low cost, are commonly used for production of vehicle body parts, while the carbon fibre composites are used for the parts requiring high strength-to-weight ratio and rigidity. Hybrid composite made of glass and carbon fibre can be an optimal solution due to appropriate mechanical properties and acceptable costs.

Such hybrid approach was also applied for production

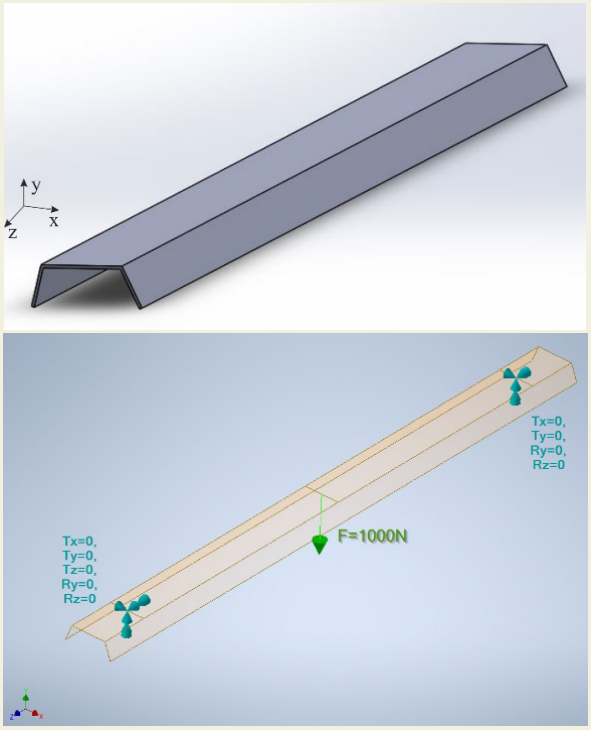

Figure 3. V shaped structural floor element CAD (left) and FEM model (right)

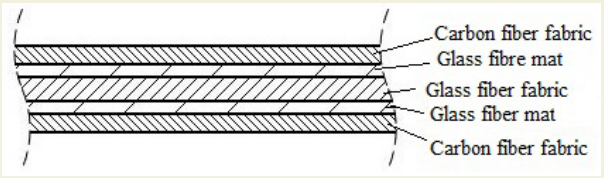

Figure 4. Structure of the profile laminate

of V shaped structural element (profile), where polyester resin reinforced with 5 layers of biaxial carbon fibre and three-axial glass fibre woven fabric and a glass mat were used. Hand lay up lamination has been chosen as a production method for economical and practical reasons. Lay-up of a hybrid laminate is shown in Figure 4. The outer layers of the laminate are carbon fabric, and the middle is glass fabric, while two layers between the outer fabric and the middle layer are made of glass mat.

Metal mould was used for the production of specific V shape. Thickness of the laminate structure was around 3 mm. Due to technological reasons and resin wet lay up time (45 min), production length of the profile was 2000 mm, width 150 mm and height 50 mm. From the end part of the profile, in length of 250 mm, samples for flexural tests were machined. Final length of the profile was 1750 mm. Production process and finished profile are shown in Figure 5.

2.3. Measurement method

Optical measurement methods are used for deformation and displacement measurements on a large scale objects made from composite materials [11,12]. As they offer non-destructive, practical, and precise measurements they

a)

b)

Figure 5. Production process (a) and finished profile (b) [10]

are applicable for evaluation of parts behaviour as well as quality control.

Optical measurement method was used to determine the behaviour of the profile under the load. Steel weights were used to simulate the load generated by passenger standing in the centre of the profile, while the profile was supported at the ends by two supports. The test set up was constructed to be similar to the mechanical model of a beam with two supports to enable the verification of the obtained results by the analytical method. GOM Tritop optical measurement system was used for measurements. Test procedure was carried out with the progressive load in 5 stages (200, 400, 600, 800 and 1000 N) while the unloaded state was used as reference.

GOM Tritop system uses triangulation principle to determine the coordinates of the measurement points glued on the object (black and white round stickers shown in Figure 6). The position and size of the object is defined with reference points (coded points) on scale bars and reference crosses. Using a photogrammetric camera GOM software creates a cloud point for each load stage and can compare the displacement of the points. Camera focal length is constant for each stage while the effect of the environment temperature (22 °C) is taken in account in pre-measurement set up and calibration process before each stage.

2.4. Determination of flexural properties

Flexural properties required for analytical and numerical evaluation have been determined by the three point

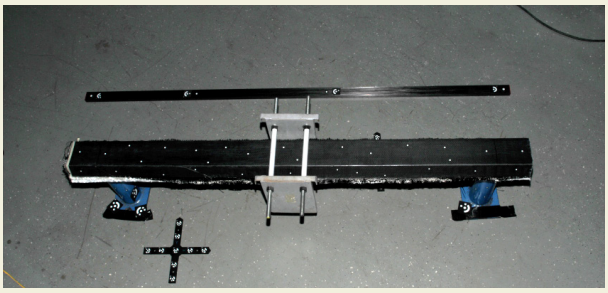

Figure 6. Measurement test set up (load of 200 N)

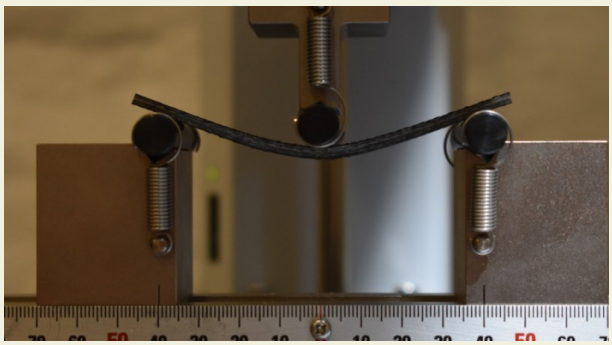

Figure 7. Flexural testing of the hybrid composite test specimen

flexural test on a *Shimadzu AGS-X* universal testing machine in accordance with the standard HRN EN ISO 14125:2005 [13]

Testing procedure, shown in Figure 7, was carried out at 23 °C and 49 % humidity. Testing speed was 2 mm/min, support rollers radius was R_2= 5+/-0,2 mm and pressure roller radius R_1= 5+/-0,2 mm. Distance between support rollers was L = 80 mm. In total 4 test specimens were machined from the profile and tested to determine flexural modulus needed in analytical and numerical calculations. Dimension of the test specimen was from standard 100 x 15 x 4 mm.

3. Results and Discussion

After all measurements with different loads were done, measurement data was analysed by *GOM TRITOP Professional V7.5 SR2* software. From analysed, dependence of the vertical displacement in the middle of the profile on the applied force was obtained. Vertical displacement distribution on the profile under series of loads are analysed after the measurement and shown in Figures 8-12.

For every load case measured with optical measurement system, FEM calculation with the same boundary conditions was made. Simplified mechanical model with a concentrated vertical force was used to describe load behaviour of a passenger standing in the middle of the profile. Since vehicle structure is still in early design phase additional loads could not be taken in account, but all assumptions made are overestimation of sort and re-evaluation of the concept is expected to have better results in terms of mechanical response of the floor structure as a whole. Although real measurements are taken with

Figure 8. Displacement distribution under the 200 N load measured with *GOM Tritop*

Figure 9. Displacement distribution under the 400 N load measured with *GOM Tritop*

Figure 10. Displacement distribution under the 600 N load measured with GOM Tritop

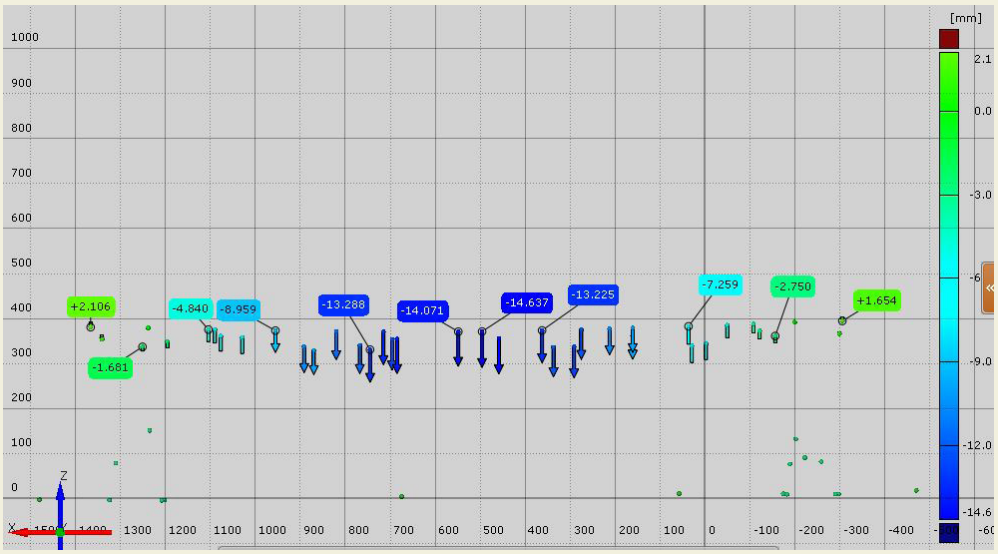

Figure 11. Displacement distribution under the 800 N load measured with GOM Tritop

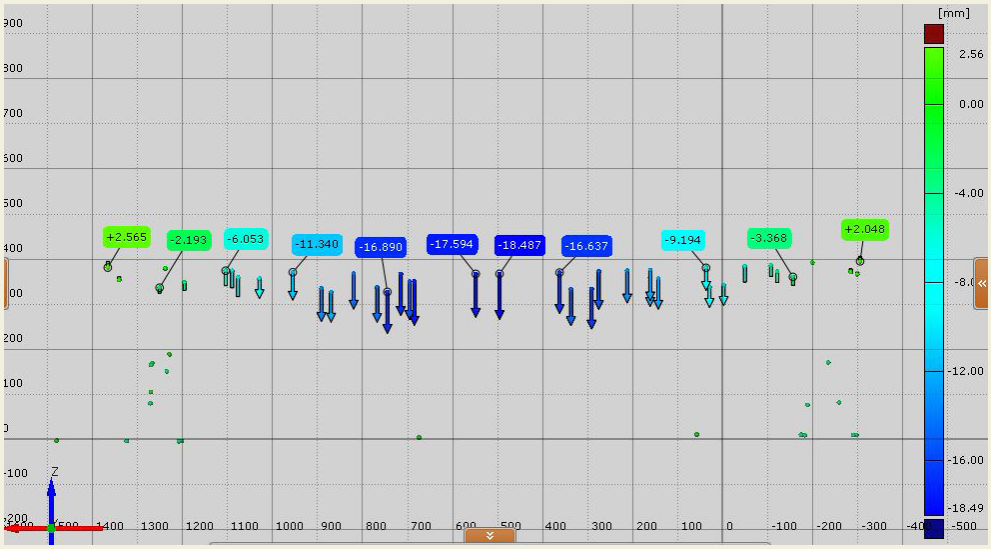

Figure 12. Displacement distribution under the 1000 N load measured with GOM Tritop

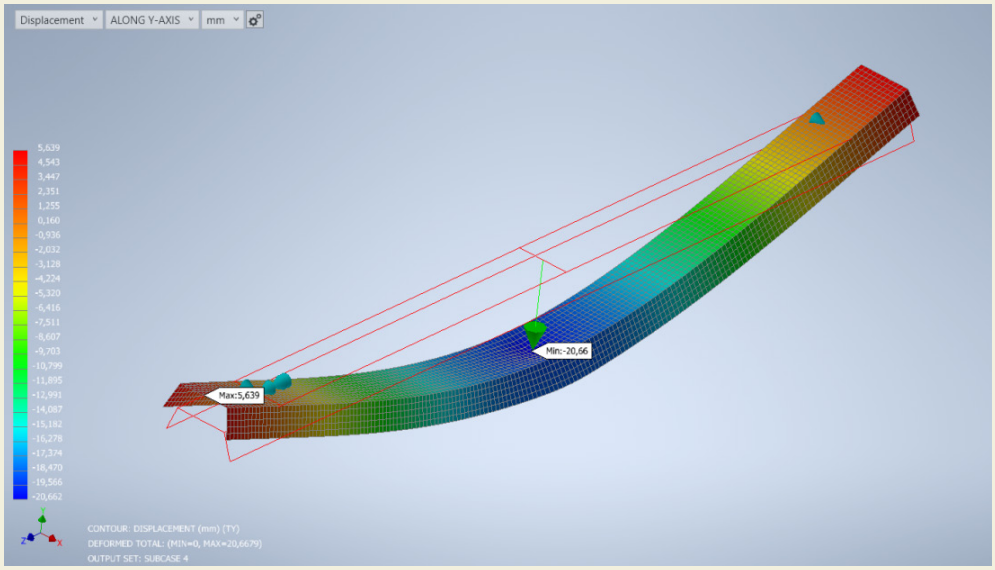

Figure 13. Displacement distribution in FEM under the 1000 N load

weights with two struts for practical reasons there is a neglible difference between the case in reality and one concentrated force used for FEM model. Vertical displacement distribution on the profile under the load of 1000 N calculated with the FEM is shown in Figure 13. From the figures, it can be concluded that both forms of distribution show the shape of a conventional distribution of displacement in a beam with two supports which was expected. In both cases, the results of the vertical displacement along the profile between the support match relatively well. Only deviation in the vertical displacement occurs at overhangs at the ends of the profile, which may occur due to the support difference in the real profile and the FEM model.

As a final part of result analysis, both, measurement, and FEM method were compared with the analytical values calculated by conventional engineering methods using equation:

$$w = \frac{F \cdot L^3}{48\, E_f\, I} \tag{1}$$

Where: F – force load, N
L – profile length, mm
E_f – flexural modulus, N/mm^2
I – moment of inertia, mm^4

Length of profile beam between supports was 1500 mm. Moment of inertia of 168,867 mm^4, determined from the CAD model and flexural modulus of 23,119.7 N/mm^2, as a mean of measured values, were used for calculations. The results of the flexural modulus of all four test specimens with mean value and standard deviation are shown in Table 1.

Table 1. Flexural modulus results

No.	Flexural modulus, N/mm^2
1	23,798.6
2	22,766.1
3	23,179.9
4	22,734.0
	23,119.7
S	496.1

Table 2. Vertical displacement values results

Load F [N]	Vertical displacement w, mm			Deviation to measurement, %	
	Measurement	FEM	Analytical	FEM	Analytical
0	0.00	0.00	0.00	0.00	0.00
200	4.43	4.13	3.60	-6.77	-18.74
400	7.83	8.27	7.20	5.62	-8.05
600	11.55	12.4	10.81	7.36	-6.41
800	14.50	16.5	14.41	13.79	-0.62
1000	18.49	20.66	18.01	11.74	-2.60

Vertical displacement results as a function of force, measured with *GOM Tritop* optical system, calculated with FEM and analytical method are given in Table 2 and shown in Figure 14.

Comparing the results of FEM analysis and measurement it can be concluded that the FEM model is on the safety side, since the calculated displacements are higher than measured (except for the 200 N load). In that sense, real composite beam is stiffer than the calculated with the FEM.

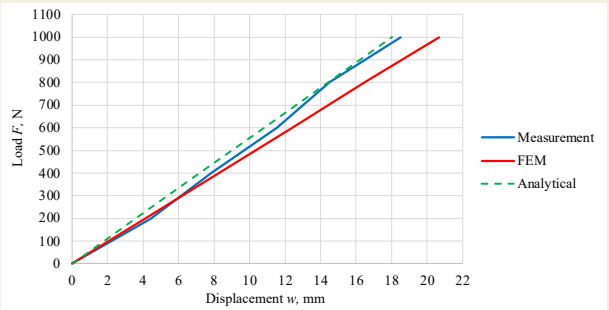

Figure 14. Load-displacement diagram

4. Conclusion

Optical measurement has shown to be reliable method to evaluate mechanical behaviour of structures which is a great advantage at an early stage of the product development. This analysis also showed that lightweight composite materials can be used as structural elements in vehicle design. Real displacement values range between analytical and numerical values which confirms that FEM calculations as well as optical measurement methods are reliable.

Displacement values, measured by optical measurement method, differ slightly from the values calculated with FEM and analytical methods. Comparison showed that the difference in results between real measurement and FEM calculation in vertical displacement under the maximal load is only 11.7%. Precision of methods and calculations as well as assumptions regarding the isotropy of the materials made for FEM can be potential cause of these differences.

5. Acknowledgements

This research was made within the project KK.01.2.1.02.0071 Development of a multifunctional low floor vehicle – MUNIVO, funded by the European Regional Development Fund.

6. References

[1] Bartus, S., Vaidya, U., Ulven, C. (2006). Design and development of a long fiber thermoplastic bus seat. Journal of Thermoplastic Composite Materials, 19(March): 131–154, 10.1177/0892705706062184.

[2] https://www.lamilux.com/composites/branches/bus-in-

dustry.html., consulted 14.9.2021.

[3] Mary Lou Jay (2020). Composites power efficiency in electric buses. Composite Manufacturing Magazine, May 2020. http://compositesmanufacturingmagazine.com/2020/05/composites-power-efficiency-in-electric-buses/., consulted 15.9.2021.

[4] Neves, P. C., Ferreira, A. J. M. & Fernandes, A. A. (2010). Litebus - Modular Lightweight Sandwich Bus Concept. Consulted 15.9.2021.

[5] https://www.proterra.com/timeline-event/the-ecoride/ consulted 15.9.2021..

[6] https://de-academic.com/dic.nsf/dewiki/1009300.consulted 15.9.2021.

[7] Dawson, D. (2018). A clean technology for clean zero emission-buses. Composites World, October 2018., https://www.compositesworld.com/articles/a-clean-technology-for-clean-zero-emissions-buses, consulted 16.9.2021.

[8] Testoni, O., Concept And Preliminary Design of A Composite Monocoque For An Electric City-Bus, Master Thesis Eth Zurich, 2015., Https://Doi.org/10.3929/Ethz-A-010559727

[9] Delogu, M. P. M., Zanchi, L., Dattilo, C.a. (2017). Innovative composites and hybrid materials for electric vehicles lightweight design in a sustainability perspective. Materials Today Communications, 13 (December): 192–209, 10.1016/J.mtcomm.2017.09.012.

[10] Tujmer, M. (2021). Application of composite materials for a structural floor panel in a commercial vehicle. Master Thesis Fsb Zagreb, https://zir.nsk.hr/islandora/object/fsb:7195

[11] Horvat, M. (2017). Application of optical measurement system in analysis of formula student race car chassis, Fsb Zagreb.

[12] Goda, I., L'hostis, G., Guerlain, P. (2019). In-situ non-contact 3d optical deformation measurement of large capacity composite tank based on close-range photogrammetry. Optics And Lasers In Engineering, 119: 37–55, 10.1016/J.optlaseng.2019.02.006.

[13] HRN EN ISO 14125:2005 Fiber Reinforced Plastic Composites - Determination of Flexural Properties"

EUROPEAN MECHANICAL SCIENCE
e-ISSN: 2587-1110

RESEARCH ARTICLE

Evaluating the effectiveness of combined hardening models to determine the behavior of a plate with a hole under combined loadings

Melih Çaylak[1], Toros Arda Akşen[1], Mehmet Firat[1*]

[1]The University of Sakarya, Department of Mechanical Engineering, Sakarya, Turkey

Orcid: M. Çaylak (0000-0002-6857-6642), T.A. Akşen (0000-0002-7087-3216), M. Firat (0000-0002-3973-4736)

Abstract: Geometrical discontinuities in a material such as holes and notches on machine elements are called as critical regions due to the stress concentrations. They are the potential failure initiation locations, therefore, researchers put significant effort on the prediction of the material response in these discontinuities, especially under repetitive loadings. Cyclic plasticity is an important field of computational mechanics and deals with the nonlinear material response under cyclic loadings. In this study, numerical cyclic stress – strain response of a plate with a hole was evaluated under the combined loadings which are cyclic bending and tensile loadings. Oxygen Free High Thermal Conductivity (OFHC) Copper alloy was considered as material, and finite element simulations were performed in Marc software. A user defined material subroutine known as Hypela2 was utilized in order to define the material response. The plasticity model used in the present study comprises J2 plasticity along with combined isotropic – kinematic hardening model. Evolution of the backstress was introduced by Armstrong – Frederic type kinematic hardening model. The results were compared with the literature study, and it was seen that presented hardening model provides accurate results in small cyclic strain range.

Keywords: Cyclic Plasticity, Armstrong-Frederic Model, Kinematic Hardening, Small Strain, Finite Element Method

1. Introduction

Cyclic plasticity is an important research field investigating the stress – strain behavior of the materials under repetitive loadings. Under cyclic loading, materials exhibit unique features such as Bauschinger effect and ratcheting response. In order to model both behaviors, kinematic hardening models are incorporated into the constitutive framework. Prager [1] introduced the first kinematic hardening model. This linear kinematic hardening model could predict the Bauschinger effect; however, it fails to model the ratcheting. Later, Besseling [2] and Mroz [3] proposed multi-surface kinematic models based on the modifications of the Prager's model. However, both models could not tackle the ratcheting behavior. There were also several models based on multi-surface concept have been proposed in the literature [4, 5]. Then, Armstrong – Frederic put forward a nonlinear kinematic hardening model to sort out the ratcheting issue taking a fading memory – recovery term into consideration [6]. Through the fading memory term, backstress could saturate at a constant value and this model could present the ratcheting behavior of the material.

Some works can be found in the literature evaluating the influence of the kinematic hardening models on the cyclic stress – strain response of the material. Firat [8] carried out the finite element (FE) simulations of a notched round bar to investigate the notch root strains under combined loadings. 20 different tests comprising of proportional and non-proportional loadings were considered for SAE1070 steel. A kinematic hardening model in conjunction with a yield surface in pseudo stress space was implemented. It was observed that the numerical results were consistent with the experimental outcomes. Firat [9] also carried out another study on the same notched round bar using von Mises yield criterion coupled with a kinematic hardening model with multi – component. Six proportional and non-proportional tests were simulated in this study, he reported that the numerical results were consistent with the experiments and the presented material model was suitable for the fatigue life estimation. Aksen et. al. [10] conducted similar study on the same circumferentially notched round bar and assessed the effect of the different backstress parameters on the cyclic response of the material subjected to combined proportional and – non-proportional loadings. Joo and Huh [11], evaluated the stress – strain behavior of TWIP980

* Corresponding author.
Email: firat@sakarya.edu.tr

European Mechanical Science (2022), 6(2): 97-104
https://doi.org/10.26701/ems.1051057
Received: December 13, 2021 — Accepted: February 8, 2022

and TRIP980 steel sheets numerically and experimentally, under monotonic tensile and reversal tensile – compressive loadings. They employed a rate dependent material model involving a combined isotropic and kinematic hardening model in numerical approach to characterize the Bauschinger effect along with the transient behavior of the material. It was recorded that the proposed material model can be adopted in sheet metal forming applications as well as springback prediction. Huh et. al. [12] investigated the cyclic behavior of DQ and DP590 steels under intermediate and different strain rates by using combined hardening model. In addition, both FE simulations and experiments were conducted for different complex loading paths. The dependency of Bauschinger effect on strain rate was also evaluated and it is concluded that the Bauschinger effect changes with strain rates. Ohno et al. [13] developed a new algorithm to minimize ratcheting and cyclic stress relaxation. To this end, a plate with a hole was considered and finite element analyses were conducted for different element types such as brick and shell element to prove the accuracy of the new algorithm. An annealed OFHC Copper was chosen as material in this study and a combined hardening model was adopted as a hardening rule. It was reported that the new algorithm is applicable to both two-dimensional and three-dimensional stress states. Zhang et. al. [14] conducted a study by using the same specimen to introduce a new hardening model for cyclic plasticity, which takes into account anisotropic nonlinear kinematic and nonlinear isotropic hardening. It was concluded that, with the new model, predictions are mostly suitable even for the different materials and different loading paths. Montáns and Zhang [15] also carried out another study on the same holed plate made of OFHC Copper. They proposed a new model for non-linear kinematic hardening at large strains. It was reported that the new approach is suitable for large strains for soft materials and has no restriction tackling the materials anisotropy or the form of the stored energy. Fu et. al. [16] investigated the ratcheting effect of thin steel wires under cyclic loading comprising of tension-torsion loading. Experiments were conducted for thin 316L steel wires under different loading conditions. Finite element (FE) simulations with different kinematic hardening rules were also conducted. It was pointed out for macro-based model's that the numerical results tend to under-estimate the ratcheting behavior. Shojaei et. al. [17] applied a combined hardening model to predict ratcheting behavior of CS1026 steel under cyclic loading. Experimental data and numerical solutions were compared in this study. It was reported that the hardening rule used in the work accomplished to describe the material behavior under different repetitive loading paths. Badvana et. al. [18] investigated the ratcheting response of SS304 stainless steel numerically and experimentally under cyclic loading. To predict plastic behavior of the material, a combined hardening model and von-Mises isotropic yield criterion were employed. It was reported that, proposed hardening model satisfactorily predicted the experimental results. Tasavori et. al. [19] conducted similar study on 9Cr-1Mo steel in order to evaluate the ratcheting behavior under cyclic loadings. Numerical results predicted from the presented combined hardening model were compared with and the experimental outcomes. It was reported that accumulate progressive plastic strain is observed and amount of accumulated plastic strain is related with geometry of specimens. Nath et. al. [20] investigated the ratcheting effect on cyclically stable materials under different loading conditions. The results predicted by employing the introduced combined hardening model and the experimental outcomes were compared in this work. As a result, it was reported that the hardening data obtained with the presented method showed a good agreement with the experimental data. Lee et. al. [21] investigated the directional dependency of the hardening response. Several FE analyses were carried out for different material orientations. A new combined hardening model accounting for the directional dependency of the Bauschinger effect was proposed and compared with the existing literature It was reported that new model provides superior performance. Qin et. al. [22] proposed a new combined hardening model to examine the behavior of aluminums and steels under complex strain paths. They compared the numerical results with the experimental data for EDDQ pure aluminum and DP780 steel. It was pointed out that the accuracy of the proposed model for representing the Bauschinger effect, transient hardening and permanent softening under different strain paths is sufficient for the related materials. There are also several works investigating the effect of the combined hardening for different applications of mechanical design [23-25] and investigating the cyclic behaviors of notched specimens [26].

In this work, finite element (FE) analyses of a centered hole plate were conducted using a material model comprising an isotropic yield criterion in conjunction with Armstrong – Frederic kinematic hardening model. Oxygen Free High Thermal Conductivity (OFHC) Copper was considered as a test material. The plate was subjected to the tensile loading and bending, simultaneously. The results were compared with the numerical outcomes of Ohno.

2. Constitutive Model

A plasticity model involves a yield criterion, a flow rule, and a hardening rule. Yield criterion represents a limit distinguishing the elastic and plastic domains from each other. Flow rule establishes a relationship between the stress increment and plastic strain increment. Lastly, hardening rule elucidates the change of yield surface in terms of motion and expansion. In the present study, von Mises yield criterion was employed as yield function, and this criterion can be expressed as follows.

$$f_{VM} = \sqrt{\frac{2}{3}(\underline{\underline{S}} - \underline{\underline{\alpha}}) : (\underline{\underline{S}} - \underline{\underline{\alpha}})} - \sigma_0 = 0 \quad (1)$$

where, S denotes the deviatoric component of the stress tensor and α is the backstress tensor. σ_0 is the yield stress which is a function of the equivalent plastic strain. Here, the deviatoric component of stress can be defined as Eq. (2).

$$\underline{\underline{S}} = \underline{\underline{\sigma}} - \underline{\underline{\lambda}}\sigma_m \quad (2)$$

Here, λ is the Kronecker delta and σ_m is the mean stress. σ refers to the Cauchy stress tensor. Strain can be disintegrated into elastic and plastic components in an additive way such that,

$$d\underline{\underline{\varepsilon}} = d\underline{\underline{\varepsilon}}_e + d\underline{\underline{\varepsilon}}_p \quad (3)$$

Cauchy stress tensor can be determined using Hooke's law as follows.

$$d\underline{\underline{\sigma}} = \underline{\underline{\underline{\underline{C}}}}_e : d\underline{\underline{\varepsilon}}_e \quad (4)$$

Here C_e is the elastic tensor. Associated flow rule used in this work and is given in Eq. (5).

$$d\underline{\underline{\varepsilon}}_p = d\lambda \frac{df}{d\underline{\underline{\sigma}}} \quad (5)$$

In the equation above, $d\lambda$ denotes the plastic proportionality factor. During the plastic deformation, the yield locus expands, and the Cauchy stresses should comply with the expansion of the yield locus which leads to,

$$df = \frac{df}{d\underline{\underline{\sigma}}} : d\underline{\underline{\sigma}} + \frac{df}{d\bar{\varepsilon}_p} : d\bar{\varepsilon}_p = 0 \quad (6)$$

Hardening rule is essentially employed in order to capture the Bauschinger effect, ratcheting response. Initial attempts are concentrated on the modeling of Bauschinger effect [1, 7]. Later, Armstrong and Frederic proposed another model (AF) in order to predict the ratcheting behavior [6]. AF Kinematic hardening model can be expressed by Eq. (7).

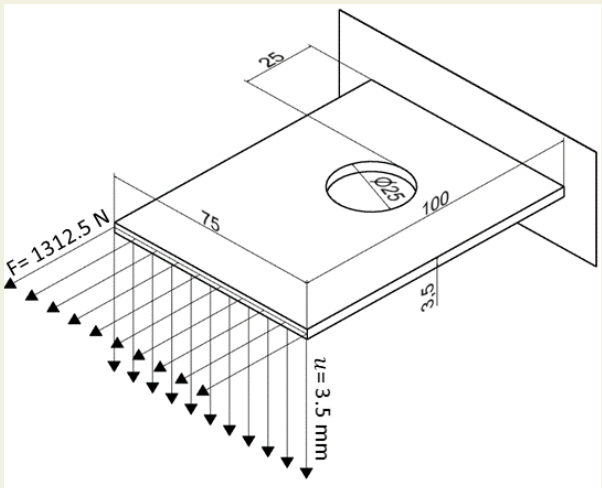

Figure 1. Model description [13]

$$d\underline{\underline{\alpha}} = \frac{2}{3} C d\underline{\underline{\varepsilon}}_p - \gamma\alpha\sqrt{\frac{2}{3} d\underline{\underline{\varepsilon}}_p : d\underline{\underline{\varepsilon}}_p} \quad (7)$$

The equation above comprises of two components. The first one represents the linear hardening; the second term represents the dynamic recovery [27]. Owing to the dynamic recovery term, AF model could represent the ratcheting behavior of the material. Hardening modulus decreases gradually and backstress eventually saturates at a constant value of C/γ. Here C and γ are correlated with the kinematic hardening part of the combined hardening model.

AF model was incorporated into the FE simulations through Hypela2 user defined material behavior subroutine.

3. Application

3.1. Description of the Model

In the present work, FE simulations of a plate with a hole were carried out. Dimensions of the model were procured from the Ref [13]. A tensile force of 1312.5 N was applied to the specimen which leads to 5 MPa nominal stress on one edge of the plate, while the other edge was fixed in all directions. Simultaneously, the same edge exposing to the constant nominal stress was subjected to the cyclic bending as well. The cyclic bending was applied as a displacement in out of plane direction. Fig. 1. shows the dimensions and loading conditions of the plate

Loading conditions were presented in Fig. 2 for tensile and bending loadings, separately.

3.2. Characterization of the Material

Within the scope of this work, OFHC copper was used as a test material. The mechanical data of the OFHC copper was taken from the Ref [13] and listed in the Table 1. Materials hardening curve was characterized by Swift law which is expressed as in the Eq. (8).

Table 1. Mechanical properties of OFHC Copper [13]

Parameter	Value
Swift Coefficient of Strength (K)[MPa]	144
Swift Hardening Exponent (n)	0.2
Reference strain (ε_0)	0.000011
Young Modulus [MPa]	123000
Poisson Ratio	0.34

$$\sigma_{true} = K.\left(\varepsilon_0^p + \varepsilon^p\right)^n \quad (8)$$

Combined hardening was adopted to represent the behavior of the material under cyclic loadings. Parameters of the combined hardening law were obtained using curve fitting method as well. Hardening was assumed as sum of the initial yield stress, backstress and isotropic hardening curve. The parameters of combined hardening law were

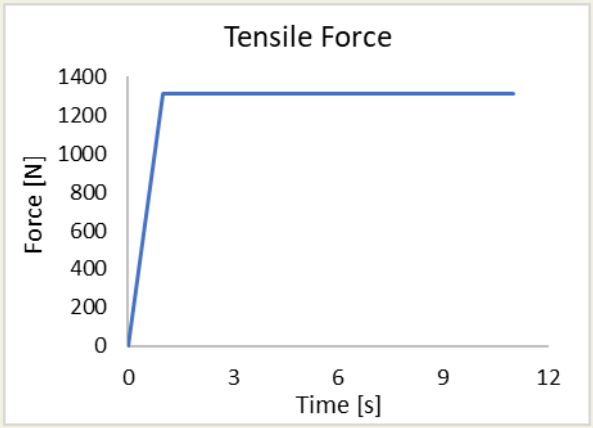

a)

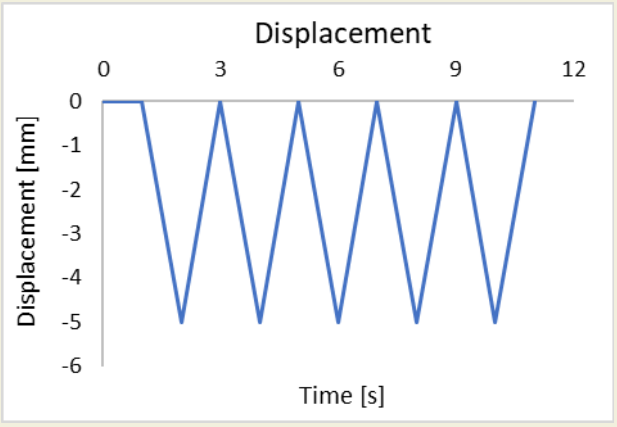

b)

Figure 2. Loading conditions for a) Tension b) Bending

summarized in Table 2. Isotropic hardening and backstress curves generated using these parameters were illustrated in Fig. 3. The expression of combined isotropic – kinematic hardening is as follows:

$$\sigma_{true} = \sigma_0 + \frac{Q}{b}\left(1 - e^{-b\varepsilon_p}\right) + \frac{C}{\gamma}\left(1 - e^{-\gamma\varepsilon_p}\right) \quad (9)$$

σ_0 denotes the initial yield stress whereas C and γ are the kinematic hardening parameters of AF model. Q and b are associated with the isotropic hardening behavior of the material.

Table 2. Combined hardening parameters of OFHC Copper

Parameters	σ_0 [MPa]	Q[MPa]	b	C [MPa]	γ
Value	14.67	2060	40	26000	1000

3.3. Ohno Model

In the present study, Ohno's model was utilized only for the comparison. Only a brief explanation was given here. Ohno disintegrated the backstress into several components. The backstress introduced by Ohno is as follows.

$$d\underline{\underline{\alpha}}^{(i)} = \frac{2}{3}h^{(i)}d\underline{\underline{\varepsilon}}^{p} - \zeta^{(i)}\left(\frac{\underline{\underline{\alpha}}^{(i)}}{r^{(i)}}\right)^{k^{(i)}}\alpha^{(i)}dp \quad (10)$$

where,

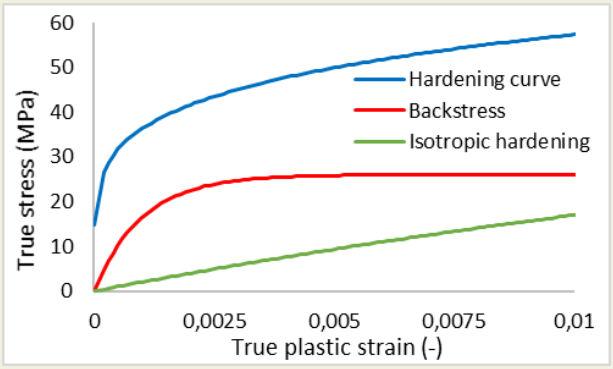

Figure 3. Hardening and backstress curves obtained with curve fitting method

$$\underline{\underline{\alpha}} = \sum_{i=1}^{m}\underline{\underline{\alpha}}^{(i)} \quad (11)$$

In the Eq. (10), dp represents the equivalent plastic strain increment. The parameters h and ζ are similar to the C and γ in the model employed in this work (See in Eq. (7)). h is a material function and expressed as in the Eq. (12).

$$h^{(i)}(p) = h_0^{(i)}\rho(p) \quad (12)$$

In Eq.12 ρ is a function of equivalent plastic strain and defined as,

$$\rho(p) = 1.0 + 2.11\,(1.0 - e^{-9.41p}) \quad (13)$$

Besides, $h_0^{(i)}$ is different for each component of backstress. Isotropic hardening of material is also defined by following expression.

$$Y(p) = Y_0\rho(p) \quad (14)$$

In the equation above, Y_0 is a constant material parameter. Detailed identification procedure was explained in the related article [13].

3.4. FE Modeling

FE simulations of plate with a hole were carried out in commercial Marc software associated with Hypela2 user defined material behavior subroutine. Mechanical properties and the combined hardening parameters were separately incorporated into the subroutine. Fully integrated hexahedral elements which are constant dilatational free from volume locking were utilized to discretize the plate [28, 29]. Owing to the orthotropic symmetry, half section of the plate was generated. Firstly, mesh sensitivity study was carried out by assuming only isotropic hardening. Element number in thickness direction and planar density of the elements were considered, separately. First, for the same planar mesh layout, elements in thickness direction

Table 3. Element numbers in thickness direction of each mesh structure

Case	Total element number	Number of layers in thickness	Solution time[s]
Case 1	1548	2	244
Case 2	3096	4	567
Case 3	6192	8	1369

were increased. Table 3 gives the total element numbers and the number of layers in out of plane direction. Mesh layouts were demonstrated in Fig. 4.

The results of the mesh sensitivity study conducted to investigate the influence of the elements through thickness were shown in Fig. 5 for monotonic loading and cyclic loading separately.

It was seen from the Fig. 5 that the case 2 and case 3 were almost identical. Nonetheless, a dramatic difference was observed between the case 2 and case 3 in terms of the solution time. Therefore, four elements in thickness direction were utilized in line with the case 2 for the further studies. Secondly, the effect of the planar mesh density was assessed. Three different mesh layouts with 4 elements in thickness direction were considered. Element numbers of each mesh layout were given in Table 4, while Fig. 6 gives the mesh layouts used in the planar mesh sensitivity study.

The results of planar mesh sensitivity work were depicted in Fig. 7.

According to the Fig. 7, case 2.2 and case 2.3 were satisfactorily close to each other. Having regard to the solution time, case 2.2 was selected for the further studies.

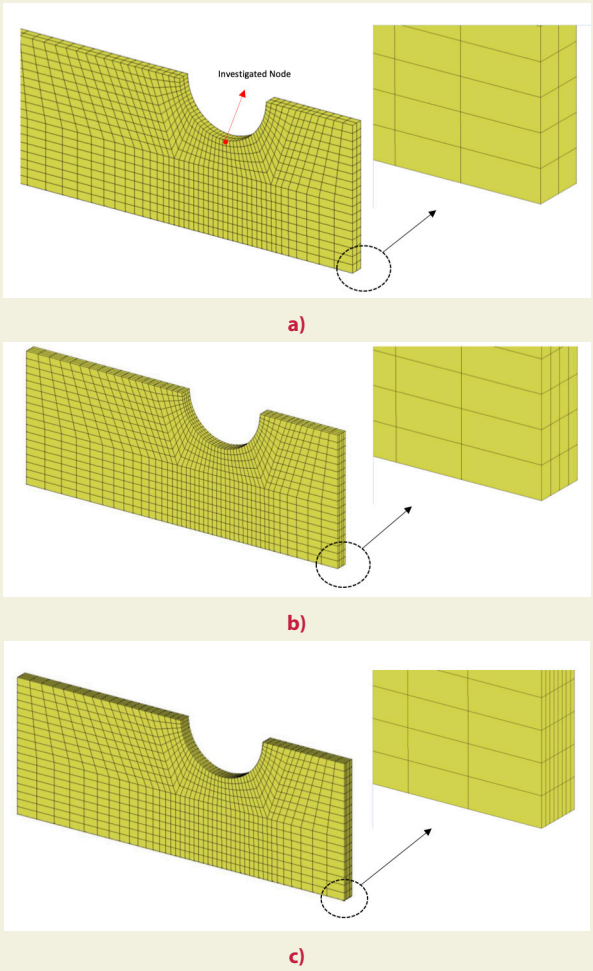

Figure 4. Through thickness elements of the different mesh structures, a) case 1 b) case 2 c) case 3

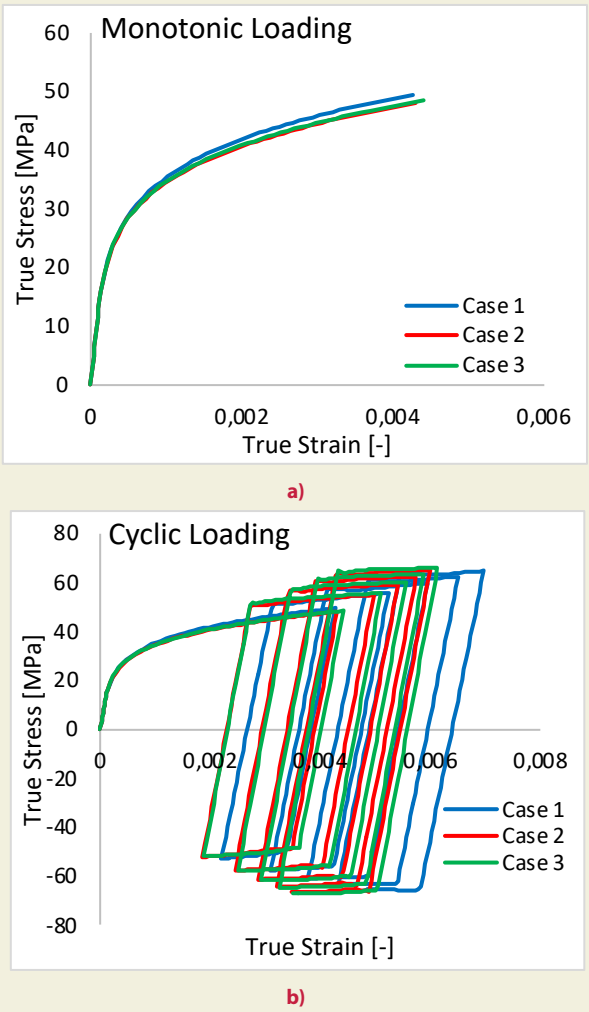

Figure 5. Stress – strain curves obtained from different mesh structures containing different element numbers in out of plane direction a) monotonic loading b) cyclic loading

Table 4. Element numbers of each mesh layout

Case	Total element number	Element number in thickness direction	Solution time[s]
Case 2.1	3096	4	567
Case 2.2	6080	4	1135
Case 2.3	9440	4	1811

4. Results and Discussion

In this section, cyclic deformation of plate with a hole was simulated based on the combined hardening rule assumption. Combined hardening parameters were employed into the Hypela2 user subroutine. The plate was exposed to tension and bending simultaneously. The tensile stress was constant during the process while bending was varying. The results obtained from FE simulation were compared with the Ohno's [13] numerical results. Comparison of the stress – strain curve prediction and the Ohno's result were given in Fig. 8.

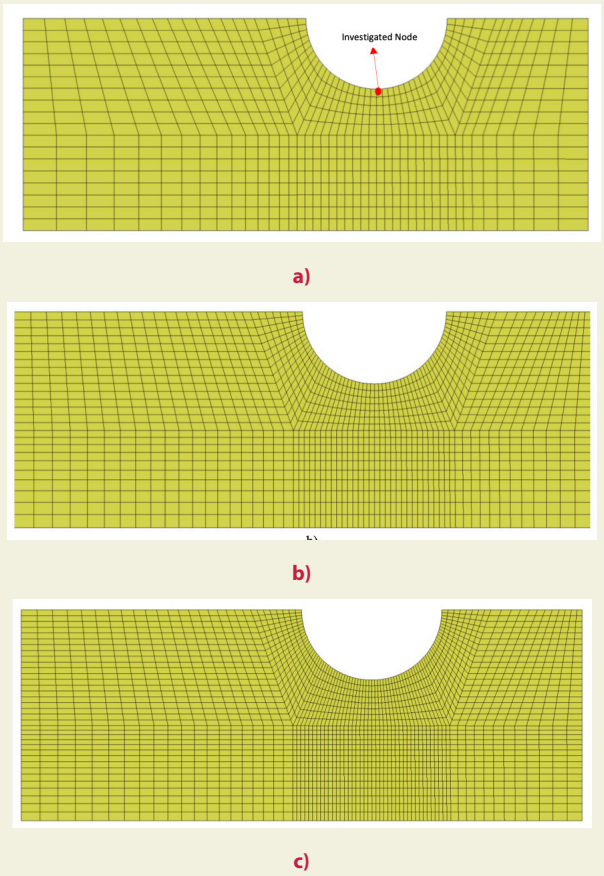

Figure 6. Planar mesh layouts of a) case 2.1 b) case 2.2 c) case 2.3

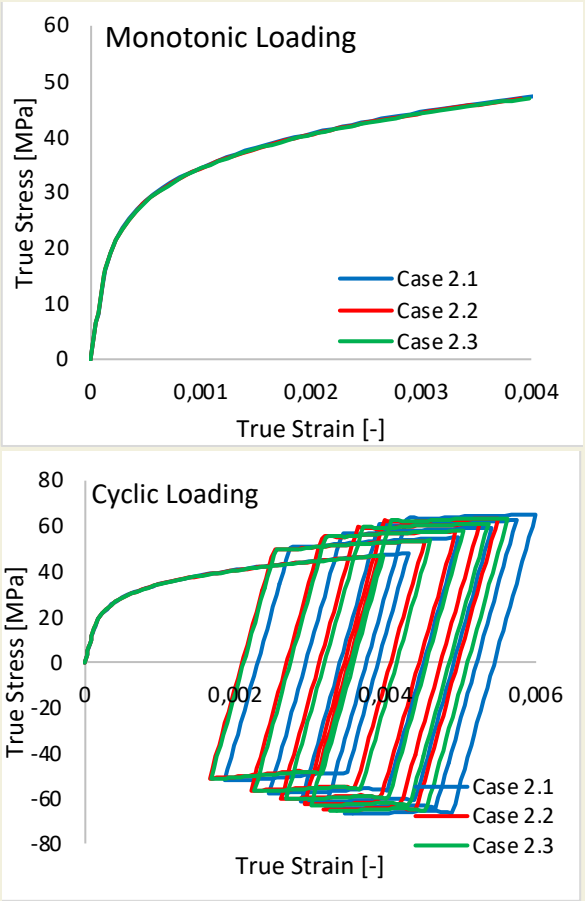

Figure 7. Stress – strain curves obtained from different planar mesh layouts a) monotonic loading b) cyclic loading

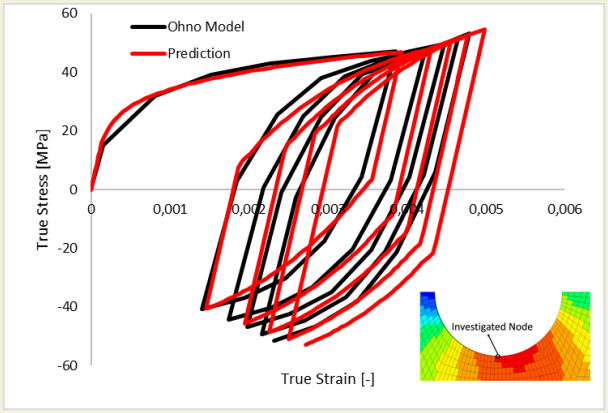

Figure 8. Comparison of the cyclic stress – strain curves obtained from numerical method and Ohno's model

Fig. 8 showed that the Ohno's results were accurately predicted. Especially, stress – strain behavior in the first cycle was entirely captured by the material used in this work. Combined hardening model with AF type kinematic model could address the Bauschinger effect. Moreover, ratcheting behavior of the OFHC copper was tackled by the presence of dynamic recovery – memory term of AF model. Minor discrepancies were observed after the first cycle when compared to the Ohno's result, but these differences were within the small range of error. Loops were inclined to converge in the higher cycles.

5. Conclusions

In the present work, a material model involving a combined isotropic – kinematic hardening model was implemented so as to define the cyclic response of a plate with a hole. The plate is exposed to a constant tensile stress as well as a cyclic bending. Simulations were carried out in commercial Marc software in conjunction with a user subroutine known as Hypela2. The numerical results obtained from the material model used in this work were compared with the Ohno's model [13]. The conclusions were summarized below.

- Bauschinger effect and the ratcheting behavior of the OFHC copper were successfully modeled by the combined hardening model.
- Numerical results obtained from the FE method were in accordance with the Ohno's numeric model. In particular, the first cycle of the cyclic stress – strain curve was accurately captured. The material model used in this work may lead to compatible predictions for the low cycle fatigue applications.
- The loops in cyclic stress strain curve were in tendency to converge which points out that the AF type kinematic hardening model provide a stabilization in loops.
- In the model proposed by Ohno [13], the backstress definition requires a complex calibration procedure and this complex calibration procedure brings about

larger solution times in FE analyses. However, the model employed in this study is more practical and user-friendly. Moreover, presented model provided compatible results in small cyclic strain range when the ratcheting effect is not large.

6. References

[1] Prager, W. (1956). A new method of analyzing stresses and strains in work hardening plastic solids. ASME Journal of Applied Mechanics, 23: 493-496. DOI:10.1115/1.4011389.

[2] Besseling, J.F. (1958). A theory of plastic and creep deformations of an initially isotropic material. ASME Journal of Applied Mechanics, 25: 529-536, DOI:10.1115/1.4011867.

[3] Mroz, Z. (1967). On the description of anisotropic work hardening. Journal of Mechanics and Physics of Solids, 15: 163-175, DOI:10.1016/0022-5096(67)90030-0.

[4] Dafalias, Y.F., Popov, E.F. (1976). Plastic internal variables formalism of cyclic plasticity. ASME Journal of Applied Mechanics, 98: 645-651. DOI:10.1115/1.3423948.

[5] Ohno, N., Wang, J.D., (1993). Kinematic hardening rules with critical state of dynamic recovery. Part 1: Formulations and basic features for ratcheting behavior. International Journal of Plasticity, 9: 375-390. DOI:10.1016/0749-6419(93)90042-O.

[6] Armstrong, P.J., Frederic, C.O. (1966). A mathematical representation of the multiaxial Bauschinger effect. G.E.G.B. Report RD/B/N 731.

[7] Ziegler, H.A. (1959). A modification of Prager's hardening rule. Quarterly of Applied Mechanics, 17: 55-65. DOI:10.1090/qam/104405.

[8] Firat, M. (2011). Notch strain calculation of a notched specimen under axial-torsion loadings. Materials and Design, 32: 3876–3882. DOI:10.1016/j.matdes.2011.03.005.

[9] Firat, M. (2012). Cyclic plasticity modeling and finite element analyzes of a circumferentially notched round bar under combined axial and torsion loadings. Materials and Design, 34: 842-852. DOI:10.1016/j.matdes.2011.07.022.

[10] Aksen, T.A., Esener, E., Firat, M. (2019). Investigation of Notch Root Strain Behaviors Under Combined Loadings, European Journal of Engineering and Natural Sciences, 3: 42-51.

[11] Joo, G., Huh, H. (2018). Rate-dependent isotropic-kinematic hardening model in tension -compression of TRIP and TWIP steel sheets. International Journal of Mechanical Sciences, 146–147: 432–444. DOI:10.1016/j.ijmecsci.2017.08.055.

[12] Joo, G., Huh, H., Choi, M.K. (2016). Tension/compression hardening behaviors of auto-body steel sheets at intermediate strain rates. International Journal of Mechanical Sciences, 108-109: 174–187. DOI:10.1016/j.ijmecsci.2016.01.035.

[13] Ohno, N., Tsuda, M., Kamei, T. (2013). Elastoplastic implicit integration algorithm applicable to both plane stress and three-dimensional stress states. Finite Elements in Analysis and Design, 66:1–11. DOI: 10.1016/j.finel.2012.11.001.

[14] Zhang, M., Benitez, J.M., Montáns, F.J. (2018). Cyclic plasticity using Prager's translation rule and both nonlinear kinematic and isotropic hardening: Theory, validation, and algorithmic implementation. Computer Methods in Applied Mechanics and Engineering, 328:565–593. DOI:10.1016/j.cma.2017.09.028.

[15] Zhang, M., Montáns, F.J., (2019). A simple formulation for large-strain cyclic hyperelasto-plasticity using elastic correctors. Theory and algorithmic implementation. International Journal of Plasticity, 113: 185–217. DOI:10.1016/j.ijplas.2018.09.013.

[16] Fu, S., Yu, D., Chen, G., Chen, X. (2016). Ratcheting of 316L stainless steel thin wire under tension-torsion loading. Fracture and Structural Integrity, 38: 141-147. DOI:10.3221/IGF-ESIS.38.19.

[17] Shojaei, A., Eslami, M.R., Mahbadi, H. (2010). Cyclic loading of beams based on the Chaboche model. International Journal of Mechanics and Materials in Design, 6:217–228. DOI:10.1007/s10999-010-9131-5.

[18] Badnava, H., Pezeshki, S.M., Nejad, F., Farhoudi, H.R. (2012). Determination of combined hardening material parameters under strain controlled cyclic loading by using the genetic algorithm method. Journal of Mechanical Science and Technology, 26(10):3067~3072. DOI:10.1007/s12206-012-0837-1.

[19] Tasavori, M., Zehsaz, M., Tahami, F.V. (2020). Ratcheting assessment in the tube sheets of heat exchangers using the nonlinear isotropic/kinematic hardening model. International Journal of Pressure Vessels and Piping, 183:104-103. DOI:10.1016/j.ijpvp.2020.104103.

[20] Nath, A., Ray, K.K., Barai, V. (2019). Evaluation of ratcheting behaviour in cyclically stable steels through use of a combined kinematic-isotropic hardening rule and a genetic algorithm optimization technique. International Journal of Mechanical Sciences, 152:138–150. DOI:10.1016/j.ijmecsci.2018.12.047.

[21] Lee, E., Stoughton, T.B., Yoon, J.W. (2019). Kinematic hardening model considering directional hardening response. International Journal of Plasticity, 110:145–165. DOI:10.1016/j.ijplas.2018.06.013.

[22] Qin, J., Holmedal, B., Hopperstad, O.S. (2018). A combined isotropic, kinematic, and distortional hardening model for aluminum and steels under complex strain-path changes. International Journal of Plasticity, 101: 156–169. DOI:10.1016/j.ijplas.2017.10.013.

[23] Shahabi, M., Nayebi, A. (2015). Springback modeling in L-Bending process using continuum damage mechanic's concept. Journal of Applied and Computational Mechanics, 1: 161-167. doi: 10.22055/jacm.2015.11020.

[24] Meggiolaro, M.A., Castro, J.T.P., Wu, H. (2015). On the applicability of multi-surface, two-surface and non-linear kinematic hardening models in multiaxial fatigue. Fracture and Structural Integrity, 33: 357-367. DOI: 10.3221/IGF-ESIS.33.39.

[25] Chen, J., Xiao, Y., Ding, W., Zhu, X. (2015). Describing the non-saturating cyclic hardening behavior with a newly developed kinematic hardening model and its application in springback prediction of DP sheet metals. Journal of Materials Processing Technology, 215: 151–158. DOI:10.1016/j.jmatprotec.2014.08.014.

[26] Adin, H., Sağlam, Z,. & Adin, M.Ş. (2021). Numerical Investigation of Fatigue Behavior of Non-patched and Patched Aluminum/Composite Plates. European Mechanical Sci-

ence, 5 (4): 168-176 . DOI: 10.26701/ems.923798.

[27] Paul, S.K., Sivaprasad, S., Dhar, S., Tarafder, M., Tarafder, S. (2010). Simulation of cyclic plastic deformation response in SA333 C-Mn steel by a kinematic hardening model. Computational Materials Science, 48: 662-671. DOI:10.1016/j.commatsci.2010.02.037.

[28] Marc 2018.1 Volume A: Theory and User Manual.

[29] Marc 2018.1 Volume B: Element Library.

EUROPEAN MECHANICAL SCIENCE
e-ISSN: 2587-1110

RESEARCH ARTICLE

Application of rotational accelerometers on the measurement of automotive headlamp cut-off deviation

Barış Ediz[1*], Erhan Ay[1] ,Emre Öztürk[1]

[1]Marelli Mako Turkey Elektrik Sanayi ve Ticaret A.Ş., Turkey

Orcid: B. Ediz (0000-0002-2704-7090), E. Ay (0000-0001-9621-6030), E. Öztürk (0000-0001-5492-9358)

Abstract : Automotive lighting products, such as Head Lamps (HL), Fog Lamps (FL), Daytime Running Lamps (DRL), face with mechanical vibrations during service life which may coincide with the resonance frequencies of the light source. When excited at resonance frequencies, especially in the case of HL's, light beam cut-offline may deteriorate and vibration of light beam occurs. This situation is also called light flickering. This state has disturbing effect on the driver's visibility, which is valid for both the driver and the counter drivers. Most of the automotive manufacturers have developed test specifications for evaluation of flickering state under sinusoidal frequency sweep acceleration loading and they have introduced limits for flickering angle range or displacement range of the light beam with respect to frequency measured on a screen which is put on a prescribed distance from the light source. In this study a traditional way of light beam flickering angle deviation measurement method of HL is presented. Furthermore, application of precise & efficient way of measurement method by the use of quartz rotational accelerometer is inspected.

Keywords: Head Lamp, Light Beam Vibrations, Light Flickering, Quartz Rotational Accelerometer, Sinusoidal Sweep Test, Resonance Search Test, Harmonic Sweep

1. Introduction

Due to vibrations coming from the road conditions at low frequencies between 10Hz to 50Hz, automotive headlamps must be designed to avoid resonance frequencies below 50Hz or response of the HL to low frequency vibration excitations must be significantly low. Light source excited by vibration loads at its resonance frequencies starts to vibrate and this will cause light beam vibrations which is also called light flickering. Light flickering has disturbing effect to the light pattern in front of the car and to the visibility of the both driver & counter drivers. In order to prevent the disturbing situation, car & HL manufacturers have developed test specifications and test methods for measuring HL light beam vibration range.

In this paper the traditional reflected laser beam displacement measurement method and application of quartz rotational accelerometer on direct measurement of the rotational accelerations has been discussed. Reflected laser beam method requires lots of effort from preparation of test set-up to conduction of measurements. Furthermore, this method has low accuracy level due to manual work of the technician and requires further calculations based on assumptions. In contrast, application of new measurement device, quartz rotational accelerometer, has been introduced for HL beam vibration direct measurements. Furthermore, rotation angle range is calculated from conversion of rotation angle acceleration frequency response to rotation angle frequency response by multiplying the double amplitude of the rotational acceleration by the square of the frequency. Rotational accelerometer reduces the effort required to perform tests and increases the accuracy level of the measurements.

In the literature one can find several studies related to different application areas of rotational accelerometers as a measurement equipment for different aims.

Methods for measuring rotational motion and linear motion of a vehicle has been proposed by using five different configurations of linear accelerometers [1]. Increase in measurement errors by the use of linear accelerometers to measure rotational motion has been mentioned. Direct angular acceleration measurement device which is mostly used to calculate the rotational inertia of the crash test dummies, quartz rotational accelerometer, has been introduced. This type of accelerometer also has been used to measure vibration shaker head rotations, which

* Corresponding author.
Email: baris.ediz@marelli.com

European Mechanical Science (2022), 6(2): 105-109
https://doi.org/10.26701/ems.989166
Received: August 31, 2021 — Accepted: February 16, 2022

has significant effect on the accuracy of the modal tests. [2]. Performance capabilities of commercially available direct rotational accelerometers for identification of rotational DoFs in the field of structural dynamics has been inspected. Advantages & disadvantages of using quartz rotational accelerometer as direct measuring device have been presented. [3]. A method for measuring high quality torsional receptance by the use of quartz rotational accelerometer has been presented. This method has been used to measure torsional receptance's at the ends of a shafting system and good estimations have been made [4]. In order to diminish the effects of rotational shocks and vibrations from a small disk drive, an algorithm which uses signal from a rotational accelerometer has been introduced [5]. A MEMS-based rotational accelerometer has been successfully applied to the rejection of rotational disturbances on a commercial computer hard disk drive (HDD) [6]. HL beam displacements has been measured under sinusoidal harmonic excitation on a vibration shaker by laser method and results are compared with harmonic FEA results. [7]

2. Material & Methods

2.1. Sinusoidal Sweep Excitation

The force contains one single frequency at a time and the excitation sweeps from one frequency to another with a given step, allowing the structure to engage in one harmonic vibration at a time. [8]

In this study, constant 1g sinusoidal base excitation acceleration load is applied by the vibration shaker over the frequency range. Unit constant acceleration is used as excitation and frequency response of the system is measured. Frequency sweep rate kept constant as 1 octave/minutes between 10 Hz to 100Hz.

Test set-up for sinusoidal sweep excitation is given in Figure 1.

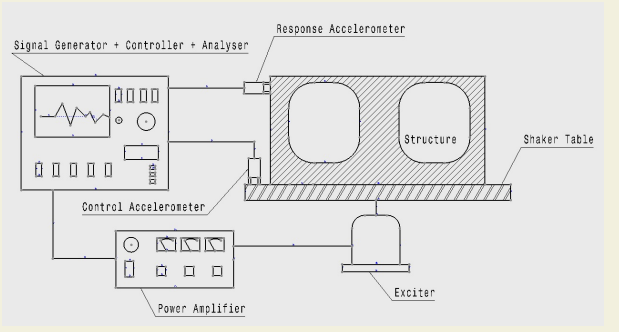

Figure 1. Basic Hardware for Sinusoidal Sweep Excitation

Harmonic response of displacement $x(t)$ for a single-degree-of-system excited by an harmonic Force, $F(t) = kA\cos\omega t$, is given by the equation below [9];

$$x(t) = A|G(i\omega)|e^{i(\omega t-\emptyset)} \quad (1)$$

where $G(i\omega)$ is a measure of the system response to a harmonic excitation of frequency ω.

When equation (1) is differentiated with respect to time;

$$\dot{x}(t) = i\omega A|G(i\omega)|e^{i(\omega t-\emptyset)} = i\omega x(t) \quad (2)$$

$$\ddot{x}(t) = (i\omega)^2 A|G(i\omega)|e^{i(\omega t-\emptyset)} = -\omega^2 x(t) \quad (3)$$

After inspecting the equations (2) and (3), it is concluded that the magnitude of the velocity is equal to the magnitude of the displacement multiplied by the factor ω and magnitude of the acceleration is equal to the magnitude of the displacement multiplied by the factor ω^2.

2.2. Laser Beam Reflection Method

In order to measure light beam vibrations, a traditional method is used. Similar test methods to this one has been performed by HL manufacturers as component level verification methods. Acceptance criteria, upper & lower response limits and some test parameters like screen distance D (mm), excitation g level, test frequency range etc.; are propriety information depending of HL & Car manufacturers. This method is based on measuring the light beam deflection on a screen with respect to frequency of the constant sinusoidal base excitation acceleration load applied on HL placed on a fixture on the vibration shaker (Figure 2 & Figure 3). A laser beam is projected to the mirror placed in front of the light source of HL and the laser beam is reflected to a screen placed on a prescribed distance D from the light source (Figure 2 and Figure 3). Technician marks the upper & lower ends of the reflected beam pattern on the millimetric paper for each excitation frequency intervals. Afterwards, vertical displacement range $d(\omega)$ of the light beam at the corresponding excitation frequencies are measured. (Figure 3.b). As a result, rotation angle frequency response $R(\omega)$ range in degrees, can be calculated by the given formula below;

$$R(\omega) \cong 0{,}5\tan^{-1}\frac{d(\omega)}{D} \quad (4)$$

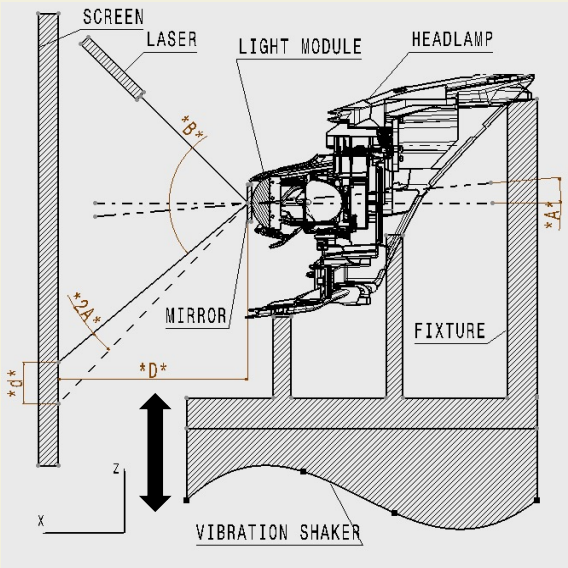

Figure 2. Test Set-Up

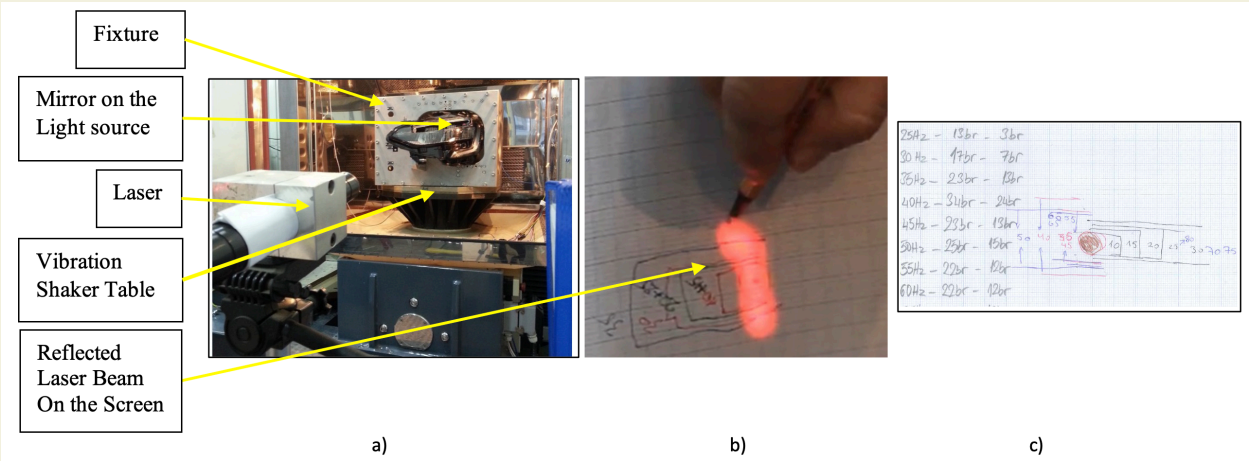

Figure 3. a) Laser beam pointed to mirror on the light source, b) Example of marking of light beam displacement range reflected on a millimetric paper placed on a screen prescribed distance D to light source c) Displacement Ranges after completion of test

where $d(\omega)$ is the vertical displacement range of the projected laser beam on the screen in mm and D is the horizontal distance between the HL light source and the screen in mm.

Graphical representation of light beam calculated rotation angle range in lateral y-axis with respect to frequency is made and compared with the limits (Figure 4).

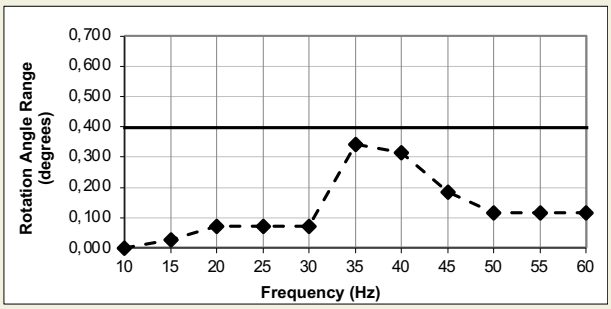

Figure 4. Example of measurement result (– – –) with respect to limits (——) for rotation angle range of light beam

2.3. Application of Rotational Accelerometer

In order to measure oscillations occuring about the lateral y- axis of the light source with respect to frequency, KISTLER® shear-quartz type 8840 rotational accelerometer has been used.(Figure 5)

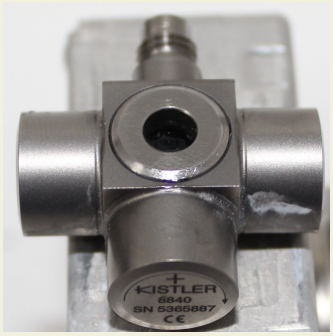

Figure 5. KISTLER® shear-quartz type 8840 rotational accelerometer

Rotational accelerometer is placed on the rear side of the light module in such a way that it can measure lateral oscillations. (Figure 6)

Figure 6. Rotational accelerometer placed on the rear side of light module

The element structure of Type 8840 accelerometer is such that the unit will accurately measure the acceleration magnitude of oscillations laterally induced to its mounting base. Technical characteristics of the accelerometer is given in Table 1.

Output of the accelerometer is connected to vibration shakers data acquisition unit and sinusoidal sweep excitation under 1g constant acceleration has been performed between 10Hz – 100 Hz with frequency sweep rate of 1 octave/minute. Rotation angle acceleration frequency response of the accelerometer has been tabulated and plotted by the help of shakers digital signal processing (DSP) and synthesis software. Furthermore, amplitude of rotation angle acceleration has been converted to rotation angle amplitude by the analogy of equation (3). However this time, acceleration frequency response is the rotation angle acceleration frequency response in degrees/s^2, displacement frequency response is rotation angle frequency response in degrees

Table 1. Technical data for Type 8840 rotational accelerometer

Specification	Unit	Type 8840
Acceleration range	krad/s2	±150
Acceleration limit	krad/s2	±200
Threshold (noise 130 μVrms)	rad/s2	4
Sensitivity nom.	μV/rad/s2	35
Resonant frequency mounted, nom.	kHz	23
Frequency response, ±10%	Hz	1 … 2000
Amplitude non-linearity	%FSO	1
Time constant	s	1
Transverse sensitivity typ (max.)	%	1.5 (2)
Vibration (max.)	g	2000
Shock limit (1 ms pulse width) max.	g	5000
Base strain sensitivity @250με	g με	0.005
Long term stability	%	±1
Temperature coefficient of sensitivity	%/°F	-0.03
Temperature range operating	°F	-65 … 250
Temperature range storage	°F	-100 … 300

$$|Rotation\ angle\ (\omega)| = \frac{|Rotation\ Angle\ Acceleration(\omega)|}{\omega^2} \quad (5)$$

3. Results & Discussion

Measurement results of laser beam reflection method and measurement results of rotational accelerometer are plotted back to back on Figure 7. Rotational accelerometer predicts the resonance frequency at 48.42Hz with double amplitue of 0.47°. However, laser beam reflection method predicts the resonance frequency at 45Hz with the double amplitude of 0.46°. Which means, 7.1% error in frequency and 2.1% error in double amplitude.

When Figure 7 is inspected in detail; it is obvious that due to low resolution of laser beam measurement method, in which the data is taken at 5Hz intervals, behaviour of the system can not be characterised in detail and some peaks and features are missed. Due to higher frequency resolution of rotational accelerometer measurements, rotation angle frequency response of the system can be characterised in more detail.

Sinusoidal sweeps have been performed by constant 1g vertical excitation with 1 octave/minute sweep rate on the shaker with & without rotational accelerometer mounted on the light module in order to understand the effect of 18.5gr weight of the rotational accelerometer on the resonance frequency of the light module. Another acceler-

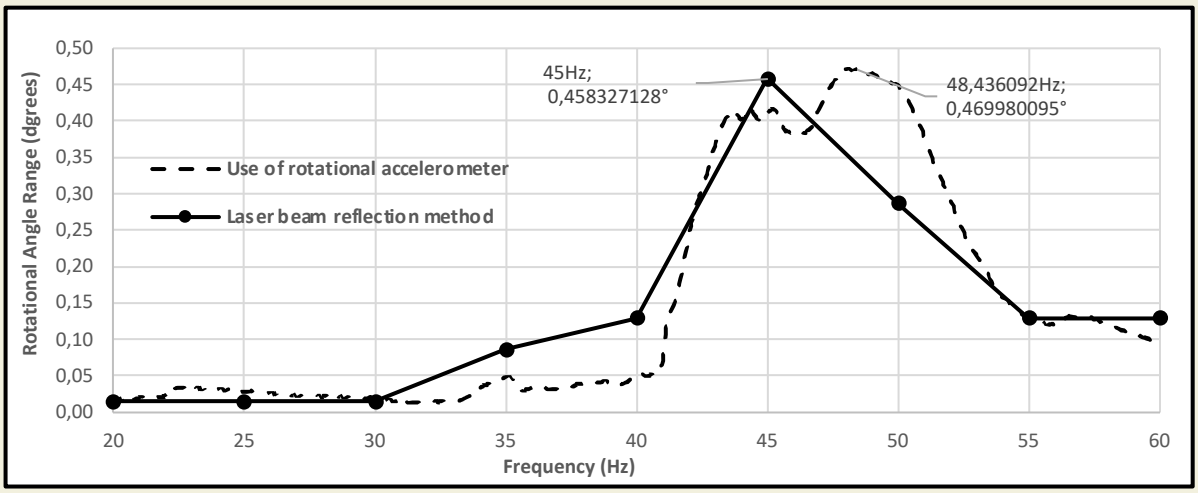

Figure 7. Comparison of resonance search results, laser beam reflection method vs the use of rotational accelerometer

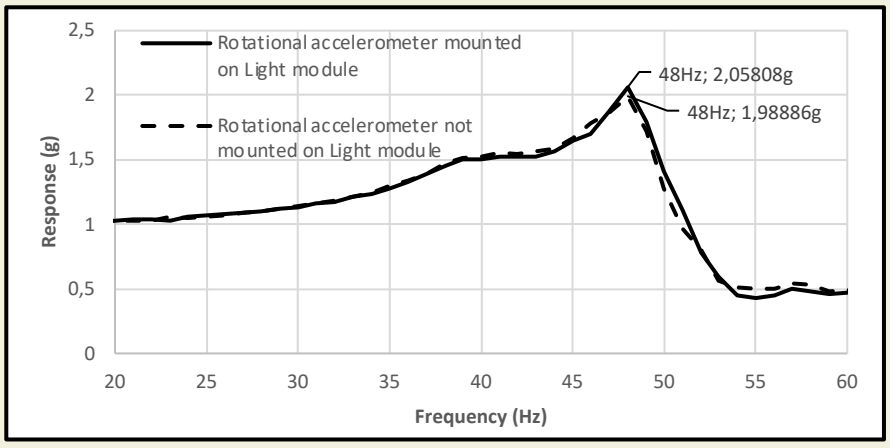

Figure 8. Effect of Rotational Accelerometer Weight on Resonance Frequency

ometer has been mounted on the housing of the HL and vertical acceleration frequency response of the HL has been measured. Frequency response curves with 1Hz resolution has been plotted on Figure 8 below.

When Figure 8 is inspected in detail; it is obvious that 18.5gr weight of the rotational accelerometer does not effect the resonance frequency of the light module significantly when 1Hz resolution is taken into account.

4. Conclusion

In this study, traditional laser beam reflection method & a new method which uses a quartz rotational accelerometer for measuring HL light beam vibrations are inspected and compared. According to this study below conclusions can be made:

- Laser beam reflection method needs many efforts from preparation of test set-up to preparation of test sample. However, application of rotational accelerometer reduces the effort and time for test set-up preparation and for preparation of test sample.
- Laser beam reflection method has low accuracy level due to manual work of the technician, open to errors. However, application of rotational accelerometer prevents manual work and prevents errors.
- Results of laser beam reflection method cannot characterize the system rotation angle frequency response in detail due to data taken at 5Hz intervals which gives low resolution frequency response curve. However, by the application of rotational accelerometer, usage of signal acquisition hardware and DSP software, high resolution rotation angle frequency response curves can be plotted. In this way, system rotation angle frequency response can be characterized in detail.

There are other techniques used in determination of modal parameters and structural charateristics. One of them is called laser Doppler Vibrometry. This technique uses laser beams & the principle of interferometry. Dynamic structural characteristics and modal parameters are measured without mounting any sensor on the test sample. Hence, in this way, test sample is not affected by the weight of the sensor. However, this innovative technique requires more expensive equipment than the method proposed in this paper. Future work on this subject can be the investigation of Automotive HL light beam vibrations by Laser Doppler Vibrometry.

5. References

[1] Schuler, A.R., Grammatikos, A., Fegley, K. A., (1967). Measuring Rotational Motion with Linear Accelerometers. IEEE Transactions on Aerospace and Electronic Systems, 3: 465-472. doi: 10.1109/TAES.1967.5408811.

[2] Dumont, M., Kinsley, N., (2015). Rotational Accelerometers and Their Usage in Investigating Shaker Head Rotations. Sensors and Instrumentation. Conference Proceedings of the Society for Experimental Mechanics Series, 85-92. doi:10.1007/978-3-319-15212-7_10.

[3] Drozg, A., Rogelj, J., Čepon, G.,Boltežar, M., (2018). On the performance of direct piezoelectric rotational accelerometers in experimental structural dynamics. Measurement,127: 292-298. doi:10.1016/j.measurement.2018.05.081.

[4] Tsai, S. H., Ouyang, H., Chang, J. Y., (2019). Identification of torsional receptances. Mechanical Systems and Signal Processing, 126:116-136. doi:10.1016/j.ymssp. 2019.01.050.

[5] Abramovitch, D. Y., (1997). Rejecting rotational disturbances on small disk drives using rotational accelerometers. Control Engineering Practice, 5(11): 1517-1524. doi:10.1016/S0967-0661(97)10005-3.

[6] Oboe, R., Vigna, B., Gola, A., (2000). Application of MEMS-based rotational accelerometers to vibration suppression in hard disk drives. 2000 Asia-Pacific Magnetic Recording Conference, Digests of APMRC2000 on Mechanical and Manufacturing Aspects of HDD,MP17/1-MP17/2. doi: 10.1109/APMRC.2000.898952.

[7] Roucoules, C., Chemin, F., Cros, C., (2010). FRF prediction and durability of optical module and headlamp. Proceedings of ISMA2010 including USD2010,1: 4373-4383.

[8] He, J. , Fu, Z.F, (2001). Modal Analysis. Butterworth – Heinemann, Linacre House, Jordan Hill, Oxford OX2 8DP 225 Wildwood Avenue, Woburn, MA 01801-2041.

[9] Meirovitch, L., (2001). Fundamentals of Vibrations. McGraw-Hill, Boston.

EUROPEAN MECHANICAL SCIENCE
e-ISSN: 2587-1110

RESEARCH ARTICLE

A numerical approach in the investigation of the effects of diethyl ether and ethanol mixtures on combustion characteristics and NO emissions in a DI diesel engine

Ilker Temizer[1], Fırat Gucer[2], Omer Cihan[3*]

[1]Sivas Cumhuriyet University Technology Faculty, Department of Manufacturing Engineering, 58140, Sivas, Turkey
[2]Sivas Cumhuriyet University, Institute of Science and Technology, 58140, Sivas, Turkey
[3]Hakkari University, Engineering Faculty, Department of Mechanical Engineering, 30000, Hakkari, Turkey

Orcid: İ. Temizer (0000-0003-1170-3898), F. Gucer (0000-0003-0194-9376), Ö. Cihan (0000-0001-8103-3063)

Abstract: In this study, the effects of adding ethanol and diethyl ether to diesel fuel on combustion characteristics and NO emissions were numerically investigated. Neat diesel fuel and by volume 90% diesel+10% ethanol blend, 80% diesel+20% ethanol blend, 80% diesel+10% ethanol+10% diethyl ether blend and 85% diesel+ 10% ethanol+5% diethyl ether mixtures were used as fuel. Analyzes were carried out using a single-cylinder, air-cooled, four stroke direct injection diesel engine at 2000 and 3000 rpm engine speed conditions. AVL FIRE software was used for numerical study. In-cylinder pressure, cumulative heat release rate, turbulent kinetic energy, NO emissions and velocity distributions in the combustion chamber were investigated for specified fuel. As a result, the in-cylinder pressure and heat release rate of ethanol and diethyl ether blended fuels were lower than diesel fuel at both speeds. It was observed that NO emissions decreased as the ethanol content in the fuel increased. At 3000 rpm, the highest TKE value was obtained in D90E10 mixed fuel, and the lowest value was found in D80E10DEE10 mixture fuel. Ethanol positively affected the turbulent kinetic energy at both engine speeds.

Keywords: Diesel fuel blends; ethanol; diethyl ether; NO emission.

1. Introduction

Today, with the increase in oil prices, the decrease in the demand for fossil fuels and the increase in air pollution, studies on the use of alternative fuels in diesel engines have increased as well as in gasoline engines [1,2]. When the studies in the literature are examined, there are many studies in which ethanol and diethyl ether are used as fuel at different rates.

Carvalho et al. investigated the effects of the use of diethyl ether (DEE) on engine performance and emissions in a diesel engine operating on biodiesel-ethanol mixtures. In this study, besides biodiesel and diesel fuel, B80E20 (80% biodiesel, 20% ethanol) and B76E19DEE5 (76% biodiesel, 19% ethanol and 5% diethyl ether) fuels were tested at different engine loads (2.7 kW, 5.4 kW, 8.1 kW). The highest fuel consumption and the highest NO emissions were observed when B80E20 fuel was used for all loads in the engine studied, while the best engine efficiency was determined with B76E19DEE5 fuel. This is due to higher oxygen content and lower cetane number. In all three load conditions, B100 fuel according to D100, CO and NOx increased while THC decreased. [3]. Wang et al. investigated the effects of using biodiesel-ethanol mixtures and diethyl ether (DEE) on engine performance and emissions in a diesel engine. In this study, besides diesel and biodiesel fuels, B95E5 (95% biodiesel, 5% ethanol), B90E10, B95DEE5 (95% biodiesel, 5% diethyl ether) and B90DEE10 fuels were used. Biodiesel fuel was produced from orange oil methyl ester. As a result, the thermal efficiency of the engine increased when the biodiesel-ethanol mixture was used compared to diesel fuel and biodiesel fuels. When using B90DEE10 fuel, CO emissions increased while HC, smoke and NO_x emissions decreased, better engine performance and lower emission values were obtained with this B90DEE10 fuel compared to other biodiesel mixture types [4]. Sivalakshmi and Balusamy investigated the combustion, performance and emission values of BD5 (5% diethyl ether and 95% neem oil biodiesel), BD10 and BD15 fuels using 5%, 10% and 15% diethyl ether as an additive in a diesel engine. When the BD5 mixture was compared with other fuels,

* Corresponding author.
Email: omercihan@hakkari.edu.tr

European Mechanical Science (2022), 6(2): 110-118
https://doi.org/10.26701/ems.1062227
Received: January 24, 2022 — Accepted: June 6, 2022

the highest in-cylinder pressure value and heat release rate was reached in the engine than the neat biodiesel fuel. Also, BD5 fuel compared to other neat biodiesel fuel, it reduced CO emissions at full load, while soot emissions decreased under all load conditions. NO and HC emissions increased at almost all loads. Higher thermal efficiency was obtained in BD5 fuel [5]. Ibrahim used diesel fuel, a mixture of cottonseed biodiesel and diethyl ether (D100, D70B30, D70B25DEE5 and D70B20DEE10) in a diesel engine operating at 1500 rpm. In the engine in which D70B30 mixture was used, it was observed that the specific fuel consumption increased while the thermal efficiency decreased compared to diesel fuel. When the results were examined, there was an increase in the specific fuel consumption and a decrease in the thermal efficiency with the increase in the DEE ratio in the mixture compared to diesel fuel, 8.1% and 6.8%, respectively. DEE did not affect the stable operation of the engine in any negative way. However, diesel fuel compared to other fuels had lower heat release rate and longer burning duration at higher engine loads [6]. Pugazhvadivu and Rajagopan compared their effects on emissions by adding 10%, 15% and 20% diethyl ether to B25, B50, B75, B100 and diesel fuel. Addition of diethyl ether to these mixtures resulted in significant reductions in NOx emissions at low and medium loads. However, NO_x emission was higher compared to diesel, and it lower compared to biodiesel blend at high loads [7]. Verma et al. looked at the effect of ethanol (E)-methanol (M)-diesel-microalgae biodiesel (S) blend on engine performance and emissions. In this study, seven different fuels were tested, namely S0E0M0, S20E0M0, S40E0M0, S20E20M0, S40E20M0, S20E0M20 and S40E0M20. The engine was operated under different load conditions (25, 50, 75 and 100%). As a result, it had been observed that mixtures containing ethanol increased the torque and decrease the exhaust gas temperature. On the other hand, the methanol helped to increase the cylinder pressure. In addition, the ignition delay duration and burning duration were increased with the methanol [8].

Venu and Madhavan investigated the effects on the engine by adding diethyl ether to ethanol-jatropha plant biodiesel-diesel (EBD) and methanol-biodiesel-diesel (MBD) fuels. EBD (20% ethanol, 40% biodiesel and 40% diesel) and MBD (20% methanol, 40% biodiesel and 40% diesel) mixtures were added with 5% and 10% diethyl ether. These fuels were named as EBD-5DEE, EBD-10DEE, MBD-5DEE and MBD-10DEE. As a result, adding DEE to EBD increased the in-cylinder pressure value while reducing the burning duration and NO_x emissions. On the other hand, with the addition of DEE to MBD, the brake specific fuel consumption, cylinder pressure and heat release rate were decreased and in the exhaust emissions, soot, CO and CO_2 emissions increased. In general, blends of EBD-5DEE and MBD-5DEE gave better results than blends of EBD-DEE10 and MBD-DEE10. The lowest NO_x emission and the bsfc were reached for MBD-5DEE fuel [9]. Sugash et al. studied the effects of a blend of cottonseed biodiesel with diethyl ether on performance and emissions. In the study, diesel fuel, B20 (20% biodiesel, 75% diesel fuel, 5% diethyl ether), B40 (40% biodiesel, 55% diesel fuel, 5% diethyl ether) and B60 (60% biodiesel, 35% diesel fuel, 5%) diethyl ether) fuels were tested at different engine loads (25%, 50%, 75%, 100%). When the results were examined, it was determined that the thermal efficiency of B20 fuel was close to the diesel fuel. In the results obtained with B60 fuel, the lowest fuel consumption and NO emission values were obtained, and the maximum CO and UHC emissions was reached. Addition of diethyl ether the specific fuel consumption of fuel was reduced [10].

Nishanth et al. researched the effects of Jatropha Curcas biodiesel-diethyl ether mixture on a variable compression ratio diesel engine. Diesel, B1 (20% biodiesel, 75% diesel fuel, 5% diethyl ether), B2 (25% biodiesel, 70% diesel fuel, 5% diethyl ether) and B3 (30% biodiesel, 65% diesel fuel, 5% diethyl) ether) fuels were used. In the study, it was emphasized that B2 fuel increased thermal efficiency and mechanical efficiency, 6.32% and 3.15%, respectively. Also, HC and NO_x emissions reduced with this fuel type [11]. Ayhan and Tunca used as fuel diesel fuel and mixtures containing 3%, 5% and 7% DEE in a single-cylinder direct injection diesel engine. A decrease in torque and effective power was observed as the DEE ratio increased at full load and 1000, 1300, 1600 and 2000 rpm speed conditions. The specific fuel consumption and effective efficiency were improved in the engine. Moreover, it was determined that there were significant reductions in NO_x and soot emissions [12]. Loganathan et al. used hydrogen-enriched cashew nut shell biodiesel by adding diethyl ether in a single-cylinder diesel engine. As a result, when hydrogen was added to the mixture, CO and HC emissions decreased, and it was determined that they were further reduced by adding diethyl ether to these mixtures, 43% and 50% decrease respectively. Also, in-cylinder pressure, NO_x emission and heat release rate were increased with the addition of DEE [13]. The high cetane number, oxygen content, low calorific value, the high latent heat of vaporization parameters of DEE affect NO_x formation. High cetane number reduces ignition delay and also reduces NOx emissions by shortening combustion duration [14]. The high burning velocity of DEE makes an extra contribution to the shortening of the burning time. Improves engine performance and exhaust emissions thanks to shorter combustion durations [15]. The addition of ethanol and DEE to diesel fuel decreased the in-cylinder chamber temperature with both increased heat of vaporization and low flame temperature. As a result, the combustion temperature has decreased and therefore NO_x emissions have decreased [16]. Banapurmath et al. [17] tested different volume ratios of ethanol and DEE

in a single-cylinder direct injection diesel engine. Effect of ethanol and diethyl ether-diesel blends on diesel engine performance, combustion and emissions was investigated using four different blends of ethanol (E0 -neat diesel, E5, E10, E15 and E20)and diethyl ether (DEE0 - neat diesel, DEE5,DEE10, DEE15 and DEE20). As a result, as the ratio of ethanol and DEE increased, NO_x decreased at low loads, while HC increased because of high fuel consumption and high latent heat of vaporization. On the other hand, CO emissions decreased at high loads, and brake thermal efficiency increased.

Usta et al. tested an ethanol-diesel mixture containing 15% ethanol and two different biodiesel blended fuels in a four-cylinder turbo diesel engine with a pre-combustion chamber. While ethanol in the mixture decreased CO emissions, it increased NO_x emissions. While ethanol caused a decrease in engine power, the addition of biodiesel did not affect power compared to diesel fuel [18].

Today, many software are used that allow flow, heat and emission modeling in internal combustion engines [19-23]. These software provide significant advantages in terms of both time and cost reduction. Xu et al. experimentally and numerically investigated the effects of diesel fuel and acetone-butanol-ethanol (ABE) mixtures on combustion and soot formation in a diesel engine. The numerical study was carried out with CFD KIVA-3V software, combined with the CANTERA code. In this study, diesel fuel was used as the reference fuel. In addition, the ABE were mixed with a magnetic stirrer in the ratio of 3:6:1 (acetone: butanol: ethanol) among themselves by volume. The ABE mixtures were tested after blending with diesel fuel at 20% and 50% by volume. As a result, in-cylinder pressure, heat release rate, combustion efficiency and soot emissions decreased with the increase of the ABE ratio in the mixture. Moreover, the combustion temperature distribution was more uniform, and the flame lift-off length increased [24].

When the literature is examined, it is seen that studies with ethanol diesel mixture are frequently encountered. However, numerical modeling of diethyl ether additives with ethanol-diesel mixtures and comprehensive combustion analysis studies are very limited. The aim of the study was numerically researched the effects of the addition of ethanol and diethyl ether to diesel fuel on the combustion characteristics, velocity distribution in the chamber and NO_x emissions. Depending on the change of fuel properties, the effect of different combustion fractions formed in the engine on NO emissions had been extensively studied in a DI diesel engine.

2. Numerical Study

In this study, 100% diesel fuel (D100) and by volume 90% diesel+10% ethanol blend (D90E10), 80% diesel+20% ethanol blend (D80E20), 80% diesel+10% ethanol+10% diethyl ether blend (D80E10DEE10) and 85% diesel+ 10% ethanol+5% diethyl ether mixture (D85E10DEE5) was used as fuel. These five different mixed fuels were tested at 2000 and 3000 rpm speed conditions. The physical and chemical properties of five different fuel types were given in Table 1.

Table 1. Properties of diesel fuel, ethanol and diethyl ether fuels [25,26]

Properties	Diesel fuel	Ethanol	Diethyl Ether
Chemical formula	C_xH_y	C_2H_6O	$C_4H_{10}O$
Oxygen content (% mass)	-	34,7	21
Density (g/cm³)	~0,83	0,789	0,713
Viscosity (mm²/s)	2,6-4,1	1,19	0,23
Boiling point (°C)	180-360	78,4	34,6
Sulfur content (ppm)	~250	—	—
Ignition temperature (°C)	315	235	160
Lower calorific value (kJ/kg)	42500	26800	33900
Latent heat of evaporation (kJ/kg)	250	825	356
Cetan number	40-55	5-8	~128
Theoric air/fuel ratio	14,6	9	11,1
Molecular weight	190-220	46,04	74,12
Carbon content (% mass)	87	52,2	64,9
Hydrogen content	13	13	13,5

ANTOR 3 LD 510 direct injection diesel engine was used within the scope of numerical study. The technical data of the engine were given in Table 2. The modeling was done by defining the initial boundaries in the ESE DIESEL section of the AVL FIRE software. Five different **mixed** fuels were defined from the library of the AVL FIRE software. In the modeling, WAVE model was used as spray model, k-zeta-f model was used as turbulence model and ECFM-3Z model was used as combustion model. The k-zeta -f turbulence model has been widely adopted for computational networks and flow conditions at any dimensionless distance close to the wall. The ECFM-3Z model can also be used for the combustion model with a combination of injection and EGR. ECFM-3Z is widely used in combustion analysis of direct injection engines [27-29]. Wave breakup model was used in the software. This model performs spray modeling depending on the physical and chemical properties of the used fuel. This model is used in injection simulation for diesel fuel and similar fuel types [30].

The intake temperature and intake pressure values at the initial conditions were defined as 293 K and 1 bar, respectively. The initial density of the ambient gas was calculated according to the ideal gas law. The velocities of the walls in all directions were defined as 0 m/s for the boundary conditions. In addition, the wall temperatures were taken as 450 K. In the boundary conditions, the type of fuel was

defined as the moving boundary condition by keeping the cylinder walls, cylinder head values, piston and all other variables constant. Thus, only the effect of fuel on combustion and NO emissions was examined.

Zeldovich mechanism was used for NO in the analysis. The thermal NO reaction mechanism was first described by Zeldovich as a two-stage reaction mechanism. Then, this mechanism was improved by adding the effects of OH radicals on thermal NO. The mechanism can be expressed as follows [31].

$$O + N_2 \leftrightarrow N + NO, k_{f1} = 1.8x10^8 e^{-38370/T}$$
$$k_{b1} = 3.8x10^7 e^{-425/T} \quad (1)$$

$$N + O_2 \leftrightarrow O + NO, k_{f2} = 1.8x10^4 Te^{-4680/T}$$
$$k_{b2} = 3.81x10^3 Te^{-20820/T} \quad (2)$$

$$N + OH \leftrightarrow H + NO, k_{f3} = 7.1x10^7 e^{-450/T}$$
$$k_{b3} = 1.7x10^8 e^{-24560/T} \quad (3)$$

Here k_{f1}, k_{f2} and k_{f3} are the forward reaction constants and k_{b1}, k_{b2} and k_{b3} are the backward reaction constants. The eq. (1) represents the thermal NO formation rate due to the high activation energy, which indicates the high temperature dependence of NO formation.

The wall interaction model known as "Walljet10" was used for all test fuels in the modelling. In all numerical studies, the spray angle was determined as 126°. In Figure 1, the combustion chamber geometry mesh structure of the test engine was given. Analyzes were performed on approximately 100000 cells.

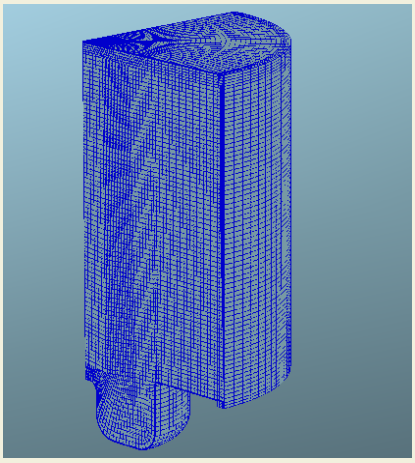

Figure 1. Mesh structure of chamber geometry

3. Results and Discussion

The effects of different fuel mixtures on combustion and emissions were investigated in the AVL-FIRE program at 2000 and 3000 rpm speed conditions. In the study, D100, D90E10, D80E20, D80E10DEE10 and D85E10DEE5 fuels were selected from the AVL library and defined to the software in different mixing ratios. The variation of in-cylinder pressures depending on the crank angle of the engine analyzed using different fuel mixtures was given in Figure 2. It was observed that the maximum in-cylinder pressures for all test fuels were obtained after the 725° CA. There are many parameters that affect the in-cylinder pressure distribution. Some of these can be listed as fuel density, cetane number, evaporation ability, ignition temperature and calorific value. When the in-cylinder pressure distributions were examined, it was seen that the maximum pressures were lower in all blended fuels compared to D100 fuel at both engine speeds. As seen in Table 1, this was because ethanol and diethyl ether have lower heating values than diesel fuel. For the 2000 rpm operating conditions of the engine, the maximum in-cylinder pressure values for D90E10, D80E20, D80E10DEE10 and D85E10DEE5 fuels compared to the D100 fuel decreased by 0.5%, 1.3%, 3.5% and 2%, respectively. For the engine's 3000 rpm operating conditions, the decreased in maximum pressures of D90E10, D80E20, D80E10DEE10 and D85E10DEE5 fuels compared to Diesel fuel were 0.5%, 1%, 3% and 1.7%, respectively.

Table 2. Technical properties of the test engine

Engine Name	Antor 3 LD 510
Engine Type	Four stroke, air-cooled, single-cylinder and direct injection diesel engine
Piston displacement	510 cm^3
Stroke x Bore	90 x 85 (mm x mm)
Compression ratio	17.5:1
Power	6.6@3000 (kW)
Torque	32.8@2000 (Nm)
Injection angle	126°
Injector hole number	4

Ethanol has a lower cetane number than diesel fuel. Especially low cetane number causes diesel knock in engines as well as worsening combustion. Due to this feature of ethanol, there are many studies where it is mixed with diesel fuel at low rates such as 10%, 20% and 30% [23,32]. Therefore, the selected ethanol-blended fuels did not cause significant pressure fluctuations in the diesel engine. Also, pressure distributions obtained using D100 fuel and ethanol blended fuels gave close results.

When the cumulative heat release curves are examined in Figure 3, it is seen that they are parallel with the in-cylinder pressure distributions. It could be said that the high calorific value of D100 fuel compared to other mixtures is effective especially in the maximum pressure and heat releases in the cylinder. It was observed that the heat release rates decreased with the increase in the ethanol ratio in the mixture. It could be said that this situation causes a decrease in in-cylinder temperatures.

As is known, diethyl ether has a low calorific value compared to D100 fuel, and diethyl ether has a high calorific value compared to ethanol fuel. At the same time, the low cetane number of ethanol fuel causes some disadvantages to the engine compared to D100 fuel [25]. In order to eliminate these problems, it was aimed to increase the cetane number of the mixture by adding 5% and 10% diethyl ether fuel to the ethanol fuel. According to the results of the analysis made in this direction, it was seen that the mixtures of D85E10DEE5 and D80E10DEE10 reduced the maximum heat release rates compared to D80E20, D90E10 and D100 fuels. It could be said that the cetane number affects this situation. The increase in the cetane number in the mixture increased the ignition ability of the fuel, shortened the ignition delay times and thus increased the maximum pressure and heat releases in the cylinder. On the other hand, the high heat of vaporization of DEE fuel could be demonstrated.

The turbulent kinetic energy/crank angle change of the engine using different fuels is seen at 2000 and 3000 rpm engine speeds (Figure 4). For all fuels, it was seen that the TKE value increases around TDC and decreases with the expansion stroke. When the results were examined, the highest TKE value was obtained for both engine speeds in the D80E20 mixed operation, and the lowest in the D80E10DEE10 mixture operation. When looking at D100 and other blended fuels in general, results were close to each other. The turbulent kinetic energy changes showed a 0.6% decrease in D90E10 fuel, a 2.7% decrease in D80E10DEE10 fuel, a 1% decrease in D85E10DEE5 fuel, and an increase of 0.05% in D80E20 fuel compared to the D100 fuel. Figure 4 shows the variation of turbulent kinetic energy (TKE) according to the crank angle obtained from different fuels at 3000 rpm operating conditions. Increasing engine speed and air movement caused the TKE value of the mixture to increase. In particular, the fuel injected into the cylinder with the movement of the piston towards the TDC caused the TKE value to increase in all test fuels. Decreased pressure and flow mobility with the development of combustion event and the movement of the piston towards the BDC caused the TKE value to decrease in all test fuels. At 3000 rpm engine speed, the highest TKE value was obtained in D90E10 mixed operation, and the lowest TKE value was obtained in D80E10DEE10 mixed operation.

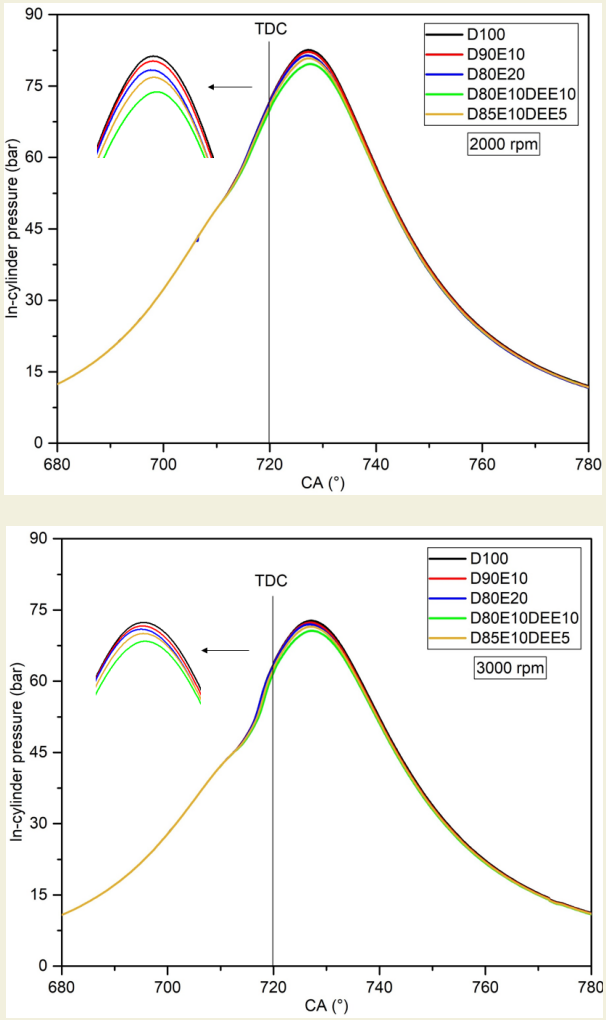

Figure 2. Variation of in-cylinder pressure according to crankshaft angle in different mixtures ratios at 2000 and 3000 rpm.

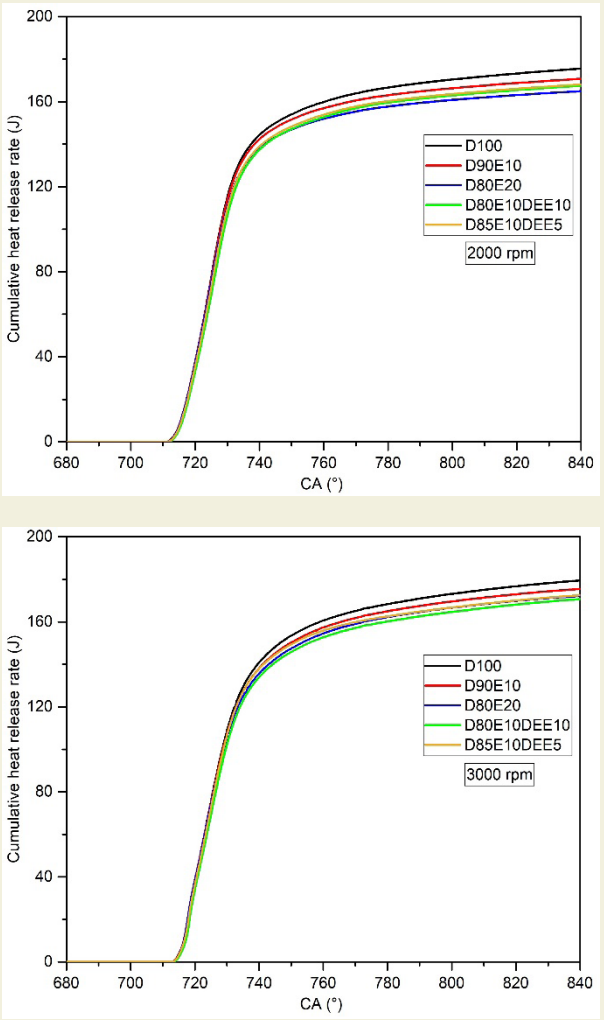

Figure 3. Variation of cumulative heat release rates according to crankshaft angle in different mixtures ratios at 2000 and 3000 rpm.

The variation of NO emissions according to the crank angle for different fuels is given in Figure 5. In parallel with the increase in in-cylinder temperature, NO emissions increased. There are many parameters that affect NO emissions in engines. Some of these are combustion temperature, excess air coefficient and burning duration. Especially the use of different fuels in engines causes these parameters to change and NO emissions to differ. All ethanol and diethyl ether additive test fuels reduced NO emissions compared to diesel fuel. This was thought to be due to the calorific value of the fuel. When the in-cylinder pressure and heat release rates were examined, the lowest value was obtained in the D80E10DEE10 fueled operation. It had been observed that NO emission was in parallel with the emission values. Although the DEE additive had a higher heating value compared to the ethanol additive, the maximum heat release rate and NO values were lower [14, 16]. This had been accepted as an indication of the complex process of combustion in the engine. It could be said that especially the high cetane number of DEE additive shortens the ignition delay time and caused a decrease in maximum pressure and temperatures. Therefore, NO emission decreased depending on the temperature. It would be expected that NO emissions would increase due to the oxygen they contain in the structure of diethyl ether and ethanol. However, the combustion end temperatures of ethanol and diethyl ether fuels decreased due to their low calorific value and high latent heat of evaporation compared to diesel fuel. NO emissions decreased D90E10, D80E20, D80E10DEE10 and D85E10DEE5 fuel compared to D100 fuel by 2%, 10%, 15% and 9% respectively. The variation of NO emission of test fuels at 3000 rpm speed condition is seen (Figure 5). Increased engine speed, causes an increase in the amount of injected fuel into the combustion chamber per unit time and an increase in in-cylinder temperatures. NO emission increased with increasing speed. In both speed conditions, lower NO emission was obtained in the blended fuels. When Figure 5 is examined, the lowest NO value was obtained for 3000 rpm in the D80E20 blended fuel study. In this case, the combustion end temperatures decreased due to the low calorific value and high latent heat of evaporation of the blended fuels compared to the D100 fuel. Therefore, NO emission decreased. For 3000 rpm engine speed, the reductions in NO emissions of D90E10, D80E20, D80E10DEE10 and D85E10DEE5 fuels com-

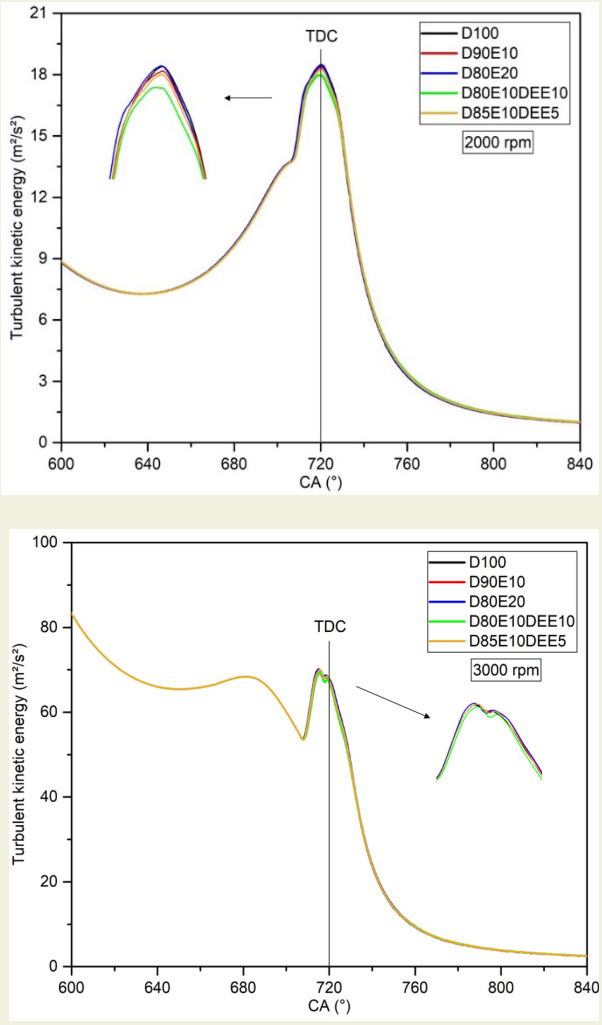

Figure 4. Variation of turbulent kinetic energy according to crankshaft angle in different mixtures ratios at 2000 and 3000 rpm.

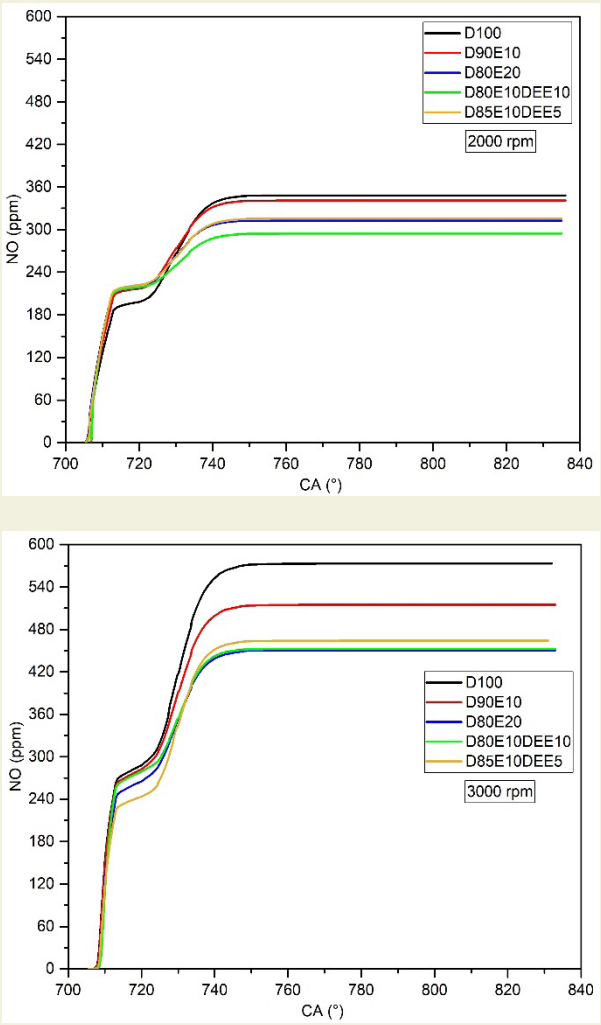

Figure 5. Variation of NO emissions according to crankshaft angle in different mixtures ratios at 2000 and 3000 rpm.

pared to diesel fuel were 10%, 21%, 20% and 16%, respectively.

Figure 6 shows the velocity distributions for five different fuels at different crank angles. In the simulations, the injection process for all test fuels took place in the crank angle range of 705-729°. Especially at the crank angle of 730°, it was seen that the spraying is completely stopped and the radial flow velocity is reduced for all test results. It was showed that the flow rate was maximum compared to other angles at the 720° crank angle. The increase in speed in the engine causes squish movements and swirl

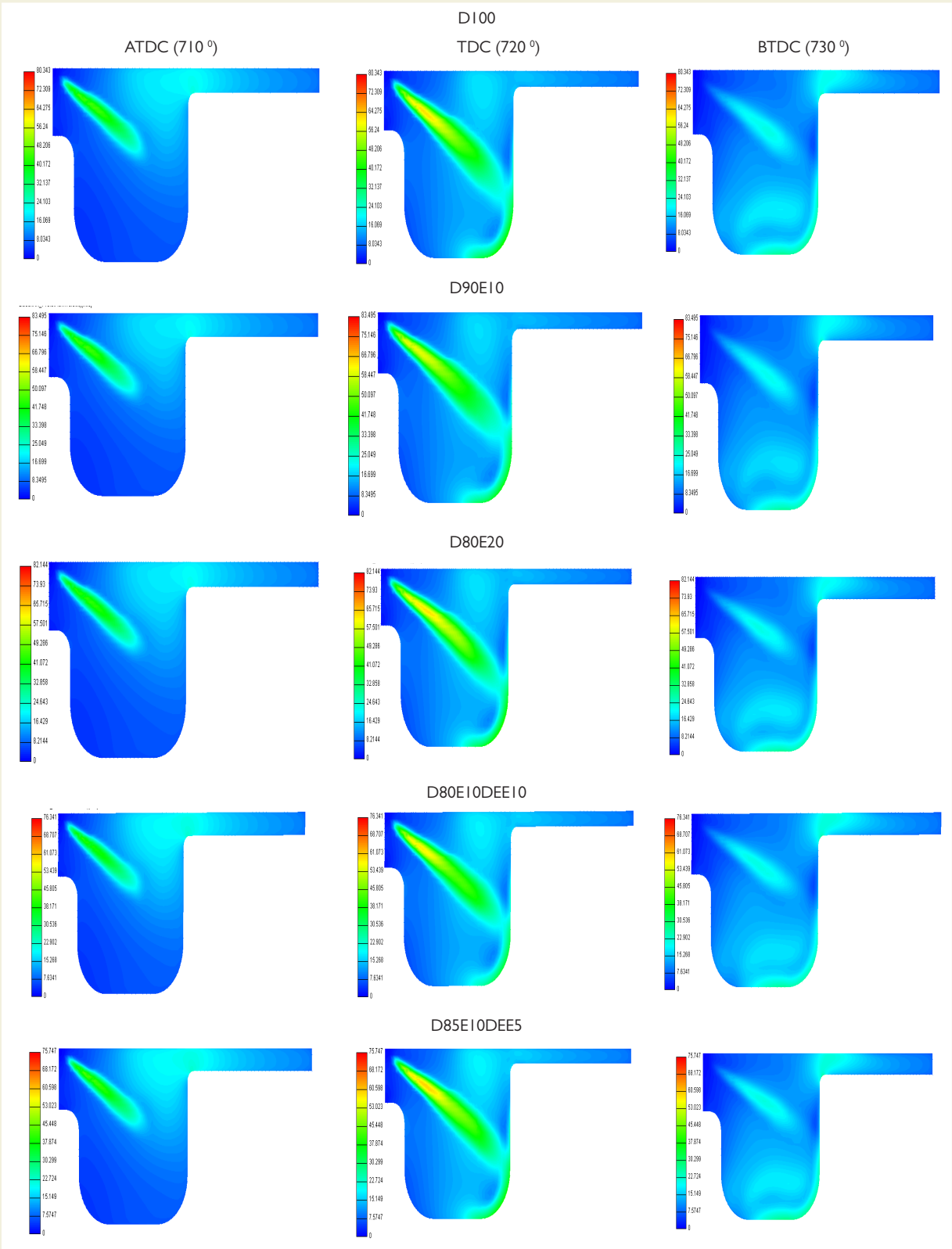

Figure 6. Speed distributions for five different fuels at 710°, 720° and 730° crank angles

rates to increase. Depending on both engine speed and piston movement, the velocity distribution of the fresh charge increased.

The velocity gradient of the fuel droplets sprayed into the combustion chamber varies depending on fuel viscosity, surface tension, droplet size and number, degree of evaporation and other factors (temperature, pressure and air flow mobility, etc.) in the combustion chamber.

At 3000 rpm speed condition, a slight increase in flow rate was obtained depending on the ethanol ratio added to the D100 fuel. On the other hand, the flow rate decreased with the addition of DEE to the blended fuels. This decrease is more clearly seen especially in the D80E10DEE10 mixture containing 10% DEE (Figure 6). As it is known, the density, surface tension and viscosity of fuel have important effects on the spray dynamics. Here, it was considered that the liquid + vapor interaction affects the fuel velocity distributions for all test fuels. Although ethanol has lower density and viscosity compared to diesel fuel, it can be said that diesel fuel, which shows early evaporation ability, breaks down more easily. This was thought to reduce the flow rate and inertia of diesel fuel. This approach supports velocity distribution graphs created by adding DEE to the mixture. In addition, when the flow velocity distributions of DEE added fuels were examined, a decrease was observed in the flow rate of DEE added fuels compared to diesel and diesel/ethanol mixtures.

4. Conclusions

In this study, in-cylinder pressure and heat release rate, TKE and NO analysis of four different mixed fuels (D90E10, D80E20, D80E10DEE10 and D85E10DEE5) and D100 fuel were performed. Depending on the change of fuel properties, the effects of different combustion fractions formed in the engine on NO emissions, which were extremely important for diesel engines, had been comprehensively discussed. In addition, velocity distributions of five different fuels in the combustion chamber were evaluated. Analyzes were made in the ESE DIESEL part of the AVL FIRE software. Engine speeds of 2000 and 3000 rpm were chosen as the operating condition. The obtained findings as a result of the study can be listed as follows.

- The maximum in-cylinder pressure of D100 fuel was higher than other blended fuels. The maximum in-cylinder pressure values for D90E10, D80E20, D80E10DEE10 and D85E10DEE5 fuels compared to the D100 fuel decreased by 0.5%, 1.3%, 3.5% and 2%, respectively, and for 3000 rpm were obtained 0.5%, 1%, 3% and 1.7%, respectively. This is because ethanol and diethyl ether have lower heating values than diesel fuel.
- The cumulative heat release rates obtained at 2000 rpm for D100, D90E10, D80E20, D80E10DEE10 and D85E10DEE5 fuels were 176.63 J, 171.65 J, 165.76 J, 168.46 J and 169.02 J, respectively. At 3000 rpm, these values were 180.55 J, 176.4 J, 173.05 J, 171.75 J and 173.51 J respectively. It was concluded that this situation was caused by the calorific value of diesel, diethyl ether and ethanol.
- NO emissions decreased D90E10, D80E20, D80E10DEE10 and D85E10DEE5 fuel compared to D100 fuel by 2%, 10%, 15% and 9%, respectively. At 3000 rpm, these values were 10%, 21%, 20% and 16%, respectively. The reason for this decrease was the lower calorific value and the high latent heat of vaporization of the mixtures compared to diesel fuel.
- The highest TKE value was obtained for 2000 rpm in D80E20 (0.05% increased) mixed fuel, and the lowest TKE value was obtained in D80E10DEE10 (2.7% decreased) mixed operation. At 3000 rpm, the values were close to each other, the highest TKE value was obtained in D90E10, and the lowest was obtained in D80E10DEE10. Ethanol had a positive effect on turbulent kinetic energy.
- The flow rate of ethanol was higher than diesel fuel. Diethyl ether was found to decrease the flow rate. This situation was due to the early evaporation ability of the fuel.

As a future study proposal on this subject, combustion chamber temperature, mass fraction burned, equivalence ratios and temperature distribution of the fuel injected into the combustion chamber at different crankshaft angles, engine performance curve and other exhaust emissions such as soot, CO_2, CO, HC can be analyzed.

5. References

[1] Calik, A. (2017). Pamuk yağı biyodizelinin motor ses seviyesine olan etkilerinin incelenmesi. Çukurova University Journal of the Faculty of Engineering and Architecture, 32(4): 147-152. https://doi.org/10.21605/cukurovaummfd.371016

[2] Calik, A. (2018). Hidrojen ile yakıt zenginleştirmenin dizel motorun motor performansı ve emisyon özelliklerine etkisi. Çukurova University Journal of the Faculty of Engineering and Architecture, 33(3): 255-262. https://doi.org/10.21605/cukurovaummfd.504771

[3] Carvalho, M., Torres, F., Ferreira, V., Silva, J., Martins, J., Torres, E. (2020). Effects of diethyl ether introduction in emissions and performance of a diesel engine fueled with biodiesel-ethanol blends. Energies, 13(15): 1-13. https://doi.org/10.3390/en13153787

[4] Wang, S., Viswanathan, K., Esakkimuthu, S., Azad, K. (2021). Experimental investigation of high alcohol low viscous renewable fuel in DI diesel engine. Environmental Science and Pollution Research, 28: 12026–12040. DOI: 10.1007/s11356-020-08298-y

[5] Sivalakshmi, S., Balusamy, T. (2013). Effect of biodiesel and its blends with diethyl ether on the combustion, performance and emissions from a diesel engine. Fuel, 106: 106–110. https://doi.org/10.1016/j.fuel.2012.12.033

[6] Ibrahim, A. (2018). An experimental study on using diethyl ether in a diesel engine operated with diesel-biodiesel fuel blend. Engineering Science and Technology, an International Journal, 21(5): 1024–1033. https://doi.org/10.1016/j.jestch.2018.07.004

[7] Pugazhvadivu, M., Rajagopan, S. (2009). Investigations on a diesel engine fuelled with biodiesel blends and diethyl ether as an additive. Indian Journal of Science and Technology, 2(5): 31-35. DOI:10.17485/ijst/2009/v2i5/29462

[8] Verma, T.N., Nashine, P., Chaurasiya, P.K., Rajak, U., Afzal, A., Kumar, S., Singh, S.V., Azad, A. (2020). The effect of ethanol-methanol-diesel-microalgae blends on performance, combustion and emissions of a direct injection diesel engine. Sustainable Energy Technologies and Assessments, 42: 1-20. https://doi.org/10.1016/j.seta.2020.100851

[9] Venu, H., Madhavan, V. (2017). Influence of diethyl ether (DEE) addition in ethanol-biodiesel-diesel (EBD) and methanol-biodiesel-diesel (MBD) blends in a diesel engine. Fuel, 189: 377–390. https://doi.org/10.1016/j.fuel.2016.10.101

[10] Sugash, G., Rubalingam, S., Kumar, U.P., Kumar, G.V., Akashragam, L. (2019). Investigation of performance and emissions of DI diesel engine with cottonseed biodiesel along with diethyl ether. International Journal of Ambient Energy, 1-4. DOI: 10.1080/01430750.2019.1630308

[11] Nishanth, S., Gunasekar, N., Nanthakumar, S., Prakash, R., Kumar, T.S. (2020). Experimental investigation on performance and emission characteristics of VCR engine working with biodiesel and diethyl ether. Materials Today: Proceedings, 45(2): 836-840. https://doi.org/10.1016/j.matpr.2020.02.913

[12] Ayhan, V., Tunca, S. (2017). The effect of diethyl ether-diesel blends a direct injection diesel engine on performance and emissions. Sakarya University Journal of Science (SAUJS), 22(2): 710-718. Doi: 10.16984/saufenbilder.321228

[13] Loganathan, M., Madhavanb, V., Balasubramanianc, K.A., Thanigaiveland, V. (2020). Investigation on the effect of diethyl ether with hydrogen-enriched cashew nut shell (CNS) biodiesel in direct injection (DI) diesel engine. Fuel, 277: 1-12. https://doi.org/10.1016/j.fuel.2020.118165

[14] Sezer, İ. (2018). A review study on the using of diethyl ether in Diesel engines: effects on NOx emissions. International Journal of Automotive Engineering and Technologies, 7(4): 164-183. https://doi.org/10.18245/ijaet.475044

[15] Sezer, İ. (2019). A review study on using diethyl ether in diesel engines: Effects on fuel properties, injection, and combustion characteristics. Energy & Environment, 31(2): 179-214. https://doi.org/10.1177/0958305X19856751

[16] Sudhakar, S., Sivaprakasam, S. (2014). Experimental investigation on combustion characteristics of di diesel engine using diethyl ether fumigation with ethanol blended diesel. International Journal Of Renewable Energy Research, 4(4): 872-878.

[17] Banapurmath, N.R., Khandal, S.V., RanganathaSwamy, L., Chandrashekar, T.K. (2015). Alcohol (ethanol and diethyl ethyl ether)-Diesel blended fuels for Diesel engine applications-A feasible solution. Advances in Automobile Engineering, 4(1): 1-8. Doi:10.4172/2167-7670.1000117

[18] Usta, N., Can, O., Ozturk, E. (2005). Comparison of biodiesel and ethanol as an alternative diesel engine fuel, Journal of Engineering Sciences, 11(3): 325-334.

[19] Xiong, J., Li, C. (2019). Study on emission of dimethyl ether engine by Avl-fire. Earth and Environmental Science, 252: 1-9. Doi: 10.1088/1755-1315/252/4/042006

[20] Iliev, S. (2015). A comparison of ethanol and methanol blending with gasoline using a 1-D engine model. Procedia Engineering, 100: 1013–1022. https://doi.org/10.1016/j.proeng.2015.01.461

[21] Mohan, B., Yang, W., Yu, W., Tay, K.L., Chou, S.K. (2015). Numerical simulation on spray characteristics of ether fuels. Energy Procedia, 75: 919-924. https://doi.org/10.1016/j.egypro.2015.07.243

[22] Yılmaz, M. (2019). Comparison of ethanol and gasoline in engine cylinder flow, M.Sc thesis, Bursa Uludağ University, Institute of science and technology, Bursa, Turkey.

[23] Rajak, U., Nashineb, P., Verma, T.N. (2020). Numerical study on emission characteristics of a diesel engine fuelled with diesel-spirulina microalgae-ethanol blends at various operating conditions. Fuel, 262: 1-20. https://doi.org/10.1016/j.fuel.2019.116519

[24] Xu, Z., Duan, X., Liu, Y., Denga, B., Liu, J. (2020). Spray combustion and soot formation characteristics of the acetone-butanolethanol/diesel blends under diesel engine-relevant conditions. Fuel, 280: 1-17. https://doi.org/10.1016/j.fuel.2020.118483

[25] Sezer, I. (2017). Experimental investigation the effects of ethanol and diethyl ether addition into diesel fuel on engine performance and exhaust emissions. J. of Thermal Science and Technology, 37(1): 61-68.

[26] Paul, A., Bose, P.K., Panua, R., Debroy, D. (2015). Study of performance and emission characteristics of a single cylinder CI engine using diethyl ether and ethanol blends. Journal of the Energy Institute, 88(1): 1-10. https://doi.org/10.1016/j.joei.2014.07.001

[27] Dimitriou, P., Wang, W., Peng, Z. (2015). A piston geometry and nozzle spray angle investigation in a di diesel engine by quantifying the air-fuel mixture. Int. J. Spray Combust. Dyn., 7: 1–24. https://doi.org/10.1260/1756-8277.7.1.1

[28] Soni, D.K., Gupta, R. (2017). Numerical analysis of flow dynamics for two piston bowl designs at different spray angles. J. Clean. Prod., 149: 723-734. https://doi.org/10.1016/j.jclepro.2017.02.142

[29] Soni, D.K., Gupta, R. (2016). Numerical investigation of emission reduction techniques applied on methanol blended diesel engine. Alexandria Eng. J., 55: 1867-1879. https://doi.org/10.1016/j.aej.2016.02.019

[30] Temizer, I. (2020). The combustion analysıs and wear effect of biodiesel fuel used in a diesel engine. Fuel, 270: 1-9. https://doi.org/10.1016/j.fuel.2020.117571

[31] Bashtani, J., Seddighi, S., Bahrabadi-Jovein, I. (2018). Control of nitrogen oxide formation in power generation using modified reaction kinetics and mixing. Energy, 145: 567-581. https://doi.org/10.1016/j.energy.2017.12.143

[32] Jayaprabakar, J., Anish, M., Beemkumar, N., Mathew, A., George, A.A. (2017). Effect of diethyl ether blended with neem oil methyl esters in CI engine. International Journal of Ambient Energy, 40: 116-118. https://doi.org/10.1080/01430750.2017.1372814

EUROPEAN MECHANICAL SCIENCE
e-ISSN: 2587-1110

RESEARCH ARTICLE

Deflection analysis of functionally graded equal strength beams

Mustafa Halûk Saraçoğlu[1*], Gökhan Güçlü[2], Fethullah Uslu[3]

[1,2,3]Kütahya Dumlupınar University, Faculty of Engineering, Department of Civil Engineering, Kütahya, Turkey

Orcid: M.H. Saraçoğlu (0000-0003-3842-5699), G. Güçlü (0000-0003-2931-9501), F. Uslu (0000-0001-8057-5119)

Abstract: In this study, equal strength cantilever and simply supported beams made of functionally graded material (FGM) whose material properties vary along the thickness direction were investigated. Equal strength cantilever FGM beams were loaded with uniformly distributed load and a point load at the tip and simply supported FGM beams were loaded with uniformly distributed loads. They all have variable cross-sections and a straight axis. For calculating equivalent material properties of FGMs, power-law distribution and the Mori-Tanaka model were used. A computer program was developed for the analysis of the problem. The dimensionless deflection values for cantilever beams and simply supported beams were obtained for different materials with the help of the developed computer program. Obtained results are presented in tables and graphs which, may be helpful for the researchers.

Keywords: Functionally graded material (FGM); Mori-Tanaka model; equal strength beam; variable cross-section.

1. Introduction

Beams are mainly used for carrying vertical loads. In general, moment and shear forces are the main determinants of the deformations and stresses caused by the loading. The bending moment of the beam is variable along the beam axis. While the beam sections are designed, a constant cross-section can be selected according to the maximum bending moment value, or a variable cross-section can be used in accordance with the bending moment. If the beam is designed by keeping the maximum bending stress constant in all cross-sections along the axis, the cross-section will be reduced where the bending moment is small and will increase where the bending moment is large. These types of beams are called equal strength beams and materials are saved because of their variable cross-sections.

If equal strength beams are used, the cross-section area will be reduced. This will result in material savings and a reduction in the weight of the beam. The basic logic of the FGM is to make a composite material by changing the microstructure from one material to another with a particular gradient. This ensures that the new material created has the best properties of the constituent materials. Studies have shown that FGM's effectively increases systems' resistance to thermal effects, corrosion, fatigue, fracture, and stress cracking [1,2].

There are previous studies on equal strength beams. Many basic books about the strength of materials or mechanics of materials have sections about this subject. Inan, Bakioğlu covers the subject in their books [3,4].

Due to its useful features, research on FGM is continuing intensively. Özarslan found the equations of motion of a functionally graded plate made of zircon and aluminum materials by making the Navier solutions according to the classical plate theory and found the natural frequencies by making free vibration analyzes of plates in different combination ratios and different sizes in his graduate study [5]. Ersan investigated the behavior of functionally graded discs under thermal load by analytical and numerical analysis methods in her graduate study [6]. Kadoli et al. studied the static analysis of functionally graded beams using higher-order shear deformation theory [7]. Chauhan and Khan have published a review paper on the analysis of beam-type structures made of functionally graded material [8]. Alagöz et al. made a study about functionally graded materials and their usage areas [9]. Arslan et al. investigated the free vibration analysis of straight axis beams made of bidirectional functionally graded material (FGM) in frequency space [10]. In the study of Sınır and Çevik, linear and non-linear natural frequencies of the axially polynomial functionally graded beam by considering the non-linear Euler-Bernoulli beam theory were obtained [11]. Çalım studied the free vibration analysis of axially functionally graded beams with variable cross-sec-

* Corresponding author.
Email: mhaluk.saracoglu@dpu.edu.tr

European Mechanical Science (2022), 6(2): 119-128
https://doi.org/10.26701/ems.1015629
Received: December 6, 2021 — Accepted: March 24, 2022

tions [12]. Rezaiee-Pajand et al. investigated the static behavior of non-prismatic sandwich beams composed of functionally graded materials [13]. Atmane et al. studied the free vibration behavior of exponential functionally graded beams with varying cross-sections [14].

In engineering fields such as aerospace, mechanical, and civil engineering, beams with variable cross-sections are commonly used. This study investigates the design of straight axis cantilever and simple beams with equal strength, made of functionally graded materials using different ceramic and metal materials. Equations of elastic curves of the beams are obtained.

A program is written for the analysis of beams examined using Matlab software. Results are obtained by using the developed codes. The obtained results were compared with the finite element program and the accuracy of the solution was demonstrated.

2. MATERIALS AND METHODS

The geometry of a functionally graded prismatic beam is shown in Figure 1. The *x*, *y*, and *z* axes are taken in width, height, and length directions, respectively. Since the geometry of the beam is symmetrical with respect to the vertical y-axis, the acting loads are in the yz plane.

In the study, it is assumed that the beam material behaves linearly elastic and small deformations occur.

As presented in Figure 1b, phase transitions of ceramic and metal materials functionally graded material along the cross-section height can be assumed as quasihomogeneous ceramic-metal layers and a continuous variation of the volume fraction of ceramic or metal materials.

2.1. Functionally Graded Materials

The functionally graded beam is typically made of ceramic and metal. It is assumed that with the thickness of the beam, the material properties vary. There is ceramic material on the upper surface of the beam and metal material on the lower surface.

The volume ratio distribution of functionally graded materials is as follows:

$$P = P_c V_c + P_m V_m \tag{1}$$

$$V_c + V_m = 1 \tag{2}$$

$$P = P_c + V_m (P_m - P_c) \tag{3A}$$

$$P = P_m + V_c (P_c - P_m) \tag{3B}$$

Material properties for ceramic and metal are shown with symbols, P_c and P_m, respectively. V_c and V_m are the material volume fractions of ceramic and metal [16].

There are several models developed to determine the material properties of FGM. Some of them are material distributions depending on various functions such as power-law distribution, sigmoid distribution, and exponential distribution [17]. The power-law distribution is given by

$$P(y) = P_c + \left(\frac{y}{h} + \frac{1}{2}\right)^n (P_m - P_c) \tag{4}$$

where *n* is a non-negative real number called the power-law index which identifies the material variation profile through the thickness of the beam.

In this study, material properties vary along the thickness dimension of the beam according to the power-law distribution.

The metal volume fraction is expressed as $V_m = \left((y/h) + (1/2)\right)^n$ according to the power-law distribution.

For the given fraction formula, metal distribution along the thickness direction for different power-law indices is given in Figure 2.

Many different models have been proposed to homogenize the mechanical properties of functionally graded materials [18,19]namely, Voigt (V. The Mori-Tanaka model was used in this study. Because this model is one of the most common homogenization techniques for modeling effective material properties. According to this model, the equivalent modulus of elasticity *E* is calculated as in equation (5):

$$E = \frac{9KG}{3K + G} \tag{5}$$

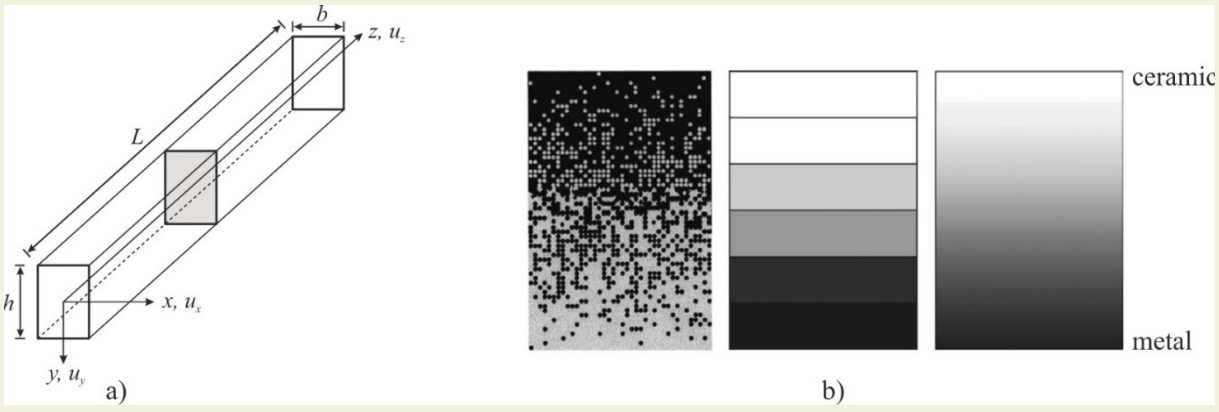

Figure 1. The geometry of a functionally graded beam and material distribution in cross-section [15,16].

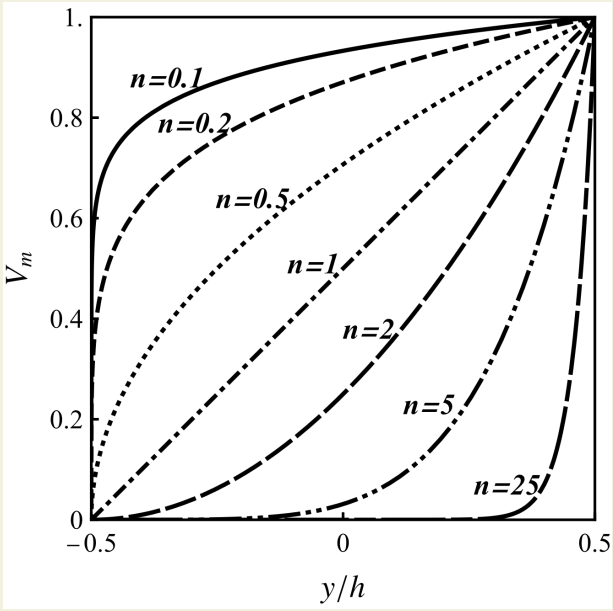

Figure 2. Value of metal volume fraction along the thickness direction depending on the index n.

In this expression, K denotes the bulk modulus and G denotes the shear modulus. According to the Mori-Tanaka model, these modules are expressed as follows [18,20].

$$\frac{K-K_c}{K_m-K_c}=\frac{V_m}{1+(1-V_m)\dfrac{3(K_m-K_c)}{3K_c+4G_c}}$$

$$\frac{G-G_c}{G_m-G_c}=\frac{V_m}{1+(1-V_m)\dfrac{G_m-G_c}{G_c+f}} \qquad (6)$$

$$K_{c,m}=\frac{E_{c,m}}{3(1-2\nu_{c,m})} \qquad G_{c,m}=\frac{E_{c,m}}{2(1+\nu_{c,m})}$$

$$V_m=\left(\frac{y}{h}+\frac{1}{2}\right)^n \qquad f=G_c\frac{9K_c+8G_c}{6(K_c+2G_c)}$$

In this expression, K_m is the bulk modulus of the metal phase and K_c is the bulk modulus of the ceramic phase. G_c is the shear modulus of the ceramic phase.

V_c and V_m are the volume ratios calculated according to equation (2) depending on the thickness coordinate of the ceramic and metal material, respectively, and indicate the material distribution.

2.2. Equal Strength Beams

Internal forces in a general beam are one axial force, two shear forces, one torsion moment, and two bending moments. Due to these internal forces, stresses (σ, τ), strains (ε, γ), and elastic curve (vertical displacements u) occur. According to the Euler-Bernoulli beam theory, also called classical beam theory, bending moment M_x and shear force S_y are dominant in beams. Other internal forces are often not very effective. On the deformation of the beam, bending is more effective than the others.

The bending moment in the beam varies along the beam axis. While the beam sections are being designed, a constant section can be determined according to the maximum bending moment in the beam or a variable section can be designed with the bending moment variation. If the beam is designed by keeping the maximum absolute value of stress as constant in all cross-sections along the axis, the cross-section will decrease in places where the bending moment is small, and the cross-section will increase in places where it is large. Such beams are called equal strength beams.

For beams of equal strength, the ratio of bending moment to the first moment of area is constant as stated in equation (7) [3,4].

$$\sigma_{\max}=M_x(z)/W_x(z)=\sigma_{\text{allow}}=\text{constant} \qquad (7)$$

In this expression, $W_x(z)$ is the first moment of area that varies along the beam axis z. It can be expressed mathematically by equation (8).

$$W_x(z)=M_x(z)/\sigma_{\text{allow}} \qquad (8)$$

If the bending moment variation of the loaded beam is determined, the variation function of the first moment of area can be obtained from the condition that all sections are of equal stress. With this obtained function, variation of the cross-section that supply the condition was presented. The cross-section variation can be along with the height, width, or both.

First moment of area of a rectangular cross-section can be calculated in equation (9)

$$W_x(z)=\frac{I_x}{h_z/2}=\frac{b_z h_z^3/12}{h_z/2}=\frac{b_z h_z^2}{6} \qquad (9)$$

The cantilever beam loaded with uniform load and a point load at the tip and simply supported beam loaded with the uniformly distributed load as shown in Figure 3 are chosen as example problems.

If the ratio of bending moments to required first moment of area is substituted as stated in equation (7), the expression becomes for the cantilever beam loaded with uniform load, a point load at the tip and simply supported beam loaded with uniformly distributed load respectively:

$$\text{constant}=\frac{M_x(z)}{W_x(z)}=\frac{-\frac{qL^2}{2}+qLz-\frac{qz^2}{2}}{\frac{b_z h_z^2}{6}}=\frac{-3q(L-z)^2}{b_z h_z^2} \qquad (10A)$$

$$\text{constant}=\frac{M_x(z)}{W_x(z)}=\frac{-P(L-z)}{\frac{b_z h_z^2}{6}}=\frac{-6P(L-z)}{b_z h_z^2} \qquad (10B)$$

$$\text{constant}=\frac{M_x(z)}{W_x(z)}=\frac{-\frac{q}{2}(z^2-Lz)}{\frac{b_z h_z^2}{6}}=\frac{-3q(z^2-Lz)}{b_z h_z^2} \qquad (10C)$$

If the section width $b_z=b_0$ is constant and the section

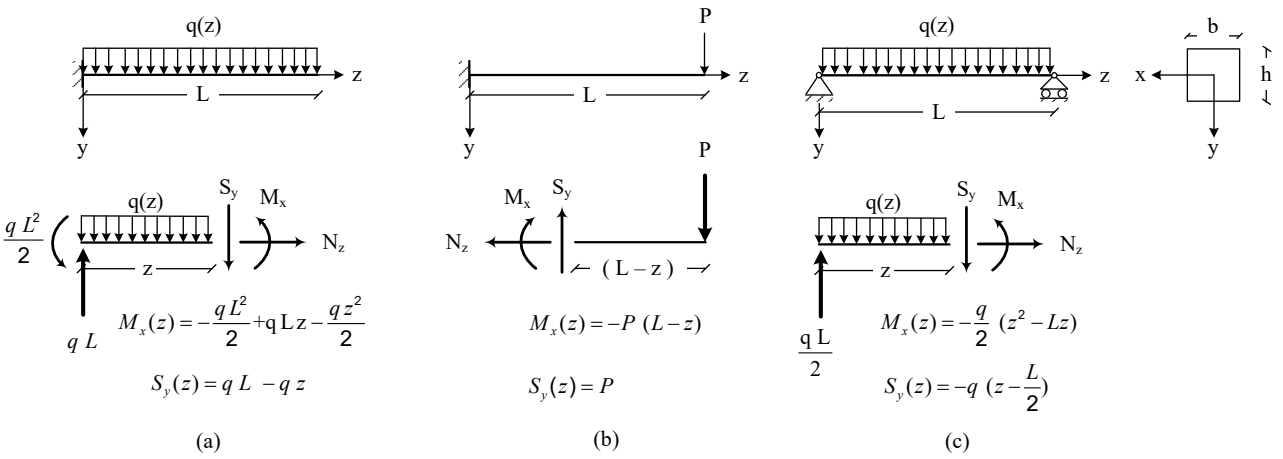

Figure 3. Beams with loads; (a) Uniform loaded cantilever beam (b) Point loaded cantilever beam (c) Uniform loaded simply supported beam [21].

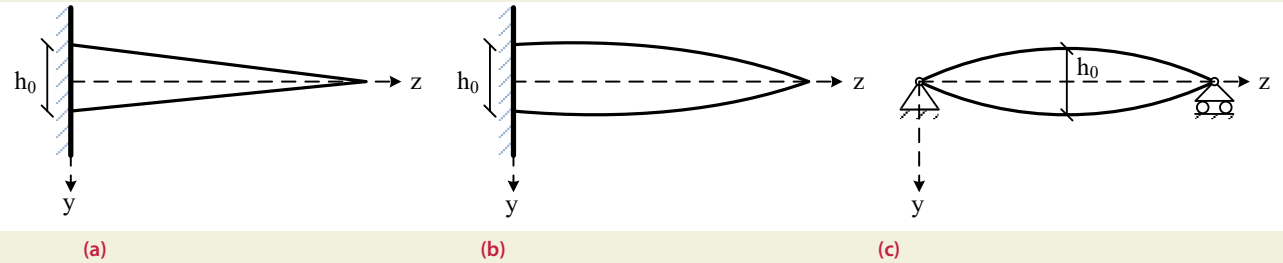

Figure 4. The schematic representation of the cross-section height of beams. (a) Uniform loaded cantilever beam (b) Point loaded cantilever beam (c) Uniform loaded simply supported beam.

height h_z is chosen as a variable in the variable beam section, and if the section height for the cantilever beam z=0 at the fixed support and for the simply supported beam z=L/2 at the mid-point is defined as h_0, then the variable section height function will be for distributed loaded cantilever, point loaded cantilever and distributed loaded simple beams respectively as in equations below:

$$z=0\Rightarrow\frac{-3q(L-z)^2}{b_0h_z^2}=\frac{-3q(L-0)^2}{b_0h_0^2}\quad\Rightarrow\quad h_z=\frac{h_0(L-z)}{L}\tag{11A}$$

$$z=0\Rightarrow\frac{-6P(L-z)}{b_0h_z^2}=\frac{-6P(L-0)}{b_0h_0^2}\quad\Rightarrow\quad h_z=\sqrt{\frac{L-z}{L}}\,h_0\tag{11B}$$

$$z=\frac{L}{2}\Rightarrow\frac{-3q\left(z^2-Lz\right)}{b_0h_z^2}=\frac{-3q\left(\left(\frac{L}{2}\right)^2-L\left(\frac{L}{2}\right)\right)}{b_0h_0^2}\quad\Rightarrow\quad h_z=\sqrt{\frac{4z(L-z)}{L^2}}\,h_0\tag{11C}$$

The schematic representation of the cross-section height of beams, whose section width is uniform and height varies as in equations, is as in Figure 4.

With this calculated section height function of the beams, the moment of inertia will be for distributed loaded cantilever, point loaded cantilever, and distributed loaded simple beams respectively as in equations (12):

$$I_x=\frac{b_0h_z^3}{12}=\frac{b_0}{12}\left(\frac{h_0(L-z)}{L}\right)^3=\frac{b_0h_0^3}{12}\left(\frac{L-z}{L}\right)^3=I_0\left(\frac{L-z}{L}\right)^3\tag{12A}$$

$$I_x=\frac{b_0h_z^3}{12}=\frac{b_0}{12}\left(\sqrt{\frac{L-z}{L}}\,h_0\right)^3=\frac{b_0h_0^3}{12}\left(\frac{L-z}{L}\right)^{3/2}=I_0\left(\frac{L-z}{L}\right)^{3/2}\tag{12B}$$

$$I_x=\frac{b_0h_z^3}{12}=\frac{b_0}{12}\left(\sqrt{\frac{4z(L-z)}{L^2}}\,h_0\right)^3=\frac{b_0h_0^3}{12}\left(\frac{4z(L-z)}{L^2}\right)^{3/2}=I_0\left(\frac{4z(L-z)}{L^2}\right)^{3/2}\tag{12C}$$

I_0 is the moment of inertia of the section at the fixed support point of the cantilever beams and at the mid-point of the simply supported beam in these expressions. Using the virtual work method, the critical displacements of the distributed loaded cantilever, point loaded cantilever, and distributed loaded simple beams are respectively as in equation (13).

$$\delta_{tip}=\frac{6qL^4}{Eb_0h_0^3}\tag{13A}$$

$$\delta_{tip}=\frac{8PL^3}{Eb_0h_0^3}\tag{13B}$$

$$\delta_{mid}=\frac{(\pi-2)3qL^4}{16Eb_0h_0^3}\tag{13C}$$

A computer program was developed with the help of MATLAB program within the scope of the study and the results were obtained using developed codes. In the first part of the computer program index n, the height of the cross-section h, Young's Modulus and Poisson's ratio of ceramic material and the metal material is taken from the user as input variables. With the help of the Mori-Tanaka model, the equivalent modulus of elasticity $E_{equivalent}$ was calculated with the volume modulus K and shear modulus G, according to this model. The developed computer program calculates the critical displacements using the virtual work method for three types of problem options; uniformly loaded cantilever beam, point loaded cantilever beam, and uniformly loaded simply supported beam. The flowchart of the program is shown in Figure 5.

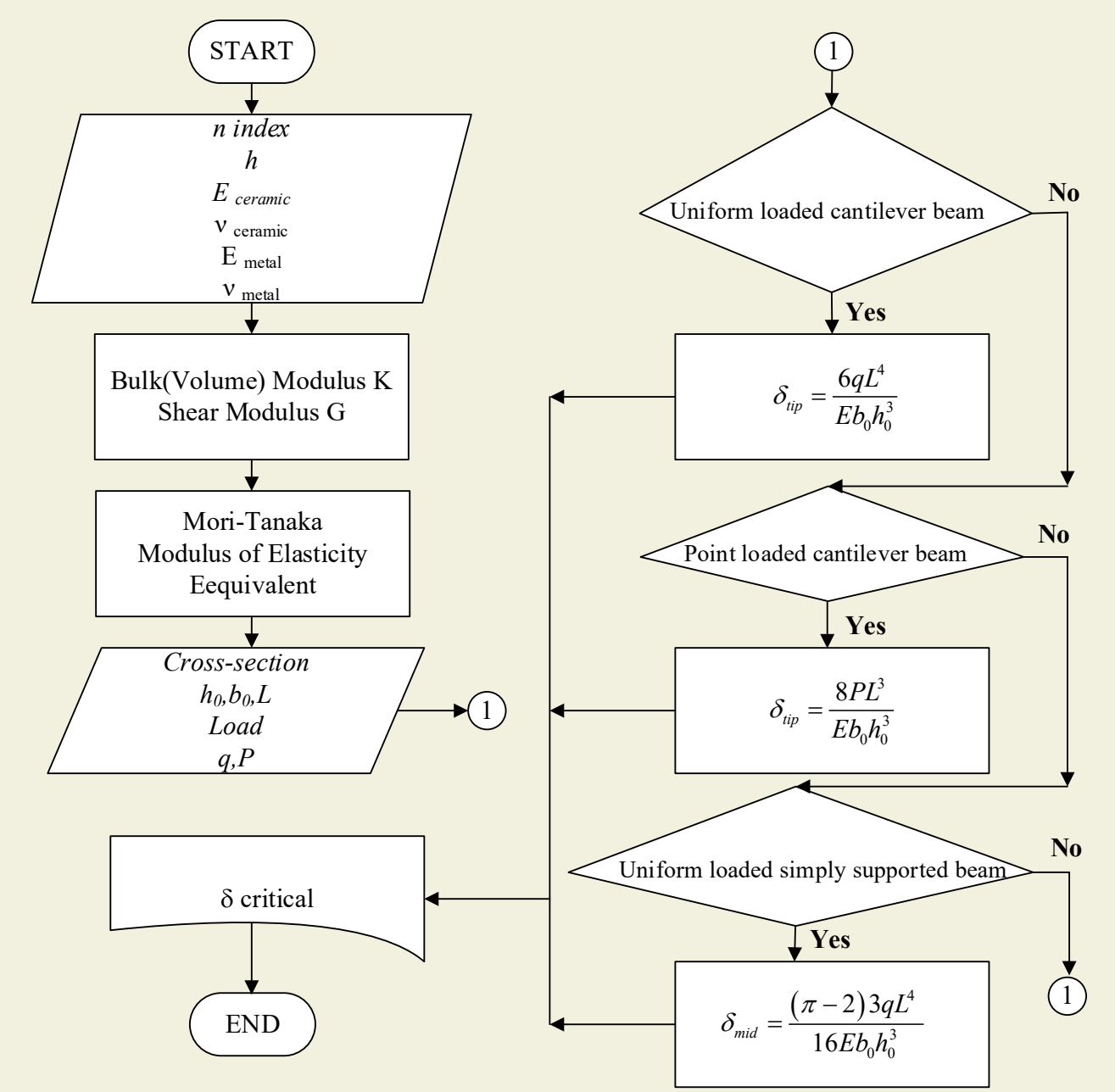

Figure 5. Flow chart of the developed computer program.

3. Results and Discussion

As an example, equal-strength cantilever functionally graded beam loaded with distributed load and point load and uniformly distributed loaded and equal-strength simply supported functionally graded beam loaded with uniformly distributed load are considered. The width of the beam, whose geometry is shown in Figure 1, is considered as b=0.1m and its height as h=0.1m. The length of the beam is L = 1m. In the problems, it is considered that point load P is 100 kN and uniformly distributed load q is 100 kN/m.

The calculated deflection values for point load and distributed load respectively are put in a dimensionless form by using equation (14).

$$\hat{u}_y = u_y \times \frac{E_m \times b \times h_0^3}{P \times L^3} \times 100$$
$$\hat{u}_y = u_y \times \frac{E_m \times b \times h_0^3}{q \times L^4} \times 100 \quad (14)$$

In this expression, E_m is the modulus of elasticity of the metal material.

Dimensionlessalizing of deflection values with the constant dimensions of the problems as b, h_0, L, P, and q can be calculated by using equation (15)

$$\hat{u}_y = u_y \times \frac{E_m \times 0.1 \times 0.1^3}{100 \times 1^3} \times 100 \quad \Rightarrow \quad \hat{u}_y = \frac{1}{10\,000} \times u_y \times E_m \quad (15)$$

In this expression, u_y is the deflection value as meter and

E_m is the Young's Modulus of metal material as kN/m^2.

Mechanical properties of ceramic and metal materials used for functionally graded materials are shown in Table 1 [20,22–26].

Table 1. Mechanical properties of ceramic and metal materials [20,22–26].

	Material	Young's Moduli (GPa)	Poisson's ratio
Ceramic	Zirconia (ZrO_2)	244.27	0.2882
	Titanium Carbide (TiC)	480.00	0.2000
	Aluminum Oxide (Al_2O_3)	349.55	0.2600
	Silicon Nitride (Si_3N_4)	348.43	0.2400
Metal	Stainless Steel (SUS304)	201.04	0.3262
	Nickel (Ni)	223.95	0.3100
	Aluminum (Al)	70.00	0.3100

In the functionally graded beam, ceramic and metal materials are used and the material properties vary with the beam's thicknes. Metal material is used at the bottom of the beam and ceramic material is used at the top.

The maximum dimensionless deflection values at the tip of the point loaded cantilever beam with variable cross-section depending on the variation in material distribution index n in the example whose material properties vary in the direction of beam height according to the power-law distribution are shown in Figure 6 b.

When the material distribution index n according to the power-law distribution is zero, the functionally graded beam is formed from completely ceramic (Figure 2). As can be seen from the calculations, the dimensionless deflection values are the maximum deflections in the all-ceramic beam models. As the index increases, the ceramic material will decrease in volume and the metal material will increase. When this value is 10, it can be considered that the cantilever beam is made of metal material. In the cantilever beam of equal strength and variable section, the maximum stress value in all sections along the beam axis is the same as the stress value at the fixed support point of the uniform section cantilever beam. As the index increases, the dimensionless deflection value at the tip point of the cantilever beam decreases (Figure 6). The behavior of the beam changes according to the mechanical properties of the ceramic and metal materials used in FGMs.

The dimensionless deflection functions for the material distribution index n of 0.2 in uniform cross-section and variable cross-section point loaded cantilever beams made of FGM using Aluminum Oxide (Al_2O_3) for ceramic material and Aluminum (Al) for metal material are shown in Figure7 b.

As can be seen in Figure7 b, the deflection of the point-loaded cantilever functionally graded (Al_2O_3 / Al) beam with the uniform section of height h_0 is less than the

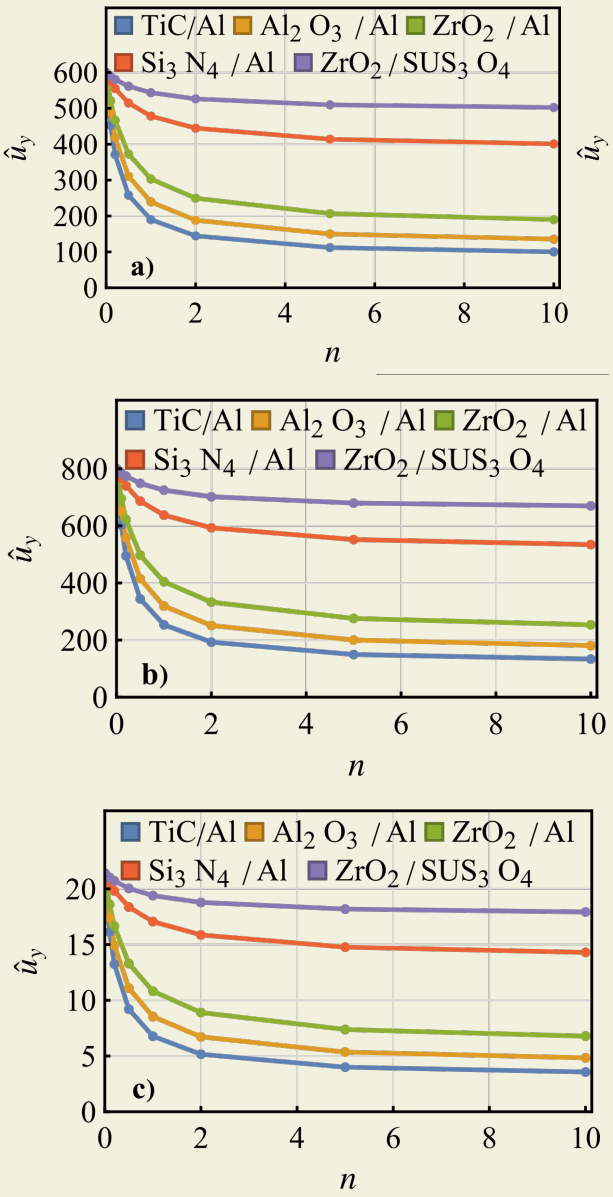

Figure 6. Distribution of dimensionless deflection values of equal strength functionally graded beams depending on the material distribution index n a) distributed loaded cantilever b) point loaded cantilever c) distributed loaded simply supported.

deflection of the equal strength beam with the same stress as this beam and a variable cross-section. While this variation is less in the fixed support, it is higher at the tip point of the cantilever beam where the point load is affected. A similar situation occurs for equal strength beams made of functionally graded materials using other ceramic and metal materials.

The maximum dimensionless deflection values at the tip of the distributed loaded cantilever beam with variable cross-section depending on the variation in material distribution index n in the example whose material properties vary in the direction of beam height according to the power-law distribution are shown in Figure 6 a.

As can be seen from the calculations, the dimensionless deflection value is the maximum for the all-ceramic beam

models. As the index n increases, deflection values decrease.

The dimensionless deflection functions for the material distribution index n of 0.2 in uniform cross-section and variable cross-section cantilever beams made of FGM using Aluminum Oxide (Al_2O_3) for ceramic material and Aluminum (Al) for metal material are shown in Figure7 a.

As can be seen in Figure7 a, the deflection of the distributed loaded cantilever functionally graded (Al_2O_3 / Al) beam with the uniform section of height h_0 is less than the deflection of the equal strength beam with the same stress as this beam and a variable cross-section. While this variation is less in the fixed support, it is higher at the tip point of the cantilever beam where the point load is affected. A similar situation occurs for equal strength beams made of functionally graded materials using other ceramic and metal materials.

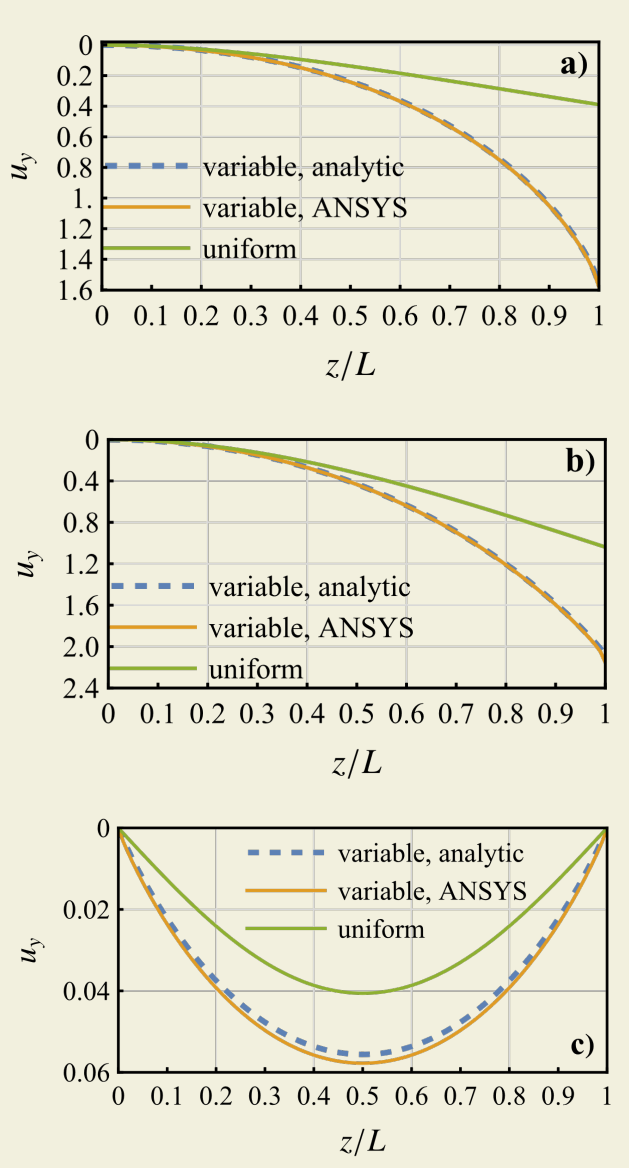

Figure7. Dimensionless deflection functions of functionally graded Al_2O_3/Al beams a) distributed loaded cantilever b) point loaded cantilever c) distributed loaded simply supported.

The variation with the dimensionless deflection values at the quarter-point of the simply supported beam with variable cross-section loaded with uniformly distributed load with the material distribution index n in the example whose material properties vary in the direction of beam height according to the power-law distribution are shown in Figure 6 c.

As can be seen from the calculations, the dimensionless deflection value is the maximum for the all-ceramic beam models as cantilever beams. As the index n increases, deflection values decrease.

The dimensionless deflection functions for the material distribution index n of 0.2 in uniform cross-section and variable cross-section simply supported beams made of FGM using Aluminum Oxide (Al_2O_3) for ceramic material and Aluminum (Al) for metal material are shown in Figure7 c.

As can be seen in Figure7 c, mid-point deflections are the same for variable and uniform cross-sections. Because they have the same section of height h_0 at the mid-point. While the deflection variation is less at the mid-point, it is higher at the supports of the simple beam where the height of the section decreases.

Table 2. Volume ratios of sample problems

Sample problem	Volume Ratio
Uniform loaded cantilever beam	0.500
Point loaded cantilever beam	0.667
Uniform loaded simply supported beam	0.785

The volumes of the equal strength beams are compared with the initial ones and the volume ratio is determined. A comparison of the volume savings of sample problems is shown in Table 2.

3.1. Verification with Finite Element Software ANSYS

Sample problems are modeled in the ANSYS program with the equivalent modulus of elasticity and equivalent Poisson's ratio. The dimensions of the example problems are taken the same as analytical studies.

The results obtained from the developed computer program were verified by the finite element software ANSYS solutions (Figure 8).

Table 3. Comparisons of the present solutions with ANSYS results of critical deflections.

Sample problem	Present	ANSYS	Difference
Uniform loaded cantilever beam	8.3045	8.4273	-1.46%
Point loaded cantilever beam	11.0726	11.4723	-3.48%
Uniform loaded simply supported beam	0.2963	0.3077	-3.72%

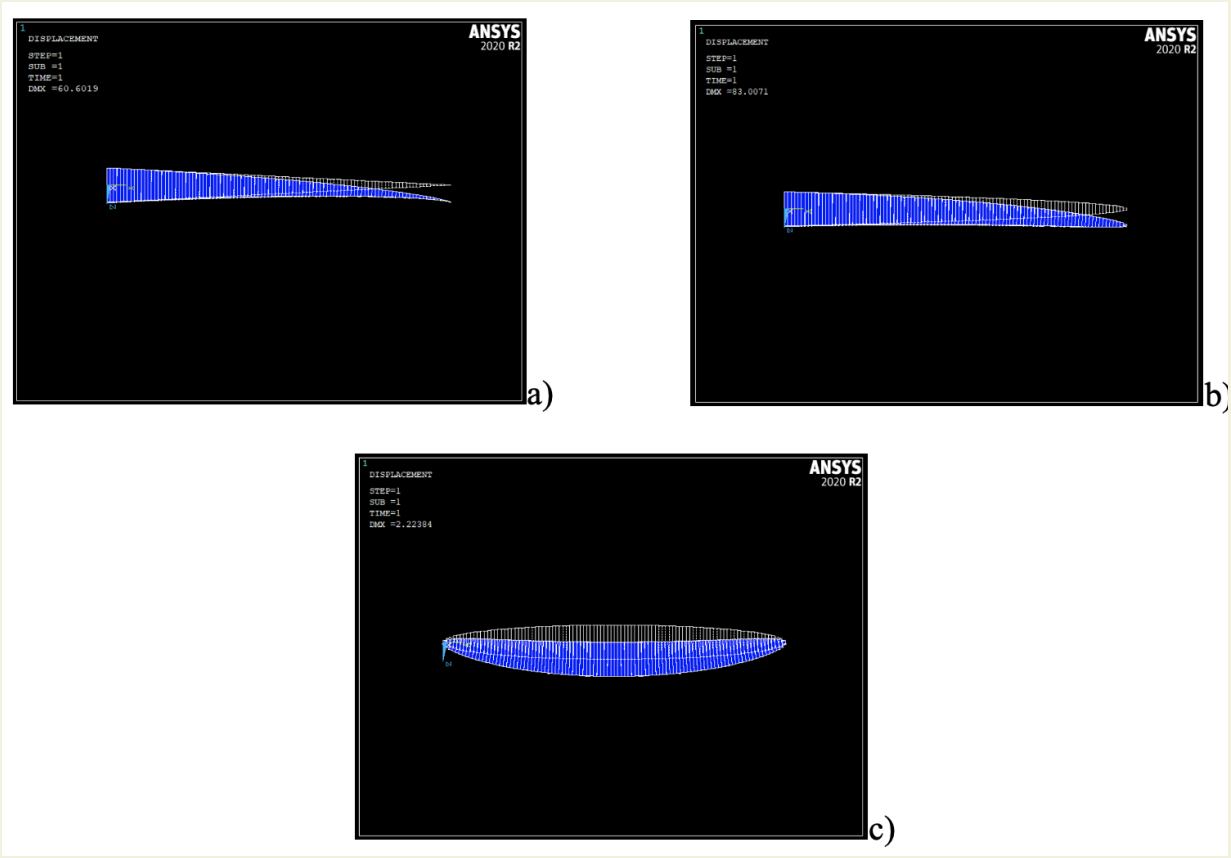

Figure 8. ANSYS solutions of discussed sample problems.

Dimensionless critical deflection values are given in Table 3 which are used for the verification of the sample problems.

There is a good agreement between the results of this study and ANSYS software results.

4. Conclusions

In this study, a computer program was developed. With the help of this program, the deflection functions of the equal-strength cantilever beam carrying a point load at the tip and equal-strength simply supported functionally graded beam loaded with uniformly distributed load made of FGM whose material properties vary with the height of the beams were obtained. The deflection values calculated for functionally graded beams with different ceramic and metal materials used in the literature have been made dimensionless and presented in the form of tables and graphics.

The material properties of FGMs have been modeled with different functions in the literature. In this study, the power-law distribution is considered. Mori-Tanaka model was used for the equivalent mechanical properties of the material.

The cross-sectional variation for the equivalent beam was calculated by keeping the stress constant calculated by the ratio of the bending moment to the required first moment of area. A function for beam height was obtained by keeping the beam width constant for the cross-section variation. Section height h_0 at the support of the cantilever beam and at the mid-point of the simple beam has decreased to zero along the beam axis according to this calculated function. Depending on this variation, the moment of inertia of the section and thus the bending stiffness were variable. The deflection function is obtained for equal strength beams made of FGMs. By giving some numerical values for the obtained function, the design of cantilever and simple beams of the variable cross-section with straight axis and equal strength made of different functionally graded materials is examined.

From the calculations, it is observed that when the index n increases the maximum deflection of the beam decreases. The maximum deflections of the problems of a cantilever beam with a point load at the tip and uniformly loaded simply supported beam with different ceramic and metal materials behave similarly. When the maximum deflection values for these problems are for the materials ZrO2/SUS304, for uniformly loaded cantilever beam problem it is for the materials of ZrO2/Al material.

As a result of this study, it is proved that it has been demonstrated that the flexibility of the FGM beam can be increased without reducing the strength by using equal strength beams made of functionally graded materials. In addition, analyses can be made for straight axis and equal strength variable cross-section beams made of FGM un-

der different boundary conditions and different loadings.

References

[1] Rajan, T.P.D., Pai, B.C., (2014). Developments in processing of functionally gradient metals and metal-ceramic composites: A review. Acta Metallurgica Sinica (English Letters). 27(5): 825–38. doi: 10.1007/S40195-014-0142-3.

[2] Boggarapu, V., Gujjala, R., Ojha, S., Acharya, S., Venkateswara babu, P., Chowdary, S., et al., (2021). State of the art in functionally graded materials. Composite Structures. 262: 113596. doi: 10.1016/J.COMPSTRUCT.2021.113596.

[3] İnan, M., (2001). Cisimlerin Mukavemeti. 8.bs., İstanbul: İTÜ Vakfı.

[4] Bakioğlu, M., (2009). Cisimlerin mukavemeti. 2.bs., Birsen Yayınevi.

[5] Özarslan, O., (2007). Fonksiyonel derecelendirilmiş bir plağın analizi. Yüksek Lisans Tezi, İstanbul Teknik Üniversitesi, (2007).

[6] Ersan, Ç., (2008). Fonksiyonel derecelendirilmiş disklerde termal gerilme analizi. Yüksek Lisans Tezi, Pamukkale Üniversitesi, (2008).

[7] Kadoli Ravikiran, A.K., (2008). Static analysis of functionally graded beams using higher order shear deformation theory. Applied Mathematical Modelling. 32: 2509–25. doi: 10.1016/j.apm.2007.09.015.

[8] Chauhan, P.K., Khan, I.A., (2014). Review on Analysis of Functionally Graded Material Beam Type Structure. International Journal of Advanced Mechanical Engineering. 4(3): 299–306.

[9] Alagöz, H., Güleç, M., Konez, A., (2004). Fonksyionel derecelendirilmiş malzemeler ve kullanim alanları. Mühendis ve Makina. 45(5): 25–32.

[10] Arslan, T.A., Noori, A.R., Temel, B., (2019). Çift Yönlü Fonksiyonel Derecelendirilmiş Malzemeli Timoshenko Kirişlerinin Serbest Titreşim Analizi. 21. Ulusal Mekanik Kongresi, p. 218–25.

[11] Sınır, S., Çevik, M., (2017). Eksenel Olarak Polinomiyal Fonksiyonel Derecelendirilmiş Malzemeden Nonlineer Euler-Bernoulli Kirişinin Serbest Titreşim Analizi. 20. Ulusal Mekanik Kongresi, p. 706–21.

[12] Çalım, F.F., (2017). Eksenel Fonksiyonel Derecelendirilmiş Değişken Kesitli Kirişlerin Serbest Titreşimi. 20. Ulusal Mekanik Kongresi, p. 84–91.

[13] Rezaiee-Pajand, M., Masoodi, A.R., Mokhtari, M., (2018). Static analysis of functionally graded non-prismatic sandwich beams. Advances in Computational Design. 3(2): 165–90. doi: 10.12989/acd.2018.3.2.165.

[14] Atmane, H.A., Tounsi, A., Meftah, S.A., Belhadj, H.A., (2011). Free vibration behavior of exponential functionally graded beams with varying cross-section. JVC/Journal of Vibration and Control. 17(2): 311–8. doi: 10.1177/1077546310370691.

[15] Saraçoğlu, M.H., Güçlü, G., Uslu, F., (2019). Static Analysis of Orthotropic Euler-Bernoulli and Timoshenko Beams With Respect to Various Parameters. Bitlis Eren Üniversitesi Fen Bilimleri Dergisi. 8(2): 628–41.

[16] İpci, D., (2014). Fonksiyonel Derecelendirilmiş Konik Kesitli Mikro - Kirişlerin Serbest Titreşim Analizi. Yüksek Lisans Tezi, Hacettepe Üniversitesi, (2014).

[17] Chi, S.H., Chung, Y.L., (2006). Mechanical behavior of functionally graded material plates under transverse load—Part I: Analysis. International Journal of Solids and Structures. 43(13): 3657–74. doi: 10.1016/J.IJSOLSTR.2005.04.011.

[18] Shen, H.S., Wang, Z.X., (2012). Assessment of Voigt and Mori-Tanaka models for vibration analysis of functionally graded plates. Composite Structures. 94(7): 2197–208. doi: 10.1016/j.compstruct.2012.02.018.

[19] Elishakoff, I., Demetris Pentaras, C.G., (2016). Mechanics of Functionally Graded Material Structures. World Scientific Publishing Co. Pte. Ltd. 5.

[20] Shen, H.-S., (2009). Functionally Graded Materials. Boca Raton: CRC Press.

[21] Saraçoğlu, M.H., Güçlü, G., Uslu, F., (2017). Ortotrop Kirişlerin Farklı Kiriş Teorileri ile Statik Analizi. 20. Ulusal Mekanik Kongresi, p. 351–61.

[22] Reddy, J.N., Chin, C.D., (2007). Thermomechanical Analysis of Functionally Graded Cylinders and Plates. Journal of Thermal Stresses. 21(6): 593–626. doi: 10.1080/01495739808956165.

[23] Kirlangiç, O., Akbaş, Ş.D., (2020). Comparison study between layered and functionally graded composite beams for static deflection and stress analyses. Journal of Computational Applied Mechanics. 51(2): 294–301. doi: 10.22059/JCAMECH.2020.296319.473.

[24] Sahu, A., Pradhan, N., Sarangi, S.K., (2020). Static and Dynamic Analysis of Smart Functionally Graded Beams. Materials Today: Proceedings. 24: 1618–25. doi: 10.1016/j.matpr.2020.04.483.

[25] Şimşek, M., Al-shujairi, M., (2017). Static , free and forced vibration of functionally graded (FG) sandwich beams excited by two successive moving harmonic loads. Composites Part B. 108: 18–34. doi: 10.1016/j.compositesb.2016.09.098.

[26] Banks-Sills, L., Eliasi, R., Berlin, Y., (2002). Vibration Characteristics of Functionally Graded Material Skew Plate in Thermal Environment. Composites: Part B. 33: 7–15.

EUROPEAN MECHANICAL SCIENCE
e-ISSN: 2587-1110

RESEARCH ARTICLE

Numerical simulation of a magnetic induction coil for heat treatment of an AISI 4340 gear

Önder Sönmez[1*], Deniz Kaya[1], Vladimir Bukanin[2], Aleksandr Ivanov[2]

[1]Akdeniz University, Faculty of Science, Department of Physics, Antalya, Turkey.
[2] Saint Petersburg Electrotechnical University, "LETI", St. Petersburg, Russian Federation.

Orcid: Ö. Sönmez (0000-0003-3356-5334), D. Kaya (0000-0002-1951-2466), V. Bukanin (0000-0002-0215-7621), A. Ivanov (0000-0002-9598-1344)

Abstract: In manufacturing industry, heat treatment is a fundamental requirement for improving the material quality of readily manufactured products. Induction heating technology is repeatable and easily controlled by the advantage of having an electronic control unit. Nowadays, numerical methods have gained so much importance that it becomes as a reference for the induction heating industry. Experimental methods are costly and time demanding procedures. However, making use of finite element method (FEA) software, induction heating simulations of a steel gear can be performed relatively cost effective and in a short time. In this paper, induction heating simulation of an AISI 4340 steel gear using FEA software is performed. The effect of variation of inductor frequency and air gap distance on the hardening depth of the gear surface is investigated. The temperature profile of the workpiece is obtained. From the temperature distribution on the steel gear workpiece, the regions of the gear at which the austenitizing temperature (Ac3) - responsible for martensite phase formation- are observed. From the numerical results, hardening profile and hardening depth of the gear is interpreted. During the induction and heating process, the temperature distribution on the AISI 4340 steel gear was determined, depending on the frequency change (medium frequency: 8 – 12 kHz) and the air gap variations (2 mm – 28 mm), using constant time (0.5 seconds), and constant coil power (220 kW). It is interpreted that as the coil frequency rise from 8 kHz to 12 kHz the temperature rises in the root region of the steel gear. This, consequently, leads to austenitizing temperature (800 °C) in deeper regions of the workpiece. On fixed time, constant power, and constant frequency (10 kHz), depending on the decrease in magnetic field effect, increasing the air gap from 2 - 28 mm led to reduced temperature in the root area (<800 °C).

Keywords: Induction heating; Numerical modelling; Hardness profile; Surface hardening; AISI 4340; Steel gear.

Nomenclature

AISI	American Iron and Steel Institute
FEA	Finite Element Analysis
4340	43 (1.8% Nickel, 0.8% Chrome, 0.25% Molybdenum) , 40 (0.4% Carbon)
ELTA	Electrothermal Analysis
CAD	Computer Aided Design
MF	Medium Frequency
HF	High Frequency
HV	Vickers Hardnes)
HRC	Rockwell Hardness on the C scale
Ac1	Lower Austenitizing Temperature
Ac3	Upper Critical Austenitizing Temperature

Greek letters

α	Temperature Resistance Constant
c_p	Specific Heat at Constant Pressure
f	Frequency
h	Heat Convection Coefficient
j	Current Density
k	Heat Conduction Coefficient
M	Modulus
μ_0	Magnetic Permeability İn Vacuum
μ_r	Magnetic Permeability İn Matter
n	Surface Normal Vector
q	Heat Flux
R	Radius
ρ	Density
ρ_0	Initial Resistivity
σ	Electrical Conductivity Coefficient
t	Time
T	Temperature
ω	Angular Frequency

1. Introduction

The technology of induction heating of gears emerged with the patent publication of W. Braun from the USA in 1926 and Vologdin V. P. from the Soviet Union in 1939 [1,2]. Nonetheless, the heat treatment dates too far more past, and it was long known and applied to improve

* Corresponding author.
Email: ondermetu@gmail.com

European Mechanical Science (2022), 6(2): 129-137
https://doi.org/10.26701/ems.1027181
Received: December 6, 2021 — Accepted: March 24, 2022

the mechanical properties of steel. High-carbon steel hardening has been used for thousands of years and this method is quite a basic procedure. Once the steel is heated sufficiently, and if it is immediately quenched into cold water, the steel workpiece turns into a reddish color. In this part, the steel apparently has a multicolored appearance and more importantly the mechanical properties are improved such as hardness. Although the heat treatment was in use since iron age, it was in the second quarter of 19th century whose mathematical methodology was fully comprehended. Yet, controlling the process electrically and full command on the consecutive physical phenomena was not well understood. But still, this heat treatment method was known for more than a hundred years [3]. This technology is commonly used for annealing, tempering, residual stress relieving and surface hardening of critical workpieces used in industry. The induction heating method for surface hardening has superiorities over alternatives due to its repeatability, eco-friendliness and being a practically rapid method [4,5].

Herein, numerical methods have gained as much importance as to become as a reference for the induction heating industry. Now due to numerical methods (finite element method, finite difference method), multiphysics simulation has been developed. This allows us to optimize the most important parameters of induction heating processes.

The induction heating multiphysics procedure involves the Faraday's law of induction, and resulting induction causes the eddy current which leads to the Joule effect phenomenon [6]. The result is the heating of the workpiece. These consecutive physical phenomena might seem simple; however, magnetic induction heating is quite a complicated phenomenon. For this reason, it is quite demanding procedure to design a magnetic induction heating system practically and usually it requires too many trials and error processes [7]. Besides, the experimental setup of magnetic induction system requires several equipment, e.g., temperature sensors, to place on various points through the workpiece. Apparently, these procedures and equipment take cost and time. In addition, the acquired data from sensors are not always reliable and precise regarding the experimental dynamics of the process. And with the same technique is required repeatedly for every single experiment.

Experimental methods are costly and time demanding due to the reasons mentioned above. However, using of finite element method software, induction heating simulations of a steel gear can be performed relatively cost effective and in a suitable time. While errors and mistakes during numerical experiment are costless, the numerical model can be optimized by sequential simulations and can be included into the manufacturing process [8]. Hence, the demand of numerical methods arises. In this multi-physical method, coupling of electromagnetic and thermal equations is complex and material properties are nonlinear. For this reason, many researchers put invaluable efforts to achieve a robust numerical solution for induction heating process [9]. There are simulation tools for induction heating system/component design which are readily being used in the academic studies [6,10,11]. An investigation on induction heating of AISI 4340 steel gear workpiece using simulation tool is carried out. In the induction heating system, the essentially focus was on the parameters such as hardening depth (mm) and power supply frequency (Hz). The numerical results and the plots of these results are obtained after performing consecutive simulations. In these plots, two valuable observable relations: expected hardening depth and coil excitement current-hardening depth are shown. Considerably fast numerical results owing to an additional numerical technique found in ELTA software are obtained [12].

2. Methods of Study

2.1. The Governing Equations

Transient heat conduction, Faraday induction law and Ohm law for joule heating is included in the model. In heat transfer modelling, to adopt more realistic approach, convection mode of heat transfer is included as well.

2-D transient heat transfer equation (Eq. 1), Faraday law of induction (Eq. 2) and Ohm's law (Eq. 3) are shown as following [13,14].

$$\rho c\frac{\partial T}{\partial t}+\nabla.\left(-k\nabla T\right)=q \tag{1}$$

$$j\omega\sigma A-\mu^{-1}\left(\nabla^2 A\right)=J_0 \tag{2}$$

$$\sigma=\frac{1}{\left|\rho_0\left(1+\alpha\left(T-T_0\right)\right)\right|} \tag{3}$$

where, ρ is mass density, c is specific heat capacity, T is temperature, k is thermal conductivity coefficient, q is auxiliary heat flux, j is current density, ω is angular frequency, σ is electrical conductivity coefficient, T_0 is ambient temperature, A is magnetic vector potential, μ is magnetic susceptibility of medium, ρ_0 is initial resistivity, J_0 is source current density applied for the coil and α is temperature coefficient of resistance.

Eq. (1) turns into Eq. (4) when convection and radiation modes of heat transfer is included into 2-D heat transfer equation [15].

$$k\frac{\partial T}{\partial n}+\alpha\left(T^4-T_0^4\right)+\beta\left(T-T_0\right)=0 \tag{4}$$

where, α is Boltzmann Constant and β is convection coefficient.

Skin effect is an active phenomenon when the current is alternating, and in this phenomenon the alternating current tends to flow nearer the outer surface of the conduc-

tor as the frequency of the alternative current increases. The skin (penetration) depth (δ) is expressed as in Eq. (5) [6].

$$\delta = \sqrt{2/(\omega\mu\sigma)} \tag{5}$$

Skin depth, denoted as δ, refers to 1/e of its value at the surface of the conductor. The current density in the conductor is expressed as in Eq. (6) [16],

$$j = j_0 * exp(-x/\delta) \tag{6}$$

Skin effect is a directly related phenomenon and can be mathematically expressed by the two equations Eq. (5,6). The current density in the material attenuates as the distance from surface increases. The skin depth is a function of frequency and material properties, as seen in Eq. (5). As the frequency increases, the depth of current density decreases. In Eq. (6), one can have an insight into how the current density near the surface of the material behaves as a function of radial distance. These two equations are direct outcomes of AC current.

2.2. The Material Properties and Simulation Setup

The material characteristics determine the skin (penetration) depth. The magnetic permeability (μ) and the electrical conductivity or specific resistance (ρ) of the material are temperature dependent. Using this property, controlling the skin (penetration) depth becomes practicable. AISI 4340 steel is a type of ferromagnetic material with a higher relative magnetic permeability, which enables a smaller skin effect. The composition of the ferromagnetic material highly affects the property of magnetic permeability (μ). The other factor that determines the magnetic permeability is the Curie temperature, above which the material loses its magnetization [15]. Due to the loss of magnetization, the skin depth suddenly increases in this condition (760 ^{0}C). The Curie temperature is critical through the induction heating process for this reason.

The AISI 4340 material is a low alloy steel containing nickel chromium and molybdenum elements. AISI 4340 steel is highly suitable for induction heating due to its alloy element and carbon content that contribute to hardening. AISI 4340 steel is a commonly known material in terms of toughness, high hardness after heat treatment, as well as fatigue resistance properties. Typical field of use of AISI 4340 steel is mainly, aerospace industry: landing gears of airplanes, gear wheels, shafts, and other structural elements for power transmission [15,17-19]. A proper identification of material properties is extremely important for a robust numerical simulation. For this reason, transformation temperatures and critical temperatures should be known for AISI 4340 steel material. In Table 1, the material properties of the AISI 4340 steel material are shown below.

Table 1. Material properties for AISI 4340 steel

Heat Rate [°C/s]	Ac1 [°C]	Ac3 [°C]	Acm [°C]
2739	726	983	1058
814	787	982	1048
427	778	949	1038
99	768	856	910

The AISI 4340 steel is a high strength material mostly preferred as gear material due to its superior mechanical properties. In the content of this alloy, the presence of chromium, nickel, and molybdenum enables the alloy to be suitable for induction heating process for surface hardening [3]. AISI 4340 is also commonly known for its toughness, high strength, and fatigue resistance. The heat treatment of AISI 4340 has therefore of great importance. The chemical composition of AISI 4340 steel is given in Table 2. by element and the percentage.

Table 2. Chemical composition of AISI 4340 steel

Element	Fe	Ni	Cr	Mn	C	Mb	Si	Cu
Percentage (wt. %)	95.99	1.61	0.88	0.6	0.42	0.29	0.18	0.03

The simulation procedure is illustrated as a flow chart which is given in Figure 1.

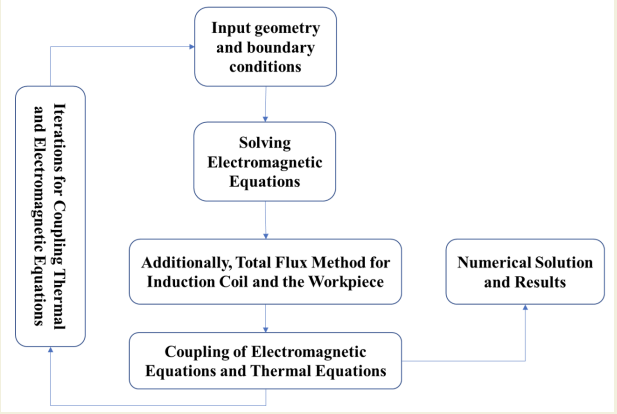

Figure 1. The flow chart of the overall simulation procedure.

In algorithm of ELTA 7.0 Software, finite difference method is used to obtain the solution of coupled electromagnetic and thermal equations. Additionally, in the numerical solution process, an analytical method "Total Flux Method" is introduced to account for the coil and workpiece. This additional analytical method is proposed by V. Nemkov [1].

In ELTA software, half part of the single tooth is taken as workpiece geometry due to symmetry (Figure 2).

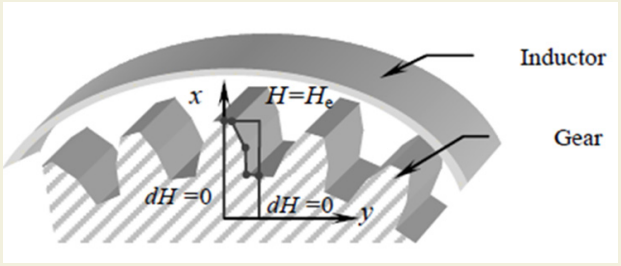

Figure 2. 2-D geometry model for calculation in ELTA software [20]

The internal part of electro-thermal problems is solved by considering geometrical symmetry, i.e., only 1/2 part of one gear tooth is calculated. ELTA 7.0 calculates in this part of workpiece the two-dimensional distribution of power sources and temperature.

The non-linear differential equation for magnetic field H and temperature T are described as:

$$\frac{\partial}{\partial x}\left(\rho \frac{\partial \dot{H}}{\partial x}\right) + \frac{\partial}{\partial y}\left(\rho \frac{\partial \dot{H}}{\partial y}\right) = j\omega\mu\mu_0 \dot{H} \quad (7)$$

$$C_v \frac{\partial T}{\partial t} = \frac{\partial}{\partial x}\left(\lambda \frac{\partial T}{\partial x}\right) + \frac{\partial}{\partial y}\left(\lambda \frac{\partial T}{\partial y}\right) + w, \quad (8)$$

where ρ – electrical resistivity, ω – angular frequency, μ – permeability, x, y – coordinates of workpiece cross-section, C_v – volume specific heat, λ – thermal conductivity, w – heat source density, T – temperature, t – time. The boundary conditions are known magnetic strength H_e on the surface in the air gap between inductor and gear, symmetry in central parts of face and bottom ($dH = 0$), super-magnetic ($H = 0$) or normal component of current is equal to 0 in the main body of a gear wheel (line $x = 0$) and temperature-dependent heat losses on the gear surface during the forced cooling stage, included in the program database.

As illustrated in Figure 2, the path of the profile of the gear tooth is represented by 5 points with 4 straight lines. For gear parameters the setting window is shown in Figure 3.

The gear parameters in this study: AISI 4340 steel is the material of the gear, outside diameter is (Do) 10.52 cm, root diameter (Dr) is 8.67 cm, the interior diameter (Dint) is 1 cm, face width (Zg) is 0.65 cm and pitch diameter (Dp) are 9.595 cm. The number of teeth of the gear (N) is 48. The processing parameters are shown in the Figure 4 below. The processing parameters are: 220 kW power of power source and a range of frequency 8-10-12 kHz.

As given in Figure 5, the interior radius of the inductor (R1) is 5.71 cm (11.42 cm diameter) with a turn number 1. The profile of the inductor is selected as 6.5 x 30 x 3 mm. The simulation time setting is 0.5 seconds. The geometry of the inductor is a hollow rectangle with a gap in the middle of its cross section for water cooling. Re indicates exterior radius of the workpiece.

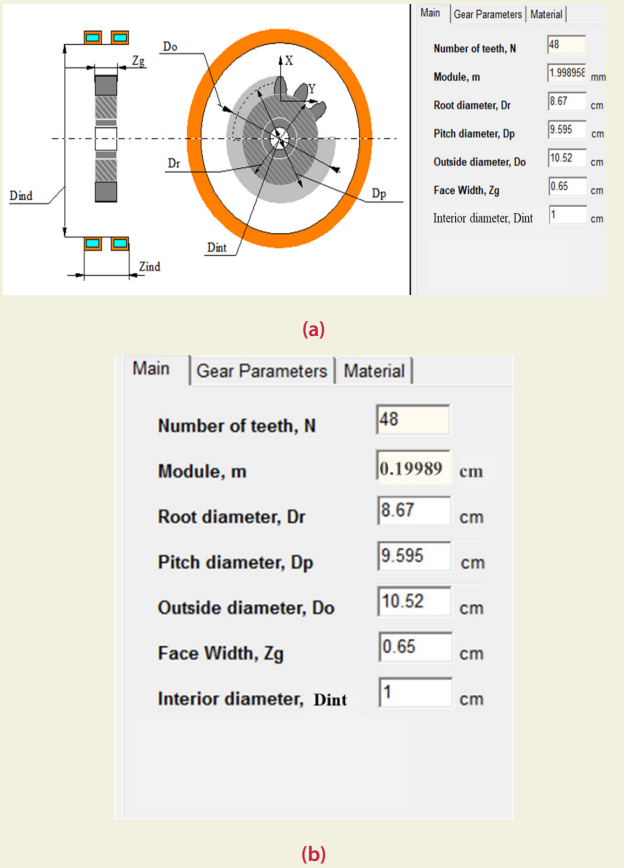

Figure 3. (a) Gear geometry and dimensions (b) Input parameters window

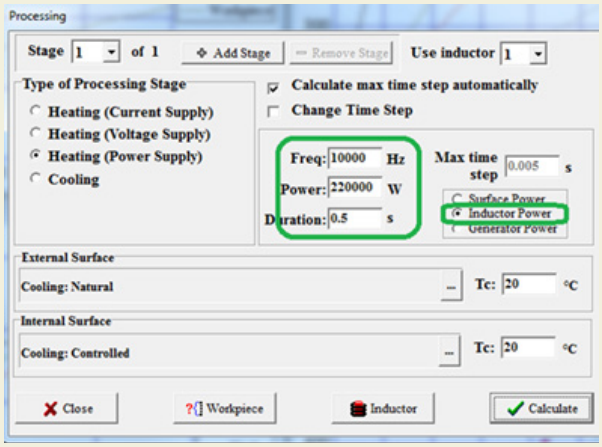

Figure 4. Gear processing settings in ELTA

The temperature distribution in the AISI 4340 steel gear workpiece was analyzed using ELTA software, using inputs of 220 kW of power, 10 kHz coil frequency, 4.54 mm clearance distance and 0.5 seconds simulation time. The temperature behavior is obtained for three different frequencies (8, 10 and 12 kHz).

There are numerous numbers of research findings that propose medium frequency (MF) of alternating current

frequency range is preferably used in practice [9,17,21-24]. As a result of simulation outcomes which made grounds for this paperwork, a couple of kHz of frequency (MF) for alternating current range, a couple of kW power, a few millimeters of airgap distance have offered a desirable depth of penetration of temperature which is required for a considerable depth of hardness. In this study, these simulation parameters and geometry dimensions are replicated by modelling the same case taken from one of an academic paper of Noureddine Barka [25]. This mentioned study is used for validation purpose which can be seen on Fig 11. After validating the current model using ELTA software and being ensured of the results referencing the study of Barka, N. [25] , a close range of these simulation parameters are swept parametrically in order to observe the effect of variation of inductor frequency and the air gap distance on the hardening depth of the gear surface.

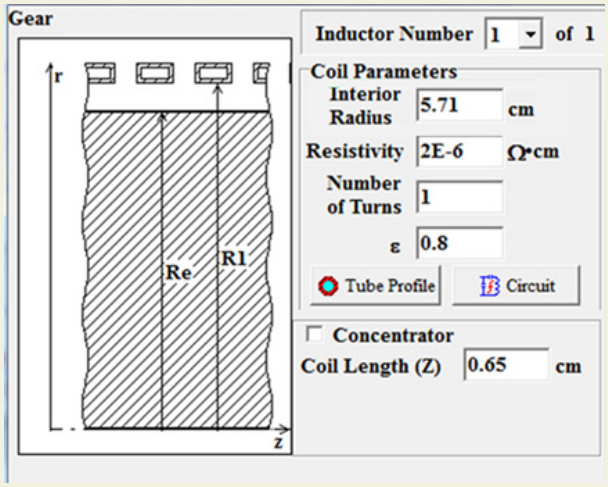

Figure 5. Inductor parameters

3. Results and Discussion

The parameter arrangements are determined by holding heating time and coil power fixed, and the coil frequency and air gap value. Under this arrangement the hardening depth for each case is obtained. The main goal was to achieve a minimum temperature over 800 ^{0}C (austenitizing temperature, Acm) and observe a uniform temperature distribution. For the parameter arrangements: heating time = 0.5 s, coil power 220 kW, coil frequency (8,10,12 kHz) and air gap value (2, 4.54, 7, 9, 11, 16, 20, 24, 28 mm) a set of cases between the combinations were performed among these parameters. The air gap of 4.54 mm value is the reference value from Barka, N. [25].

In case of 8 kHz coil frequency, the temperature in the root area of the 4340 steel gear workpiece reaches to 800 °C at a depth of 0.35 mm (Figure 6.a, cyan line limit). In the case where the coil frequency is 10 kHz, it is observed that the critical austenitizing temperature (800 °C) for martensite formation occurs at a depth of 1.48 mm, and if the frequency is increased to 12 kHz, this temperature is observed at a depth of 2.75 mm (See Figure 6.b and Figure 6.c, cyan line boundary). Therefore, as the frequency increased from 8 kHz to 12 kHz at three different frequencies, the martensite phase formation is observed at deeper regions. This formation of martensite phase is critical for fatigue and wear resistance for the workpiece. The change of the depth in which the austenitizing temperature occurs at a constant distance (4.54 mm) is shown in Figure 7.

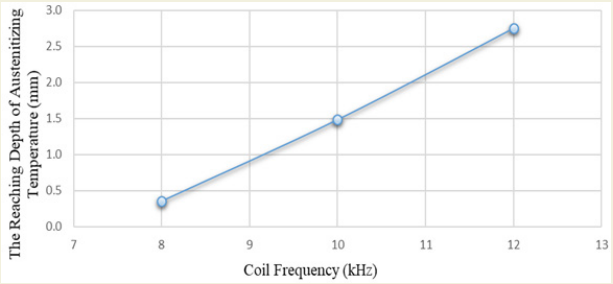

Figure 7. Change of the reaching depth of austenitizing temperature depending on the coil frequency

In the study, the effect of the air gap and the induction coil on the temperature distribution and hardness depth were examined. Therefore, the coil power (220 kW) coil frequency (10 kHz), heating time (0.5 seconds) were kept constant, and the air gap was changed (2, 4.54, 7, 9, 11, 16, 20, 24, 28 mm). The results were plotted, it is seen in figure 8 and three of these cases are shown as temperature in Figure 8.

In the case in which the air gap is 4.54 mm, a temperature of 800 ^{0}C was reached at a depth of 1.48 mm at the root region (Figure 8a). Since the magnetic field effect decreases due to the increase in the distance between the workpiece and the coil, the temperature increase on the workpiece is limited. Therefore, in cases where the air gap is 16 mm and 28 mm, the austenitizing temperature (800 ^{0}C) - required for martensite formation - occurs at a limited depth in the root region of the workpiece (Figure 8b and Figure 8c). In Figure 9, the formation depth of the austenitizing temperature versus air gap is given. As shown in Figure 9, increasing of the air gap leads to a decrease in the depth of martensite formation in the induction heating process. It is important in terms of wear resistance and fatigue resistance.

Consequently, a prescription of desired induction heating system parameters is carried out. The dimensions, appropriate power and the frequency parameters of the inductor, the air gap are well-defined as a result of this study. Applying the determined system parameters, the induction heating for the selected gear gives even temperature distribution and adequate depth of hardening. Furthermore, preparing all the simulation setup and obtaining the results were too simple by the help of rapid running ELTA software.

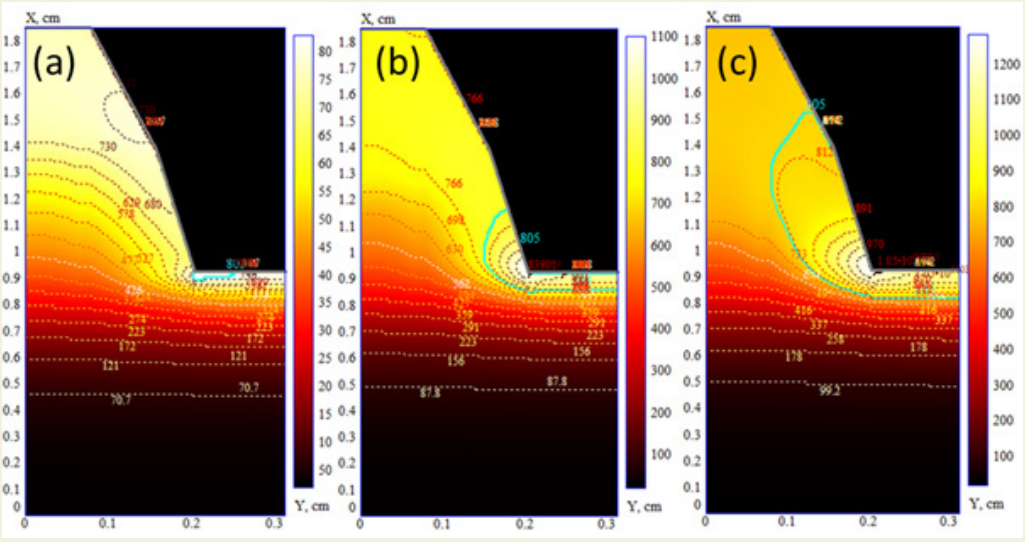

Figure 6. Fixed air gap (4.54 mm), heating time (0.5 seconds) and coil power (220 kW). The temperature distribution when coil frequency is (a) 8 kHz (b) 10 kHz (c) 12 kHz.

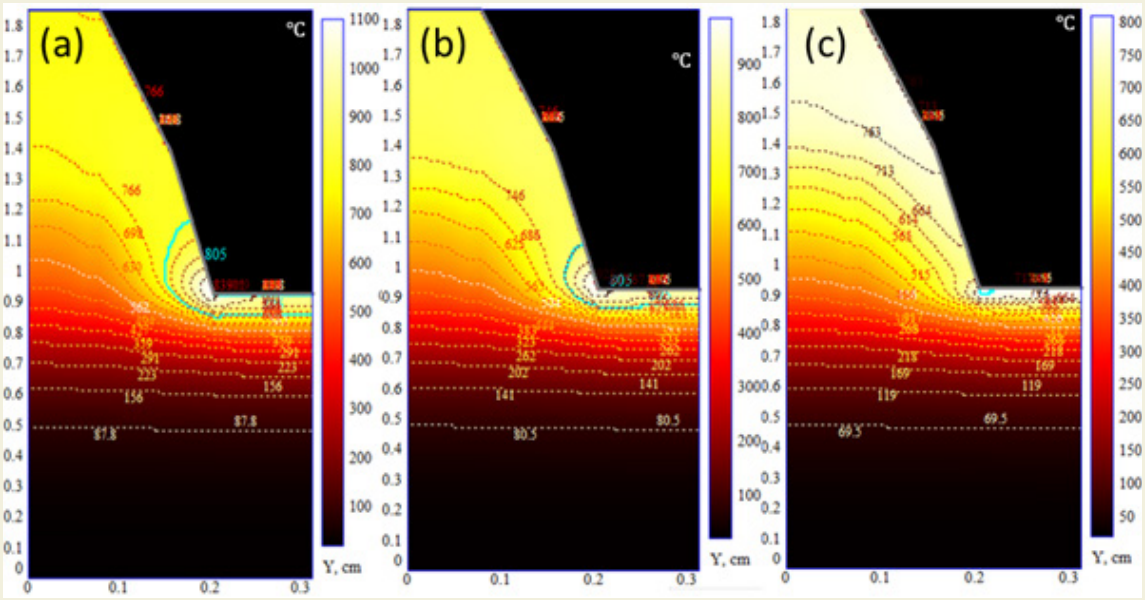

Figure 8. The effect of three different values of the air gap using coil frequency (10 kHz), coil power (220 kW), heating time (0.5 seconds) on temperature distribution (a) 4.54 mm (b) 16 mm (c) 24 mm.

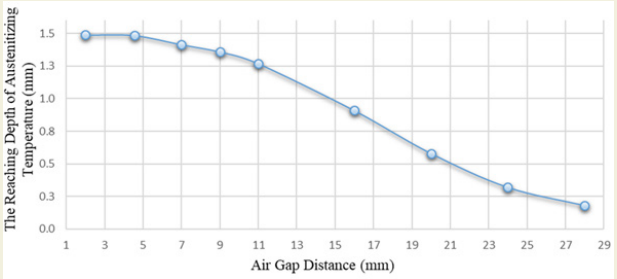

Figure 9. At fixed heating time, coil power and coil frequency, the variation of the temperature of the austenitizing temperature (800 °C) by the air gap.

In this study, the induction heating process for the AISI 4340 steel gear workpiece was studied using ELTA software. During the induction and heating process, the temperature distribution on the AISI 4340 steel gear was determined, depending on the frequency change (medium frequency: 8 – 12 kHz) and the air gap variations (2 mm – 28 mm), using constant time (0.5 seconds), and constant coil power (220 kW). In the case of constant time, constant power, and constant air gap (4.54 mm), the increase of the frequency from 8 kHz to 12 kHz has led to increased temperature in the root region of the steel gear. This, consequently, end up with the austenitizing temperature (800 ^{0}C) in deeper regions of the workpiece. On fixed time, constant power, and constant frequency (10 kHz), depending on the decrease in magnetic field effect, increasing the air gap from 2 mm to 28 mm led to reduced temperature in the root area (<800 ^{0}C).

In induction heating, it is very important to achieve an induced temperature at a certain depth. Thus, workpiece

wear resistance and fatigue resistance can be improved by using further heat treatment. To achieve this goal, induction heat treatment parameters were determined for a specific gear geometry using ELTA software. When the induction coil geometry has a section area of 6.5 x 30 mm, the coil frequency is 10 kHz, and the 4-5 mm of distance between the workpiece and coil the simulation outcome is formation of martensite at a depth of 1.48 mm in the root area of gear workpiece. In induction heating common process, medium frequency (MF) which is a generally a couple of kHz, is used in this study. As one of the outcomes of the study, it is observed that when the coil frequency was 8 kHz, the hardening depth of the gear in the root area was 0.35 mm, and when the coil frequency was 12 kHz the depth of hardening in the root area was 2.75 mm.

The outcomes obtained from this study can be compared with references and experimental studies for validation purpose. In this study, the induction heating process for AISI 4340 steel gear workpiece was investigated using ELTA software and the temperature distribution and hardness formation were compared with the work of Barka et al. [25] with COMSOL software.

The temperature distribution obtained by Barka et al. [25] using COMSOL software is given in Figure 10. When the temperatures in the tooth tip and tooth root regions were compared, it was observed that the current work and the work of Barka et al [25] have a good agreement (Figure 10). In addition, in Figure 10, the austenitization temperature (Ac3 temperature) is shown at a depth of 1.48 mm (turquoise line) with the ELTA software. This means that in the cooling process after the induction heating process, the martensite phase, which provides hardness increase and fatigue resistance, can be formed up to a depth of 1.48 mm in the root region of the gear.

The temperature distributions obtained for the 4340 steel gear workpiece with the use of ELTA and COMSOL software help us understand in which regions the martensite phase occurs after the cooling process and thus to determine the hardness profile. The austenitization temperature (Ac3, 800°C) of the AISI 4340 steel material was used to obtain the hardness profile. In the temperature distribution obtained using ELTA software in Figure 11, the region within the turquoise border shows the region where the temperature is 800°C and above. After this temperature distribution is achieved, martensite phase formation will occur in this region in 4340 steel workpieces with the quenching process. In the temperature distribution obtained by using COMSOL software in Figure 11, the gray region shows the region where the temperature is 800°C and above. Similarly, in the cooling process from this region, the entire gray region will turn into martensite phase. Therefore, by choosing the appropriate induction and coil parameters, determining the temperature profile for a steel gear workpiece, and determining the regions where the martensite phase occurs accordingly will help us obtain the desired results in terms of wear and fatigue resistance.

The air gap is another practically important variable. In the study, as the air gap is increased, the temperature in the gear root area decreased and it is interpreted that it did not cause the desired hardness change. In this study, ELTA 7.0 is used for the analysis of induction heating process of an AISI 4340-steel gear workpiece. Using ELTA software, one could rapidly perform induction heating simulation. Gears made of AISI 4340 steel are critical

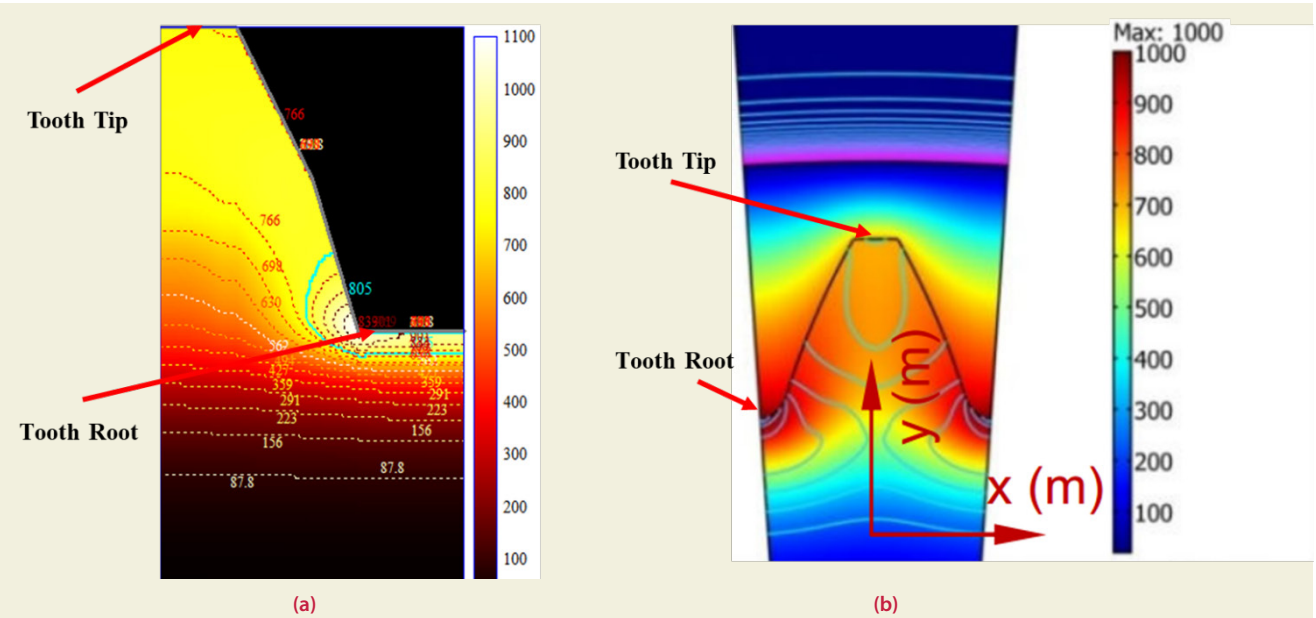

Figure 10. Temperature distributions obtained on 4340 steel gear workpieces using ELTA software and COMSOL software (coil power 220 kW, toot tip region to coil distance 4.54 mm, coil frequency 10 kHz and induction heating time 0.5 seconds) (a) ELTA 7.0© (b) COMSOL-reference study [25]

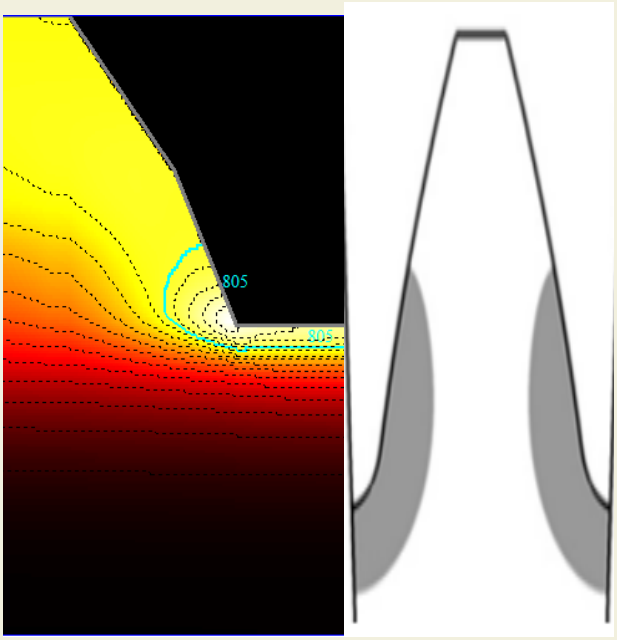

Figure 11. Hardness profile extracted from temperature distributions obtained on 4340 steel gear workpieces using ELTA software and the reference study with COMSOL software (coil power 220 kW, toot tip region to coil distance 4.54 mm, coil frequency 10 kHz and induction heating time 0.5 seconds) (a) ELTA 7.0© (zone within turquoise border) (b) COMSOL-reference study (grey zone) [25]

parts for aerospace industry. For this reason, enhancement of mechanical properties of this workpiece from workpiece is particularly important for the related industries. Since these critical components are operating under high torque and force loads along with contact with other moving parts, the fatigue, toughness, and hardness properties are the key features to be improved for operational performance of these critical components. The lifetime of these parts is strongly dependent to the heat treatment processes they undergo before the launch of the product. Consequently, the heat treatment processes must be proper and precise to be able to improve the mechanical properties of these critical components. Using numerical methods in this study, we make sure that the key parameters for induction hardening process are precisely determined for a better outcome. In the future studies related to this field, high frequency effect (100-200 kHz), coil geometry effect, and the effect of cooling water can be studied. In addition, the application of two consecutive frequencies (medium-frequency and high frequency) can be examined with magnetic flux concentrator.

Acknowledgments

The authors would like to thank to V. Bukanin and A.N. Ivanov for valuable discussions, remarks, and academic trial version of ELTA software from NSGSOFT.

Declaration of Competing Interest

The authors declare that they have no known competing financial interests or personal relationships that could have appeared to influence the work reported in this paper.

Rererences

[1] Bukanin, V. A., Ivanov, A. N., Zenkov, A. E., Vologdin, V. V., & Vologdin Jr, V. V. 2018. Induction Hardening of External Gear. Management Science and Engineering, 327(2), 022016. https://doi.org/10.1088/1757-899X/327/2/022016

[2] Dawson, F. P., & Jain, P. 1990. Systems for induction heating and melting applications: a comparison of load commutated inverter. In 21st Annual IEEE Conference on Power Electronics Specialists (pp. 281-290). IEEE.

[3] Magnabosco, I., Ferro, P., Tiziani, A., & Bonollo, F. 2006. Induction heat treatment of an ISO C45 steel bar: Experimental and numerical analysis. Computational materials science, 35(2), 98-106. https://doi.org/10.1016/j.commatsci.2005.03.010

[4] Jomaa, W., Songmene, V., & Bocher, P. 2013. On residual stress changes after orthogonal machining of induction hardened AISI 4340 steel. In Proceedings of Materials Science and Technology Conference and Exhibition, MS&T, 13, 94-103.

[5] Lucia, O., Acero, J., Carretero, C., & Burdio, J. M. 2013. Induction heating appliances: Toward more flexible cooking surfaces. IEEE Industrial Electronics Magazine, 7(3), 35-47.

[6] Jankowski, T. A., Pawley, N. H., Gonzales, L. M., Ross, C. A., & Jurney, J. D. 2016. Approximate analytical solution for induction heating of solid cylinders. Applied Mathematical Modelling, 40(4), 2770-2782. https://doi.org/10.1016/j.apm.2015.10.006

[7] Tavakoli, M. H., Ojaghi, A., Mohammadi-Manesh, E., & Mansour, M. 2009. Influence of coil geometry on the induction heating process in crystal growth systems. Journal of crystal growth, 311(6), 1594-1599. https://doi.org/10.1016/j.jcrysgro.2009.01.092

[8] Chaboudez, C., Clain, S., Glardon, R., Rappaz, J., Swierkosz, M., & Touzani, R. 1994. Numerical modelling of induction heating of long workpieces. IEEE transactions on magnetics, 30(6), 5028-5037.

[9] Fu, X., Wang, B., Tang, X., Ji, H., & Zhu, X. 2017. Study on induction heating of workpiece before gear rolling process with different coil structures. Applied Thermal Engineering, 114, 1-9. https://doi.org/10.1016/j.applthermaleng.2016.11.192

[10] Baldan, M., Cetin, M., Nikanorov, A., & Nacke, B. 2019. Optimal Design of Magnetic Flux Concentrators in Induction Heating. In 2019 XXI International Conference Complex Systems: Control and Modeling Problems (CSCMP) (pp. 203-207). IEEE.

[11] Bukanin, V., Ivanov, A., & Zenkov, A. 2019. Investigation of heating and melting in ELTA programs. COMPEL-The international journal for computation and mathematics in electrical and electronic engineering.

[12] Bukanin, V. A., Zenkov, A. E., & Ivanov, A. N. 2017. Simulation of single and dual-frequency induction hardening of steel gear using ELTA. In 2017 IEEE Conference of Russian Young Researchers in Electrical and Electronic Engineering (EIConRus) (pp. 791-795). IEEE.

[13] M. Fisk. 2011. Simulation of induction heating in manufacturing. International Journal for Computational Methods in Engineering Science and Mechanics,12,161-167.

[14] Chen, H. C., & Huang, K. H. 2008. Finite element analysis of coupled electromagnetic and thermal fields within a practical induction heating cooker. International Journal of Applied Electromagnetics and Mechanics, 28(4), 413-427.

[15] Candeo, A., Ducassy, C., Bocher, P., & Dughiero, F. (2011). Multiphysics modeling of induction hardening of ring gears for the aerospace industry. IEEE Transactions on Magnetics, 47(5), 918-921.

[16] Frogner, K., Andersson, M., Cedell, T., Siesing, L., Jeppsson, P., & Ståhl, J. 2011. Industrial heating using energy efficient induction technology. In Proc. Int. Conf. Manuf. Syst. (pp. 1-6).

[17] Hadhri, M., El Ouafi, A., & Barka, N. 2017. Prediction of the hardness profile of an AISI 4340 steel cylinder heat-treated by laser-3D and artificial neural networks modelling and experimental validation. Journal of Mechanical Science and Technology, 31(2), 615-623.

[18] Pape, J. A., & Neu, R. W. 2007. A comparative study of the fretting fatigue behavior of 4340 steel and PH 13-8 Mo stainless steel. International journal of fatigue, 29(12), 2219-2229.

[19] Maamri, I., El Ouafi, A., & [2], N. 2014. Prediction of 4340 steel hardness profile heat-treated by laser using artificial neural networks and multi regression approaches. International Journal of Engineering and Innovative Technology, 4(6), 14-22.

[20] Bilal, M. M., Yaqoob, K., Zahid, M. H., Tanveer, W. H., Wadood, A., & Ahmed, B. 2019. Effect of austempering conditions on the microstructure and mechanical properties of AISI 4340 and AISI 4140 steels. Journal of Materials Research and Technology, 8(6), 5194-5200.

[21] Barka, N., Bocher, P., Chebak, A., Brousseau, J., & Ramdenee, D. S. (2011). Study of Currents and Temperature of Induced Spur Gear using 2d Simulation. International Journal of Mechanical and Mechatronics Engineering, 5(11), 2483-2488.

[22] Di Barba, P., Forzan, M., & Sieni, E. (2015). Multiobjective design optimization of an induction heating device: A benchmark problem. International Journal of Applied Electromagnetics and Mechanics, 47(4), 1003-1013.

[23] Smalcerz, A. (2015). The use of multifrequency induction heating for temperature distribution control. Archives of metallurgy and materials, 60.

[24] Chebak A., Barka N., Menou A., Brousseau J.and Ramdenee D., (2011). Simulation and validation of spur gear heated by induction using 3D multi-physics model. World Academy of Science, Engineering and Technology,Vol. 59, 893-897.

[25] Barka, N., (2017). Study of the machine parameters effects on the case depths of 4340 spur gear heated by induction—2D model. The International Journal of Advanced Manufacturing Technology, 93(1-4), 1173-1181.

EUROPEAN MECHANICAL SCIENCE
e-ISSN: 2587-1110

RESEARCH ARTICLE

Assessing household damages using multi-model deep learning pipeline

Fatih Kıyıkçı[1], H. Onur Cunedioğlu[1], Enes Koşar[1], M. Eren Bekin[1], Fatih Abut[2*], M. Fatih Akay[2]

[1]Anadolu Sigorta, Istanbul, Turkey.
[2]Çukurova University, Department of Computer Engineering, Adana, Turkey

Orcid: F. Kıyıkçı (0000-0003-3949-5680), H.O. Cunedioğlu (0000-0002-4782-1768), E. Koşar (0000-0001-9757-2483), M.E. Bekin (0000-0002-9024-250X), F. Abut (0000-0001-5876-4116), M.F. Akay (0000-0003-0780-0679)

Abstract: Since the beginning of the pandemic, the home insurance sector has suffered from various difficulties. One of the most important difficulties was assessing the damages in the insurance owners' homes. Due to the current pandemic, letting the experts assess the damages in place is a life-threatening risk. Therefore, the idea of automatically assessing the damage is born. This study aims to create a full report for home damages using Convolutional Neural Network (CNN) and various large deep learning architectures such as EfficientNet, ResNet, U-Net, or Feature Pyramid Network (FPN). Multiple models for tasks such as binary classification and instance segmentation were developed to create an end-to-end reporting pipeline. In more detail, the pipeline consists of two binary classification models and a segmentation model. Binary classification models are responsible for detecting if the picture is indoors and if there is a wall in the picture, whereas the instance segmentation model is responsible for segmenting the damaged parts of the wall class. The effectiveness of the pipeline was measured using different metrics for each task, including accuracy, F1, Intersection over Union (IoU), and Dice scores. The data for each task is labeled by hand and fed to models. The results show that the constructed pipeline can successfully classify and segment the given images according to the needs of our project. The project will affect the home insurance assessment procedure and time spent tremendously by automatizing these repetitive processes.

Keywords: Deep learning, convolutional neural networks, semantic segmentation, classification.

1. Introduction

Since the beginning of the pandemic, people tend to make less contact with strangers or even with relatives as they should be. However, in particular areas of the natural flow of life, getting in touch with somebody is inevitable, i.e., during shopping, working, and public transporting. The pandemic has changed the way people live drastically. During this era, people are witnessing how the most deep-seated habits, traditions, and the way people behave are transforming at a killing pace [1].

With the advanced computer technologies and the pandemic force, contactless applications are trending as never been before, and it seems that they will still be the hot topic for a while [2-4]. Before the pandemic, all these applications were in the "Nice-To-Have" category, but now, they have settled in the "Must-Have" shelf robustly. Considering these new pandemic normals, the "Household Damage Assessing" project has been implemented to automate these cumbersome processes.

Several studies have been conducted in the literature to assess household damages using different methods. For example, Perez et al. [5] used close-up images to classify the defect in the building based on VGG-16. The study predicts the defect and localizes the possible defect using Class Activation Mapping (CAM). Yu et al. [6] proposed a novel method based on deep convolutional neural networks to identify and localize damages of building structures equipped with smart control devices. Li et al. [7] designed a platform to automatically estimate home damage levels in disaster areas through crowdsourcing ideas and CNN approaches. Feng et al. [8] developed a highly accurate structural damage detection method using a deep convolutional neural network with transfer learning. Naito et al. [9] proposed a method for detecting damaged buildings in the event of an earthquake using machine learning models and aerial photographs. These previous solutions, techniques, or discussions do not offer an industry-level solution. Instead, the topic has been covered by an academic view, and the images studied are not from real-world data, i.e., not shot on mobile phones or taken

*Corresponding author.
Email: fabut@cu.edu.tr

European Mechanical Science (2022), 6(2): 138-142
https://doi.org/10.26701/ems.1031595
Received: December 5, 2021 — Accepted: March 1, 2022

by building surveyors.

This study aims to create a full report for home damages using CNN and various large deep learning model architectures such as EfficientNet, ResNet, U-Net, or Feature Pyramid Network (FPN). Mainly, the contributions of this study can be summarized as follows:

- We created the input data based on 3.700 labeled ground truth images retrieved from Anadolu Sigorta's own database. Those images are only from house damage claims.
- Multiple models for binary classification and instance segmentation were developed to create an end-to-end reporting pipeline. The pipeline consists of two binary classifiers and a segmentation model in more detail. Binary classifiers are responsible for detecting if the picture is indoors and if there is a wall in the picture. In contrast, the instance segmentation model is responsible for segmenting the damaged parts of the wall class.
- The performance of the classification models has been evaluated by calculating the confusion matrix and the accuracy, F1, Intersection over Union (IoU), and Dice scores.

The rest of the paper is structured as follows. Section 2 gives information about the dataset and methodology. Section 3 presents the results and discussion. Section 4 concludes the paper along with possible research directions.

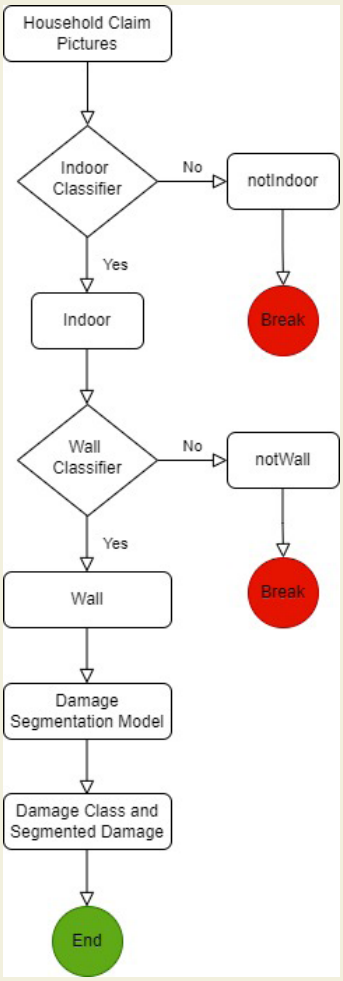

Figure 1. Flowchart of the home damage assessment pipeline

2. Dataset and Methodology

The model pipeline, illustrated in Figure 1, is constructed by three different deep learning models connected with their image inputs and filtered outputs in an end-to-end fashion.

The input pictures from a home insurance claim are first fed to a binary classifier which classifies the picture as indoor or notIndoor. Then, if an indoor image is detected, another binary classifier classifies the image as wall or notWall. Finally, suppose an image of a wall is detected. In that case, it is fed to the damage segmentation model, which segments the damages that are present in the image with respect to their damage class and produces output mask images.

The utilized input data consists of images retrieved from Anadolu Sigorta's own database and are only from house damage claims. Figure 2 shows some samples from each pipeline class. The data can be tagged in a wide variety of semantic classes. We have used and labeled the data in three different semantic meanings for their respective objectives: indoor-outdoor classification, wall-not wall classification, and semantic segmentation of wall damages with four different classes of wall damages: crack, water stain, paint peeling, and shatter. We used 1.425 labeled

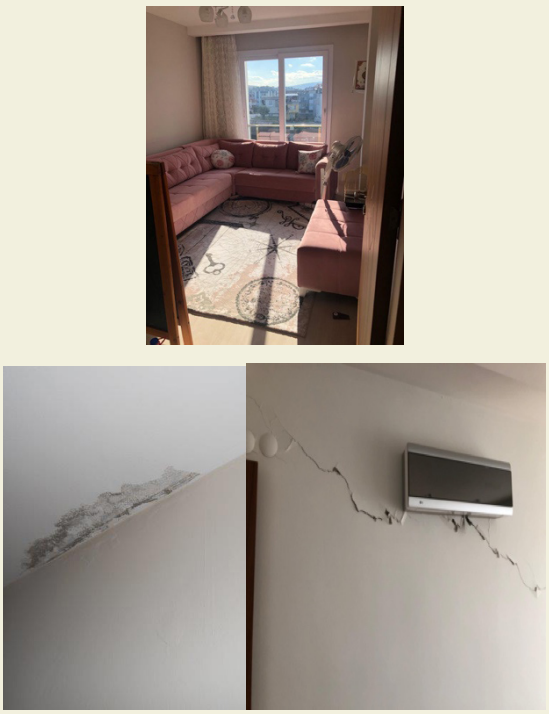

Figure 2. Samples from each pipeline class (indoor, wall, and crack)

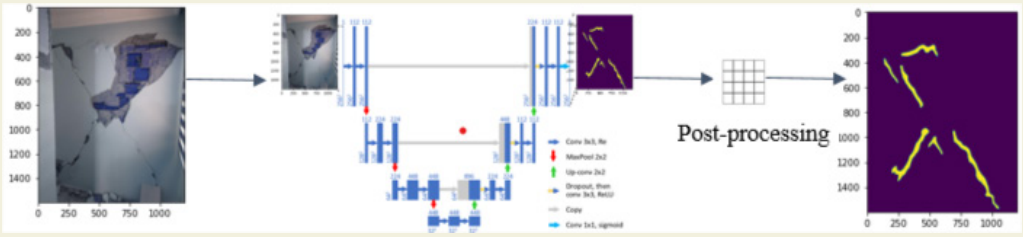

Figure 3. Visualization of segmentation process of a random sample using U-Net model architecture

images for each classification task and 2.374 labeled images for the segmentation task.

For all objectives, we have used a variety of pre-processing methods which go hand in hand with both the objective and used modeling methods, such as image augmentation (i.e., flip, blur, or saturation), resizing, or normalizing the images. All images in all objectives have been resized to a 384x384 resolution to standardize the image resolutions as input to the deep learning model, reducing the training time and required VRAM.

For classification objectives, we haven't used any pre-processing methods other than resizing and normalizing. For the segmentation task, we have used Gaussian blurring and random brightness contrast augmentation function from the "Albumentations" [10] library in Python, with the probability of application p=0.3 and a custom random box-blurring augmentation, which blurs a small box-shaped portion of the image with the probability of application p=0.7.

Several metrics have been proposed in the literature to evaluate the performance of binary classification and segmentation models. We summarize the most popular metrics for assessing the accuracy of classification and segmentation models.

- **Accuracy / F1-score** can be defined for a bi-class problem or for each class in the case of multiclass as follows (TP, TN, FP, and FN refer to the true positives, true negatives, false positives, and false negatives, respectively):

$$Accuracy = \frac{TP + TN}{TP + FP + FN + TN} \#(1)$$

$$F1 - score = \frac{2 * TP}{2 * TP + FP + FN} \#(2)$$

- **Intersection over Union (IoU)**: IoU is defined as the area of intersection between the predicted segmentation map A and the ground truth map B, divided by the area of the union between the two maps:

$$IoU = \frac{|A \cap B|}{|A \cup B|} = \frac{TP}{TP + FP + FN} \#(3)$$

- **Dice:** Dice coefficient is a popular metric for image segmentation, which can be defined as twice the overlap area of predicted and ground-truth maps, divided by the total number of pixels in both images.

$$Dice = \frac{|A \cap B|}{|A| + |B|} = \frac{2 * TP}{2 * TP + FP + FN} \#(4)$$

We used CNN along with various large deep learning model architectures. CNN has become hugely popular because of its architecture which automatically performs feature extraction for image classification. CNN uses two operations called 'convolution' and 'pooling' to reduce an image into its essential features and uses those features to understand and classify the image.

We experimented with a wide range of combinations for training the deep learning models for each of their respective tasks and evaluated each experiment using the evaluation metrics defined in Section 2.3. We used the PyTorch [11] library in Python for experimenting and constructing deep learning models. We utilized the transfer learning method, which transfers weights of models trained on large datasets, such as ImageNet, to a new model that we train on our specific objective and data. We used pre-trained models from timm [12] and SMP [13] packages for classification and segmentation, respectively. Furthermore, we used CrossEntropyLoss from the torch library as the main loss function since the data is not in an imbalanced state.

For the segmentation task, we have experimented with a large family of deep learning model architectures such as EfficientNet [14] or ResNet [15] overall objectives. After that, as illustrated in Figure 3, we also experimented with U-Net [16] and FPN [17] architectures for the segmentation task, using the SMP library, which serves segmentation models that are using pre-trained EfficientNet or ResNet architecture weights. Figure 4 represents some damage segmentation model outputs overlaid on predicted images.

Also, we constructed a custom learning rate scheduler dependent on the number of epochs and Adam optimization function from the torch library. We used 20% of the training dataset as validation and used two different test datasets. After the training phase, we applied different post-processing methods to the output for stabilizing the predictions and reducing the number of errors.

We used thresholding to reduce the number of incorrect-

ly predicted pixels while keeping the number of correctly predicted pixels roughly the same. Thus, we have selected different thresholds and experimented with optimizing the evaluation metrics. We have found that the value 0.2 was the optimal threshold value for all four classes.

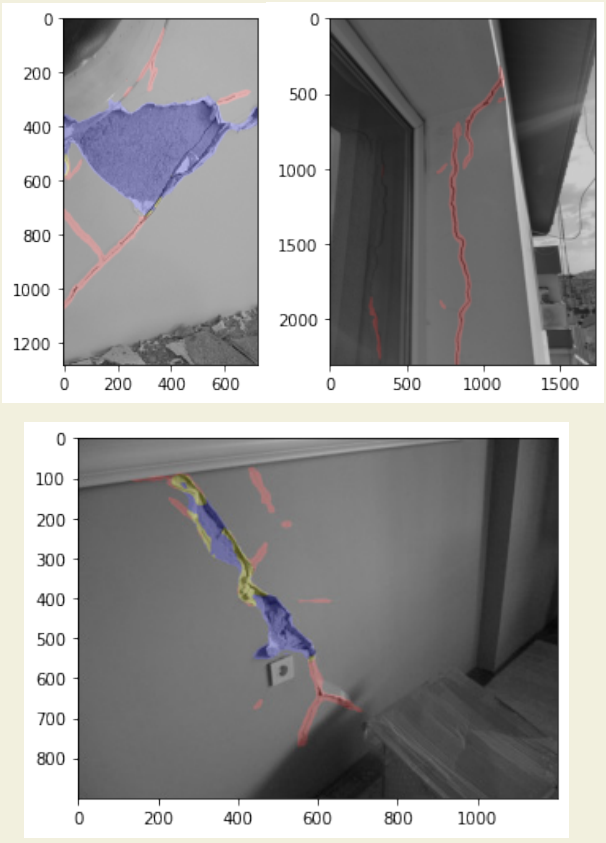

Figure 4. Damage segmentation model outputs overlaid on predicted images

To reduce the number of false positives (i.e., ground truth has no damage, the prediction has little damage), we have used a min_pixel_ratio value, which returns an empty mask if the predicted number of pixels over total pixels in the image is not greater than the min_pixel_ratio. This approach prevents the output of 1 pixel for an empty mask, resulting in a score of 0. According to our experiments, this value is optimal at 2%.

3. Results and Discussion

Table 1 and Table 2 show the experiment and confusion matrix results for binary indoor classification models, respectively. Similarly, Table 3 and Table 4 show the experiment and confusion matrix results for binary wall classification models, respectively.

The best indoor/notIndoor model in our experiments has achieved an accuracy of 0.885 and an F1-score of 0.878, considering that the dataset is created using real-life claims data and has many uninformative images. In this case, the model has encountered only 41 errors from 357 images, although only 855 images have been used for training (excluding validation).

Wall classification and indoor classification are very similar problems in terms of their technical objective and complexity. The best wall classifier, which was close to the performance exhibited by the indoor classifier, yielded an accuracy of 0.879 and an F1-score of 0.877 and had 43 errors in 357 photographs by using 855 images for training.

Table 1. Experiment results for binary indoor classification models

Backbone name	Accuracy	F1-score
EfficientNet_B0	0.874	0.862
EfficientNet_B1	0.885	0.878
EfficientNet_B2	0.868	0.860
ResNet18	0.865	0.852
ResNet50	0.865	0.848

Table 2. Confusion matrix results of predictions from EfficientNet-B1 model for indoor classification

	notIndoor	Indoor
notIndoor	114	20
Indoor	21	201

Table 3. Experiment results for binary wall classification models

Backbone name	Accuracy	F1-score
EfficientNet_B0	0.860	0.857
EfficientNet_B1	0.871	0.869
EfficientNet_B2	0.879	0.877
ResNet18	0.831	0.830
ResNet50	0.750	0.750

Table 4. Confusion matrix results of predictions from EfficientNet-B2 model for wall classification

	notWall	Wall
notWall	179	25
Wall	18	134

The segmentation models were trained using 1.401 images and tested using 973 images in two test sets. Table 5 shows the experiment results of models on both test sets (averaged per sample). The best damage segmentation model is an FPN architecture model using an EfficientNet-B2 as a backbone, which has reached a Dice score of 0.647 and an IoU score of 0.576.

Table 5. Experiment results for the damage segmentation models

Backbone name	Architecture	Dice Score	IoU Score
EfficientNet_B0	FPN	0.644	0.573
EfficientNet_B1	FPN	0.641	0.570
EfficientNet_B2	FPN	0.647	0.576
EfficientNet_B0	U-Net	0.632	0.560
EfficientNet_B1	U-Net	0.634	0.562
EfficientNet_B2	U-Net	0.636	0.565

4. Conclusion and Future Work

This study proposed models for automatically assessing household damages using multi-model deep learning. In more detail, two binary classification models and a segmentation model have been developed based on a dataset created from the database of Anadolu Sigorta. Binary classification models are responsible for detecting if the picture is indoors and if there is a wall in the picture. In contrast, the instance segmentation model is responsible for segmenting the damaged parts of the wall class. Experiments have been made using transfer learning with different backbone architectures and pre-trained weights. A pipeline solution with three steps has been implemented for the project requirements. For all tasks, several experiments have been conducted with different model architectures and backbones. At the final state, the pipeline consists of one EfficientNet-B1 indoor classification model, one EfficientNet-B2 wall classification model, and one FPN damage segmentation model with EfficientNet-B2 backbone.

Despite having a limited dataset, the model pipeline achieved relatively good scores and stable results on all three objectives. We believe that with time, as we label more images in an accurate and standardized fashion, the results will get better. In future work, we plan to expand the limits of the damage detection pipeline to not only detect and segment the wall damages but also do the same for tile and parquet damages and predict their dimensions while creating a detailed report of damage for the claim. Other possible future research direction includes automatically categorizing and assessing automobile damages from road traffic accidents.

5. References

[1] Di Crosta, A., Ceccato, I., Marchetti, D., La Malva, P., Maiella, R., Cannito, L., Di Domenico, A. (2021). Psychological factors and consumer behavior during the COVID-19 pandemic". PloS one, 16(8), e0256095.

[2] Puriwat, W., Tripopsakul, S. (2021). Explaining an adoption and continuance intention to use contactless payment technologies: during the COVID 19 pandemic. Emerging Science Journal, 5(1): 85-95.

[3] Al Tarabsheh, A., Yaghi, M., Younis, A., Sarker, R., Moussa, S., Eldigair, Y., Hajjdiab, H., El-Baz, A., Ghazal, M. (2021). Towards Contactless Learning Activities during Pandemics Using Autonomous Service Robots. Applied Sciences, 11, 10449.

[4] Li, X., Yuen, K. F., Wang, X., Wong, Y. D. (2021). Contactless technologies adoption during the coronavirus pandemic: a combined technology acceptance and health belief perspective. Technology Analysis & Strategic Management. doi: 10.1080/09537325.-2021.1988919.

[5] Perez, H., Tah, J. H., Mosavi, A. (2019). Deep learning for detecting building defects using convolutional neural networks. Sensors, 9(16), 3556.

[6] Yu, Y., Wang, C., Gu, X., Li, J. (2019). A novel deep learning-based method for damage identification of smart building structures. Structural Health Monitoring, 18(1): 143-163.

[7] Li, Z., Tian, K., Wang, F., Zheng, X., Wang, F. (2016). Home damage estimation after disasters using crowdsourcing ideas and Convolutional Neural Networks. In: 2016 5th International Conference on Measurement, Instrumentation and Automation.

[8] Feng, C., Zhang, H., Wang, S., Li, Y., Wang, H., Yan, F. (2019). Structural damage detection using deep convolutional neural network and transfer learning. KSCE Journal of Civil Engineering, 23(10): 4493-4502.

[9] Naito, S., Tomozawa, H., Mori, Y., Nagata, T., Monma, N., Nakamura, H., Shoji, G. (2020). Building-damage detection method based on machine learning utilizing aerial photographs of the Kumamoto earthquake. Earthquake Spectra, 36(3): 1166-1187.

[10] Buslaev, A., Iglovikov, V. I., Khvedchenya, E., Parinov, A., Druzhinin, M., Kalinin, A. A. (2020). Albumentations: fast and flexible image augmentations. Information, 11(2): 125.

[11] Paszke, A. (2019). PyTorch: An Imperative Style, High-Performance Deep Learning Library. Advances in Neural Information Processing Systems, 32: 8024-8035.

[12] Wightman, R. (2019) PyTorch Image Models. GitHub. doi:10.5281/zenodo.4414861

[13] Kingma, D. P., & Ba, J. (2014). Adam: A method for stochastic optimization. arXiv preprint arXiv:1412.6980.

[14] Tan, M., Le, Q. (2019). Efficientnet: Rethinking model scaling for convolutional neural networks. In: International Conference on Machine Learning, 6105-6114.

[15] He, K., Zhang, X., Ren, S., & Sun, J. (2016). Deep residual learning for image recognition. In: Proc. of the IEEE conference on computer vision and pattern recognition, 770-778.

[16] Ronneberger, O., Fischer, P., Brox, T. (2015). U-net: Convolutional networks for biomedical image segmentation. In: International Conference on Medical image computing and computer-assisted intervention, 234-241.

[17] Lin, T. Y., Dollár, P., Girshick, R., He, K., Hariharan, B., Belongie, S. (2017). Feature pyramid networks for object detection. In: Proc. of the IEEE conference on computer vision and pattern recognition, 2117-2125.

EUROPEAN MECHANICAL SCIENCE
e-ISSN: 2587-1110

RESEARCH ARTICLE

Finite element analysis of the seepage problem in the dam body and foundation based on the Galerkin's approach

Timuçin Alp Aslan[1*], Beytullah Temel[1]

[1]Cukurova University, Department of Civil Engineering, Adana, Turkey

Orcid: T.A.Aslan (0000-0002-7558-3568), B. Temel (0000-0002-1673-280X)

Abstract: In this study, the 2D steady-state seepage analysis of the dam body and its base is investigated using the finite element method (FEM) based on Galerkin's approach. The body and foundation soil is considered as homogeneous isotropic and anisotropic materials and the effects of horizontal drainage length and the cutoff wall on seepage are investigated. The differential equation governing the response of water in the soil is obtained with the help of Darcy's law and continuity equations. A program has been prepared in Fortran programming language to find the hydraulic load, pressure values and phreatic line pressure values at the points inside the dam body and the quantity of seepage on the bottom of dam. It has been shown that the obtained values are in good agreement by comparing them with the results of existing studies in the literature.

Keywords: Dam; Seepage analysis; Finite element methods, Phreatic line, Hydraulic head

1. Introduction

As with many engineering problems, the state and movement of water in the body and foundation ground of impounding dams need to be analyzed. Seepage; It is the uncontrolled, unmeasurable continuous movement of water accumulated in the upstream part of the dam towards the downstream part. Seepage in the bodies of the dams causes water loss from the reservoir, as well as erosion in the fill, causing piping to occur. This situation causes damage to the dam's body and may even cause the dam to collapse. For these reasons, seepage problems in the dam body and its foundation continue to be a current issue and are being investigated by many researchers. Ardıçlıoğlu [1] used the FEM for the analysis of the 2D steady-state seepage analysis of the embankment dam body and calculated the pore water pressures of the element nodes in the flow regions and the seepage rate through the unit width of the embankment. Keskin [2] studied the potential and velocity distributions of various sheet piles, spillways, and earth-fill dams in the body and bottom of the seepage in two dimensions using the FEM. Çilingir [3] investigated the seepage in the body of Büyükçekmece dam, which was chosen as a mathematical model, by using the FEM and the Geo-Studio computer program. Fakhari and Ghanbari [4] developed a new formula to find the total amount of seepage through a clay core dam body and compared it with all other flow calculation methods. Çelik [5] performed a two-dimensional seepage analysis on the Ikizdere Dam body cross-sections with the Seep/W program. In the selection of the material parameters of the model entered into the program, the laboratory test results presented in the project sheets and the literature were used. Sağlıca [6] wrote a program that performs seepage analysis with the finite difference method (FDM) and compared the values found as a result of the analysis with the results obtained by other methods. Darbandi et al. [7] developed A Moving-Mesh finite volume method (FVM) that can solve the seepage problem in arbitrary geometries. Rafiezadeh and Ataie-Ashtiani [8] improved the three-dimensional boundary element solution based on the transformation approach for the analysis of seepage in a multi-domain general anisotropic media. Ouria and Toufigh [9] used the FEM based on Nelder-Mead simple optimization and the changing mesh technique to solve the unconfined seepage problems. El-Jumaily and Al-Bakry [10] examined the seepage analysis through and underneath the hydraulic structures together without dividing the structure into parts, and then analyzed it with the FVM using rectangular elements separately for each of the parts. Mesci [11] investigated the methods used to determine the seepage occurring in the dam bodies and calculated the total seepage amounts by determining the flow of water in the dam body with these meth-

*Corresponding author.
Email: taslan@cu.edu.tr

European Mechanical Science (2022), 6(2): 143-151
https://doi.org/10.26701/ems.1024266
Received: November 16, 2021 — Accepted: March 16, 2022

ods. Çakır [12] sophisticated a numerical model for the two-dimensional groundwater flow using the collocation method. For the purpose of comparison, they prepared a MATLAB program with the FDM. Quanshu and Jianjun [13] adopted a numerical simulation method for leakage analysis and investigated the influence of core and other factors by comparing the leakage area under different conditions. Mansuri and Salmasi [14] focused on the effectiveness of using horizontal drainage and cutoff wall in reducing seepage flow from a heterogeneous earth dam. For this purpose, they investigated the effect of various horizontal drainage lengths and shear wall depths on seepage under the earth dam at different locations of the foundation. Sakhmarsi et al. [15] investigated the influence of cutoff wall depth, position, and permeability properties on seepage in the homogeneous earth-fill dams using SEEP/W computer software. Yuan and Zhong[16] used the weak-form quadrature element method for the analysis of three-dimensional unconstrained seepage problems. Zhang et al. [17] proposed a moving kriging mesh-free method with Monte Carlo integration to determine the phreatic surface while investigating the seepage analysis. Khassaf and Madhloom [18] found the quantity of seepage that occurs in soil dams with the effect of changing the core permeability and the core thickness of a core region by using the FEM SLIDE V.5.0 software. Zewdu[19], calculated the amount of the seepage occurring in the Koga earth-fill dam body and foundation using the finite element-based PLAXIS 2D software. Taghvaei et al. [20] prepared numerical modeling of earth dam in different clay-sand compositions using SEEP/W software and validated it with experimental results. In their paper, Doaa and Molla [21] aimed to determine the effect of the existence of the sheet pile as well as its height and location on the total seepage discharge and velocities through the dam's cross-section. Sanayei and Javdanian [22] developed a new analytical solution for steady seepage from dams with nonsymmetric boundary conditions. Non-symmetrical boundary conditions for two-dimensional cases were created in dams with different unit step functions in the downstream part of the dam plane. Salmasi et al. [23] used the FEM to investigate the effect of the cutoff wall and downstream filters on seepage events occurring at the dam foundation and verified the experimental data with numerical modeling. Kheiri et al. [24] calculated the seepage under clay core embankment dams using the finite element based SEEP/W program and demonstrated the accuracy of their results by comparing them with the physical modeling results.

Preventing seepage in dam bodies is very difficult and requires great economic costs. For these reasons, it is important to calculate the amount of seepage that will occur by carrying out detailed research and studies during the design phase before the dam construction starts. In this study, the 2D steady-state seepage analysis of the embankment dam body and its base will be examined by the FEM. As it is known, the FEM is a numerical method used in the solution of engineering problems, especially in recent years, due to its many advantages [25-29]. The main purpose of this paper is to demonstrate the effective and easy usability of the FEM based on Galerkin's element approach in seepage problems in isotropic and anisotropic soil mediums. For the suggested models, a computer program is coded in Fortran for the steady-state seepage analysis. With the aid of the written program, different types of seepage problems can be solved efficiently and accurately.

2. MATHEMATICAL FORMULATIONS

2D steady-state seepage in a permeable, anisotropic soil (Figure 1) is expressed by the following partial differential equation with the help of Darcy's law and continuity equations [30].

$$K_x \frac{\partial^2 h}{\partial x^2} + K_y \frac{\partial^2 h}{\partial y^2} = 0 \quad (1)$$

where, K_x and K_y are the coefficients of hydraulic conductivity in the x and y direction, h is the total hydraulic head.

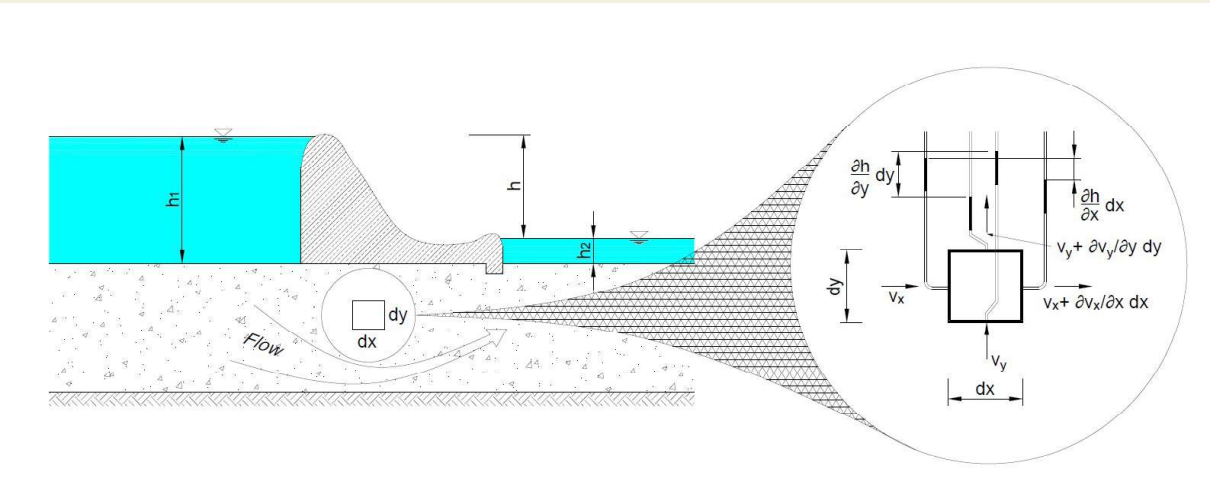

Figure 1. Flow of water through saturated pervious soil beneath a hydraulic structure

It is the sum of the elevation head and the pressure head as stated in the eq. (1). The velocity head is ignored due to the very slow movement of the water in the ground.

$$h = z + \frac{p}{\gamma_w} \tag{2}$$

The partial differential form of eq. (1) is written in integral form by applying the weighted residuals method as follows:

$$\int\int_{Ae} \psi \left(K_x \frac{\partial^2 h}{\partial x^2} + K_y \frac{\partial^2 h}{\partial y^2} \right) dA = 0 \tag{3}$$

Eq. (4) is obtained by the application of the partial integration to eq. (3).

$$\int\int_{Ae} \left(K_x \frac{\partial \psi}{\partial x}\left(\frac{\partial h}{\partial x}\right) + K_y \frac{\partial \psi}{\partial y}\left(\frac{\partial h}{\partial y}\right) \right) dxdy - \int_{\Gamma} \psi \left(\frac{\partial h}{\partial x} n_x + \frac{\partial h}{\partial y} n_y \right) d\sigma = 0 \tag{4}$$

In these expressions, the second part represents the boundary conditions, Γ represents the boundary of the element, n_x and n_y are components of the unit vector, q is the inflow or the outflow of the unit boundary surface and σ is the integration variable along the boundary in the counterclockwise direction.

In the Galerkin method, the variation of the hydraulic load is taken into account as weight functions.

$$\psi = \delta h \tag{5}$$

Equation (6) is obtained by substituting the weight functions in eq. (4).

$$\int\int_{Ae} \left(K_x \frac{\partial(\delta h)}{\partial x}\left(\frac{\partial h}{\partial x}\right) + K_y \frac{\partial(\delta h)}{\partial y}\left(\frac{\partial h}{\partial y}\right) \right) dxdy - \int_{\Gamma} (\delta h) q d\sigma = 0 \tag{6}$$

FEM is one of the effective numerical methods. This approach divides the problem domain into several elements with limited sizes and gives approximate solutions for the nodes of the system. In this study, an isoparametric 8-noded serendipity element is used in the formulation. The hydraulic heads at any point of the element are given in eq. (7).

$$\{h\} = [N_1\ N_2\ N_3\ N_4\ N_5\ N_6\ N_7\ N_8] \begin{Bmatrix} h_1 \\ h_2 \\ h_3 \\ h_4 \\ h_5 \\ h_6 \\ h_7 \\ h_8 \end{Bmatrix} = [N]\{\Delta\} \tag{7}$$

where is $[N]$ the matrix of shape functions and $\{\Delta\}$ is the element hydraulic heads. The coordinates of any point in the quadratic element are given below depending on the shape functions.

$$x = \sum_{i=1}^{8} N_i x_i \qquad y = \sum_{i=1}^{8} N_i y_i \tag{8}$$

where x_i and y_i are the coordinates of a node. For isoparametric elements, the geometric shape functions and interpolation shape functions are the same. The hydraulic head at any point of the element can be calculated with the help of element node loads depending on the shape functions.

$$h(\xi,\eta) = \sum_{i=1}^{8} N_i(\xi,\eta)\ h_i \tag{9}$$

Substituting Eq. (7) into Eq. (6) gives the following equation

$$\int\int_{Ae} \left(\frac{\partial(\delta h)}{\partial x} K_x \left(\frac{\partial [N]\{\Delta\}}{\partial x} \right) + \frac{\partial(\delta h)}{\partial y} K_y \left(\frac{\partial [N]\{\Delta\}}{\partial y} \right) \right) dxdy - \int_{\Gamma} (\delta h)\ q\ d\sigma = 0 \tag{10}$$

Eq. (10) is based on the hydraulic head gradient vector and can be given as follows:

$$\{gv\} = \begin{Bmatrix} \frac{\partial h}{\partial x} \\ \frac{\partial h}{\partial y} \end{Bmatrix} = \begin{bmatrix} \frac{\partial [N]}{\partial x} \\ \frac{\partial [N]}{\partial y} \end{bmatrix} \{\Delta\} = [B]\{\Delta\} \tag{11}$$

Accordingly, the hydraulic head variations are expressed as follows.

$$\delta h = [N]\{\delta\Delta\}$$
$$\delta h^T = \{\delta\Delta\}^T [N]^T \tag{12}$$

Substituting of eqs. (11-12) into eq. (10) leads to,

$$\int\int_{Ae} \left(\frac{\partial [N]\{\delta\Delta\}}{\partial x} K_x \left(\frac{\partial [N]\{\Delta\}}{\partial x} \right) + \frac{\partial [N]\{\delta\Delta\}}{\partial y} K_y \left(\frac{\partial [N]\{\Delta\}}{\partial y} \right) \right) dxdy - \int_{\Gamma} [N]\{\delta\Delta\}\ q\ d\sigma = 0 \tag{13}$$

The simplified form of eq. (13) is given as:

$$\{\delta\Delta\}^T \left(\int\int_{Ae} \left(([B]^T [K][B]) dA \{\Delta\} \right) \right) - \int_{\Gamma} [N]^T q\ d\sigma = 0 \tag{14}$$

where $[K]$ is the conductivity matrix.

$$[K] = \begin{bmatrix} K_x & 0 \\ 0 & K_y \end{bmatrix} \tag{15}$$

The element stiffness matrix, $[s_e]$, and the element applied flux vector , $\{f_s\}$, are:

$$[s_e]_{(8*8)} = \int_{Ae}\int \left([B]^T [K][B]\right) dA$$

$$, \quad \{f_s\}_{(8*1)} = \int_{\Gamma}\left([N]^T q\right) d\sigma \tag{16}$$

The general form of finite element equation for steady state seepage analysis is:

$$[s_e]\{\Delta\} = \{f_s\} \tag{17}$$

where $\{\Delta\}$ is element hydraulic head vector. The value of $\{f_s\}$ is 0 (zero) at the nodes that are not on the boundary. In any flow region, the global conductance matrix and system hydraulic head vector are formed by taking the contribution of the elements.

$$[S]\{\Delta\} = \{F\} \tag{18}$$

where, $[S]$ is the global conductance matrix, $\{\Delta\}$ is the system hydraulic head vector and $\{F\}$ is the system load vector for all nodes. Under the specified boundary conditions, the total hydraulic head at the nodes is found by the numerical solution. Then, hydraulic gradients, flow velocities, the quantity of seepage and pressure values can be easily calculated.

In seepage problems, boundary conditions are used to solve the main differential equation of seepage. Boundary conditions are related to initial conditions and different flow patterns of the system. The boundary conditions do not depend on time under steady-state flow conditions. In this study, upstream and downstream levels are defined as constant head boundary conditions in order to model the seepage through the considered dams. A seepage line may be formed at the downstream region of the dam. Boundary conditions for seepage problems of the embankment dam with tailwater in the downstream region are given in Figure 2.

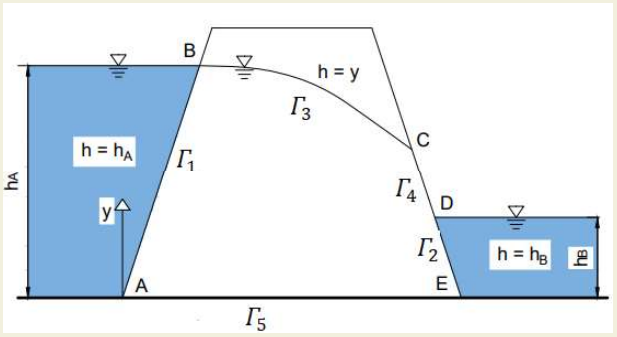

Figure 2. Seepage and boundary conditions in an embankment dam

Since the position of the phreatic surface BC in Figure 1 is not clear, it requires an iterative solution of the finite element analysis. First of all, the free surface estimated seepage line is determined, and a solution is made. After each iterative process, the free surface is updated by substituting the newly computed hydraulics heads to the old coordinates of the free surface. These processes are repeated until the error is the convergence criterion [31].

$h = h_A$ AB-Γ_1 (Upstream surface)

$h = h_B$ ED-Γ_2 (Downstream surface)

$\left\{\begin{matrix} h = y \\ \frac{\partial h}{\partial n} = 0 \end{matrix}\right\}$ BC-Γ_3 (Phreatic surface)

$h = y$ CD-Γ_4 (Seepage surface)

$\frac{\partial h}{\partial n} = 0$ AE-Γ_5 (Impervious surface)

2. Numerical Examples and Discussion

In this section, seepage analysis of dam bodies and foundations with different geometries and material properties has been studied. Element stiffness matrix and hydraulic head vector are calculated by the Gauss-Legendre numerical integral method. Several types of seepage problems are investigated with the programs written in Fortran using the FEM [32].

Example 1

Firstly, time indepented seepage phenomenon has been investigated in the homogeneous isotropic fill dam body. The material and geometrical properties are given in Figure 3.

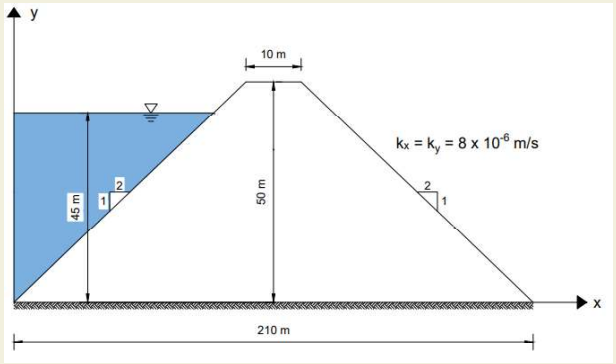

Figure 3. Geometry and material properties of the dam

The seepage value passing through the fill dam body, calculated by the FEM based on Galerkin's approach, is being compared with the results present in the literature in Table 1. It can be seen that the results are in a good agreement.

Table 1. Seepage rate per unit width of the dam ($m^3/s/m$)

Ardıçlıoğlu [1]	Flow Net Method [1]	Present Study
6.9803×10^{-5}	6.8572×10^{-5}	6.8478×10^{-5}

To perform the calculations, the seepage region is divided into 40 finite elements (149 nodes). The hydraulic head and pressure values of the embankment dam at the nodes indicated on Figure 4 are calculated and presented in Table 2.

Table 2. Hydraulic head and pressure load values of the dam

NODE	X (m)	Y (m)	HYDRAULIC HEAD (m)	PRESSURE HEAD (m)	NODE	X (m)	Y (m)	HYDRAULIC HEAD (m)	PRESSURE HEAD (m)
1	0.000	0.000	45.000	45.000	91	128.750	15.938	32.685	16.747
2	10.500	0.000	44.998	44.998	97	67.500	33.750	45.000	11.250
3	21.000	0.000	44.966	44.966	98	74.100	32.287	44.412	12.125
19	189.000	0.000	10.084	10.084	99	80.700	30.825	43.502	12.677
20	199.500	0.000	4.712	4.712	105	120.300	22.050	35.033	12.983
21	210.000	0.000	0.000	0.000	106	126.900	20.588	33.348	12.760
22	11.250	5.625	45.000	39.375	107	133.500	19.125	31.582	12.457
23	30.950	5.137	44.889	39.751	115	186.300	7.425	11.741	4.316
31	188.550	1.237	10.332	9.095	116	192.900	5.963	8.038	2.075
32	208.250	0.750	0.750	0.000	117	199.500	4.500	4.500	0.000
33	22.500	11.250	45.000	33.750	118	78.750	39.375	45.000	5.625
34	31.700	10.762	44.928	34.165	119	90.650	35.963	42.789	6.826
35	40.900	10.275	44.759	34.484	127	185.850	8.663	12.003	3.340
51	188.100	2.475	10.589	8.114	128	197.750	5.250	5.250	0.000
52	197.300	1.987	5.764	3.776	129	90.000	45.000	45.000	0.000
53	206.500	1.500	1.500	0.000	130	95.300	43.003	43.004	0.000
73	108.200	14.700	37.478	22.778	131	100.600	41.001	41.001	0.000
74	116.100	13.725	35.690	21.965	147	185.400	12.300	12.300	0.000
75	124.000	12.750	33.775	21.025	148	190.700	9.650	9.650	0.000
90	114.250	18.375	36.283	17.908	149	196.000	6.000	6.299	0.000

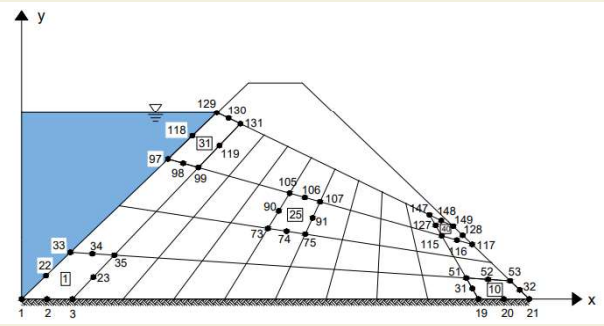

Figure 4. Finite element model of the dam

From Table 2, it can be clearly seen that the highest hydraulic head and pressure load values are in the region of the upstream part close to the foundation.

Example 2

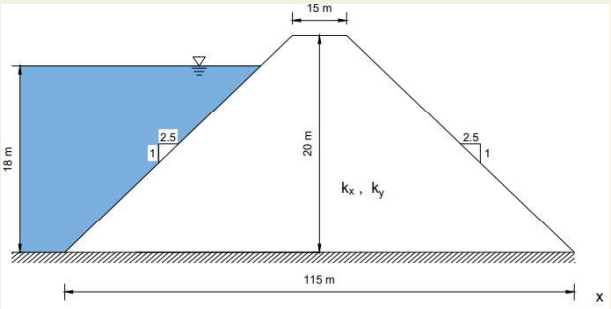

Figure 5. Geometry and material properties of the dam

The seepage quantity of dams in different situations with isotropic and anisotropic filling material properties are calculated and given in Table 3. The geometric properties of the dam are given in Figure 5.

Table 3. Seepage rate per unit width of dams with different soil properties ($m^3/s/m$)

	Permeability Coefficient (m/s)	Present Study
Case 1	$K_x = 4.5\ x\ 10^{-8}$ $K_y = 4.5\ x\ 10^{-8}$	$1.060903x\ 10^{-7}$
Case2	$K_x = 1.6\ x\ 10^{-8}$ $K_y = 4.5\ x\ 10^{-8}$	$0.3974995x\ 10^{-7}$
Case 3	$K_x = 4.5\ x\ 10^{-8}$ $K_y = 1.6\ x\ 10^{-8}$	$1.001256x\ 10^{-7}$

In Table 3, where different soil conditions are compared, it can be seen that the permeability coefficient in the x direction is more effective on seepage.

Example 3

For the embankment dam with anisotropic material (Figure 6), with horizontal drainage at the downstream part of the body, the unit width seepage rate has been calculated. The effect of the drainage length on the seepage has been investigated. The results are presented in Table 4.

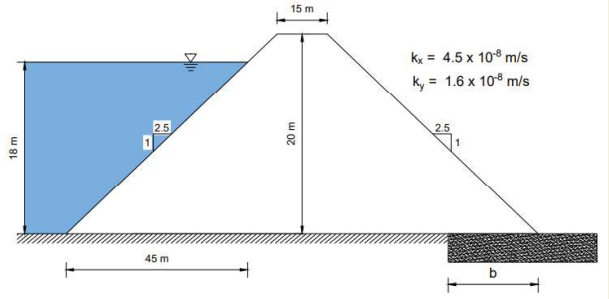

Figure 6. Geometry and material properties of the dam with horizontal drainage

Table 4. Seepage rate per unit width of dams with horizontal drainage of different lengths ($m^3/s/m$)

Horizontal Drain Length, b (m)	Sağlıca [6]	Present Study
15.5	$1.000x\ 10^{-7}$	$1.023x\ 10^{-7}$
18.0	-	$1.041x\ 10^{-7}$
21.0	-	$1.058x\ 10^{-7}$
25.0	-	$1.106x\ 10^{-7}$

Table 4 presents that the amount of seepage per unit width increases as the horizontal drainage length increases.

So that the rate of seepage increase for the length of the horizontal drains with 15.5, 18.0, 21.0 and 25.0 meters are 2.17%, 3.97%, 5.67% and 10%, respectively.

Also, for the horizontal undrained (Case 3) and horizontally drained embankment dams with anisotropic material, the location of the phreatic line is determined and shown in Figure 6.

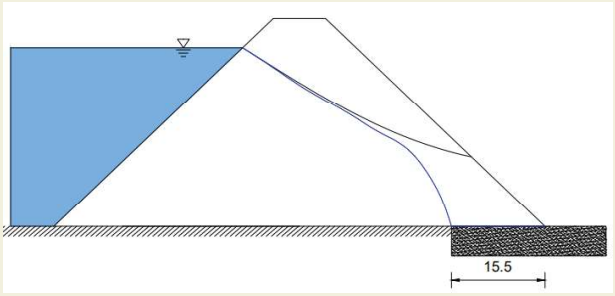

Figure 7. Phreatic line of the dam

It can be seen in Figure 7, that the seepage line in dams with horizontal drainage is inside the dam body and it cannot cause any possible damage to the downstream region due to piping. This result demonstrates the importance of using the horizontal drains to control the position of the phreatic line for the stability of earthen dams.

Example 4

In this example, the seepage amount has been calculated for the rectangular dam body with water in the downstream region. The geometric and material properties are given in Figure 8. The results obtained in this section are given in Table 5 and compared with those of Parsi and Daneshm [33] and Parsi [34]. They [33, 34] examine the position of the phreatic surface, which is unknown at the beginning of the solution and must be determined in an iterative process, with different theories.

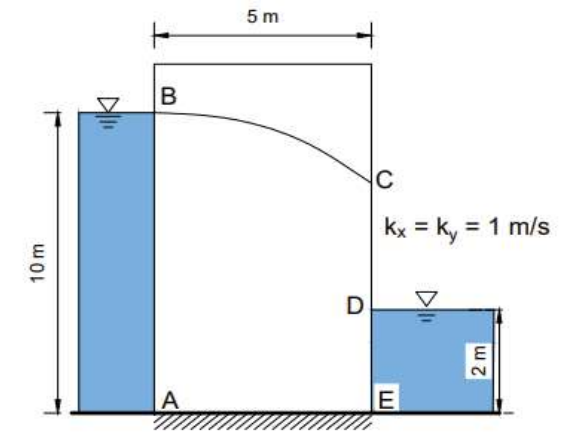

Figure 8. Geometry and material properties of the dam

In comparison with the current literature, it is seen that the seepage results given in Table 5 are in excellent agreement.

Table 5. Seepage rate per unit width of the dam ($m^3/s/m$)

Parsi and Daneshm [33]	Parsi [34]	Present Study
9.60	9.64	9.61

Example 5

The value of the seepage discharge through the foundation of the dam is calculated and given in Table 6. The geometric properties of the dam are illustrated in Figure 9. It has been seen that the results of the suggested approach are quite close to the result found in the literature.

Table 6. Seepage rate per unit width of the dam foundation ($m^3/s/m$)

Mansuri [35]	Present Study
$7.7015x\ 10^{-5}$	$7.6502x\ 10^{-5}$

While performing the calculations, the seepage region has been divided into 1250 finite element elements (3901 nodes). The hydraulic head and pressure values of the dam are calculated and shown in Table 7 at the points of the foundation ends and the middle (1,50,1200,1250) and the two elements (1221,1231) located under the body downstream and upstream region.

Several studies are carried out to reduce high uplift forces which is a result of water seeping when the foundation

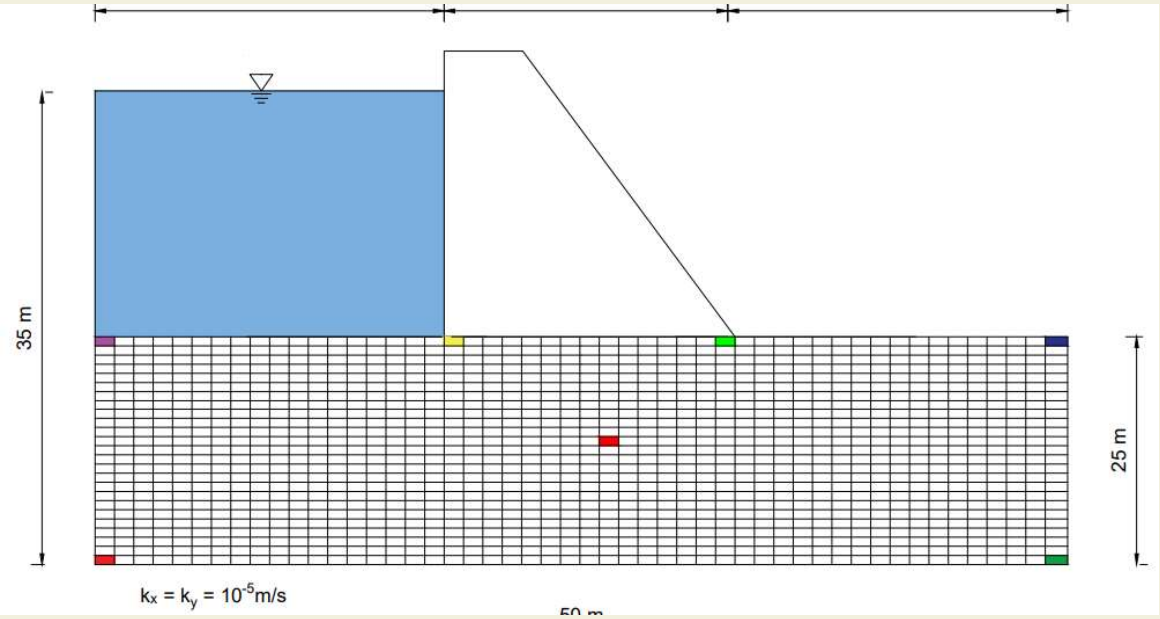

Figure 9. Geometry and material properties of the dam

Table 7. Hydraulic head and pressure load values of the dam

NODE	X (m)	Y (m)	HYDRAULIC HEAD (m)	PRESSURE HEAD (m)	NODE	X (m)	Y (m)	HYDRAULIC HEAD (m)	PRESSURE HEAD (m)
1	0.0	0.0	32.412	32.412	3690	20.5	24	33.279	9.279
2	0.5	0.0	32.410	32.410	3691	21.0	24	32.793	8.793
3	1.0	0.0	32.407	32.407	3709	30.0	24	26.359	2.359
99	49.0	0.0	27.520	27.520	3710	30.5	24	26.026	2.026
100	49.5	0.0	27.517	27.517	3711	31.0	24	25.847	1.847
101	50.0	0.0	27.516	27.516	3747	49.0	24	25.169	1.169
102	0.0	0.5	32.413	31.913	3748	49.5	24	25.169	1.169
103	1.0	0.5	32.408	31.908	3749	50.0	24	25.169	1.169
151	49	0.5	27.519	27.019	3750	0.0	24.5	34.912	10.412
152	50	0.5	27.515	27.015	3751	1.0	24.5	34.912	10.412
153	0.0	1.0	32.416	31.416	3770	20.0	24.5	34.137	9.637
154	0.5	1.0	32.415	31.415	3771	21.0	24.5	32.987	8.487
155	1.0	1.0	32.412	31.412	3780	30.0	24.5	25.853	1.353
251	49.0	1.0	27.516	26.516	3781	31.0	24.5	25.430	0.930
252	49.5	1.0	27.513	26.513	3799	49.0	24.5	25.085	0.585
253	50.0	1.0	27.512	26.512	3800	50.0	24.5	25.084	0.584
1873	24.0	12.0	30.198	18.198	3801	0.0.	25	35.000	10.000
1874	24.5	12.0	30.082	18.082	3802	0.5	25	35.000	10.000
1875	25.0	12.0	29.965	17.965	3803	1.0	25	35.000	10.000
1950	24.0	12.5	30.206	17.706	3841	20.0	25	35.000	10.000
1951	25.0	12.5	29.966	17.466	3842	20.5	25	33.756	8.756
2025	24.0	13.0	30.215	17.215	3843	21.0	25	32.986	7.986
2026	24.5	13.0	30.091	17.091	3861	30.0	25	25.000	0.000
2027	25.0	13.0	29.966	16.966	3862	30.5	25	25.000	0.000
3649	0.0	24.0	34.824	10.824	3863	31.0	25	25.000	0.000
3650	0.5	24.0	34.824	10.824	3899	49.0	25	25.000	0.000
3651	1.0	24.0	34.823	10.823	3900	49.5	25	25.000	0.000
3689	20	24.0	33.625	9.625	3901	50.0	25	25.000	0.000

with high permeability is used. This can pose a danger in hydraulic structures. So, the researchers and engineers try to reduce this undesired situation as much as possible. Thus, the stability of the dam can be ensured.

Example 6

In the last example, the effect of the cutoff wall shown in Figure 10 on the quantity of seepage from the dam foundation has been investigated. An impermeable cutoff wall with depths of 7, 8, 9, 10, 11, and 12 m has been installed at the upstream ends of the dam model. For a cutoff position at the upstream end of the dam, the rate of the seepage discharge from the foundation in the depth of 7- 12 m, the rate of seepage discharge reduction to the base model are 28.97%, 32.43%, 35.72%, 38.85%, 41.84%, and 44.69 % respectively. From Table 8 it can be understood that the cutoff wall has a significant effect on the seepage and the seepage decreases as its length increases.

Table 8. Seepage rate per unit width of dams with cuttoff wall of different depths ($m^3/s/m$)

Cutoff Wall Length, X (m)	Present Study
0	$7.6502x\ 10^{-5}$
7	$5.4336x\ 10^{-5}$
8	$5.1689x\ 10^{-5}$
9	$4.9176x\ 10^{-5}$
10	$4.6780x\ 10^{-5}$
11	$4.4495x\ 10^{-5}$
12	$4.2311x\ 10^{-5}$

3. Conclusion

In this study, seepage analysis of the embankment dam body and its foundation is investigated using the FEM based on Galerkin's approach. By writing a program in Fortran language, hydraulic head, pressure values and quantity of seepage are found at the dam body and foundation points.

It has been concluded that permeability in the x-direction is more effective on the seepage amount in fill dams.

The presence of horizontal drainage is important for the downstream region.

The seepage rate increases as the horizontal drainage length increases.

The cutoff lengthens the seepage length and reduces the permeability seepage rate per unit width.

Acknowledgements

The authors thank the Scientific Research Projects Directorate of Cukurova University for supporting the present study (FBA-2019-12058).

References

[1] Ardıçlıoğlu, M. (1990). Sonlu elemanlar yöntemi ile Aslantaş baraj gövdesinde sızma analizi, Master thesis, Cukurova University, Turkey. (In Turkish)

[2] Keskin, S. B. (2005) Toprak dolgu baraj gövdesindeki ve altındaki sızma olayının incelenmesi, Master thesis, Pamukkale University, Turkey. (In Turkish)

[3] Çilingir, H. (2007) Toprak Dolgu barajların gövdelerindeki sızmaların sonlu elemanlar yöntemi ile incelenmesi: Büyükçekmece barajı uygulaması, Master thesis, Istanbul Technical University, Turkey. (In Turkish)

[4] Fakhari, A., Ghanbari, A. (2013). A Simple method for calculating the seepage from earth dams with clay core. Journal of GeoEngineering, 8, 27-32.

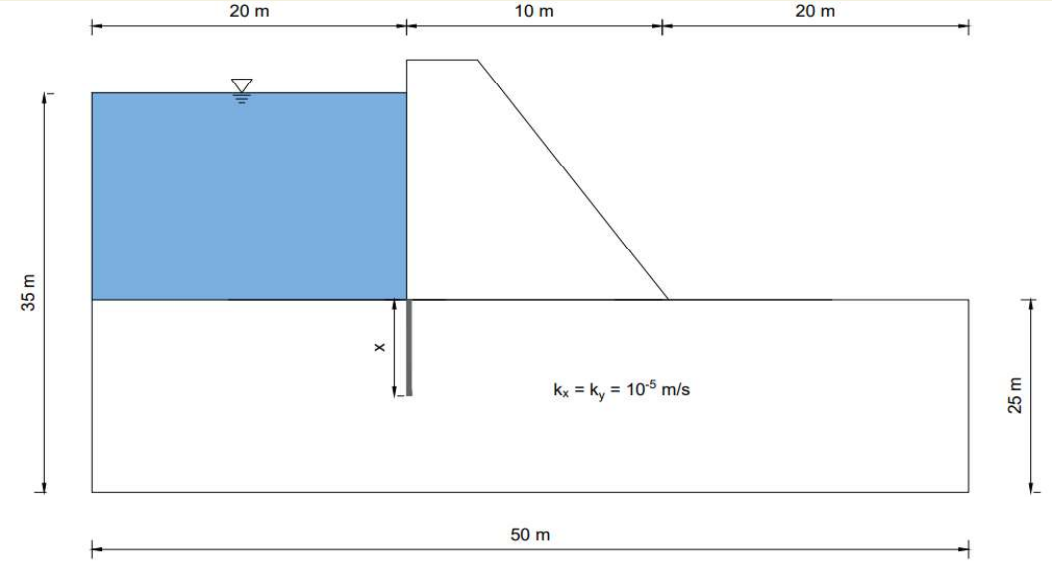

Figure 10. Geometry and material properties of the dam with cutoff wall (Example 6)

[5] Çelik, B. (2014)Aydın İkizdere barajı sonlu elemanlar yöntemi ile sızma analizi, Master thesis, Gazi University. (In Turkish)

[6] Sağlıca, O. (2013) Dolgu baraj gövdelerinde sızma analizi, Master thesis, Gazi University, Turkey. (In Turkish)

[7] Darbandi, M., Torabi, S., Saadat, M., Daghighi, Y., Jarrahbashi D., (2007). A Moving-Mesh finite-volume method to solve free-surface seepage problem in arbitrary geometries. Int. J. Numer. Anal. Meth. Geomech, 31 1609–1629.

[8] Rafıezadeh, K., Ataıe-ashtiani, B. (2013). Seepage analysis in multi-domain general anisotropic media by three-dimensional boundary elements. Engineering Analysis with Boundary Elements, 37, 527–541.

[9] Ourıa, A., Toufıgh, M.M., (2009). Application of nelder-mead simplex method for unconfined seepage problems. Applied Mathematical Modelling, 33, 3589–3598.

[10] El-Jumaıly, K.K., Al-bakry, J.M.H, (2013). Seepage analysis through and under hydraulic structures applying finite volume method. Eng. Tech.J., 9, 1719-1731.

[11] Mesci, S.B. (2006). Dolgu baraj gövdelerindeki sızmaların ve freatik hattın incelenmesi: seferihisar barajı uygulaması, Master thesis, Istanbul Technical University, Turkey. (In Turkish)

[12] Çakır, H.U. (2011). Yeraltısuyu akımlarının modellenmesinde kollokasyon metodu, Master thesis, Dokuz Eylul University, Turkey. (In Turkish)

[13] Quanshu, L., Jianjun, L., (2010). Numerical analysis of the seepage field in core-dam Iı quanshu, LIU Jianjun 492-499. https://www.researchgate.net/publication/267976261_Numerical_Analysis_of_the_Seepage_Field_in_Core-Dam.

[14] Mansuri, B., Salmasi, F., (2013). Effect of horizontal drain length and cutoff wall on seepage and uplift pressure in heterogeneous earth dam with numerical simulation. Journal of Civil Engineering and Urbanism, 3(3), 114-121.

[15] Sakhmarsi, A.A., Akhbari, H., Naeimi, S.P., Kiapey, A. (2014). The effect of the cutoff wall conditions on the seepage characteristics of homogeneous earth-fill dams using SEEP/W. WALIA journal, 30(S2), 176-182.

[16] Yuan, S., Zhong, H., (2016). Three dimensional analysis of unconfined seepage in earth dams by the weak form quadrature element method. Journal of Hydrology, 533, 403–411.

[17] Zhang, W., Dai, B., Liu, Z., Zhou, C. (2017). Unconfined seepage analysis using moving kriging mesh-free method with Monte Carlo integration. Transport in Porous Media, 116(1), 163–180.

[18] Khassaf, S.I., Madhloom A.M.,(2017). Efect of impervious core on seepage through zoned earth dam (case study: Khassa Chai dam). Int J Sci Eng Res.,8(2),1053–1064.

[19] Zewdu, A., (2019), Seepage and slope stability analysis of earthen dam: a case study of Koga Dam. Ethiopia, WNOFNS, 26, 191-217.

[20] Taghvaei, P., Mousavi, S.F., Shahnazari, A., Karami, H., Shoshpash, I. (2014). Experimental and numerical modeling of nano-clay efect on seepage rate in earth dams. Int J Geosynth Ground Eng., 5(1),1.

[21] Doaa, A., El Molla, T. (2019), Seepage through homogeneous earth dams provided with a vertical sheet pile and formed on impervious foundation. Ain Shams Eng J., 10(3), 529–539.

[22] Sanayei, H.R.Z., Javdanian, H. (2020). Assessment of steady-state seepage through dams with nonsymmetric boundary conditions: analytical approach, Environ Monit Assess, 192: 3.

[23] Salmasi, F., Nouri, M., Abraham J.(2020). Upstream cutoff and downstream filters to control of seepage in dams. Water Resources Management, 34, 4271–4288.

[24] Kheiri, G., Javdanian, H., Shams, G. (2020). A numerical modeling study on the seepage under embankment dams, Modeling Earth Systems and Environment, 6, 1075–1087.

[25] Doorı, S., Noorı, A. R. (2021). Finite element approach for the bending analysis of castellated steel beams with various web openings, ALKÜ Fen Bilimleri Dergisi, 3 (2), 38-49.

[26] Chai, Y., Li, W., Liu, Z., (2022). Analysis of transient wave propagation dynamics using the enriched finite element method with interpolation cover functions, Applied Mathematics and Computation, 412, 126564.

[27] Pinnola, P.F., Vaccaro, M.S.,Barretta, R., Sciarra, F.M., (2022). Finite element method for stress-driven nonlocal beams, Engineering Analysis with Boundary Elements,134, 1,22-34.

[28] Ma, S., Chen, M., Skelton, R.E. (2022).Tensegrity system dynamics based on finite element method, Composite Structures, 280, 114838

[29] Ming, H.,Yun, L.L., Shuai, Z., Zhang, A.M. (2022). Research on characteristics of deep-sea implosion based on Eulerian finite element method, Ocean Engineering, 110270.

[30] Harr, A. E. (1962). Groundwater and Seepage, McGRaw-Hill Book Company, 1962.

[31] Jie, Y.-x., Liu, L., Xu, W., Li, G., (2013). Application of NEM in seepage analysis with a free surface. Mathematics and Computers in Simulation, 89, 23–37.

[32] Noori, A.R., Aslan, T.A., Temel, B. (2019). Dairesel plakların sonlu elemanlar yöntemi ile laplace uzayında dinamik analizi. Niğde Ömer Halisdemir Üniversitesi Mühendislik Bilimleri Dergisi, 8(1), 193-205. (In Turkish)

[33] Parsi, M. J. K., Daneshm, F., (2012). Unconfined seepage analysis in earth dams using smoothed fixed grid finite element method. Int. J. Numer. Anal. Methods Geomech., 36, 780–797.

[34] Parsi, M.J.K., (2019). Isogeometric analysis in solution of unconfined seepage problems. Computers and Mathematics with Applications, 78, 66–80.

[35] Mansuri, B., Salmasi, F., Oghati. B., (2014). Effect of location and angle of cutoff wall on uplift pressure in diversion dam, Geotech Geol Eng., 32,1165–1173.

EUROPEAN MECHANICAL SCIENCE
e-ISSN: 2587-1110

RESEARCH ARTICLE

Web based remote agricultural control and consultancy application: An early diagnostic warning system

Fatih Çağatay Baz[1*], Emrah Denizer[1]

[1] Management Information Systems, Osmaniye Korkut Ata University, Turkey

Orcid: F.Ç. Baz (0000-0002-6398-9851), E. Denizer (0000-0002-5865-079X)

Abstract: In this study, the Web-Based Remote Agricultural Struggle and Counseling Application, which was developed within the Agriculture 4.0 approach for the spread of agricultural technologies and the use of technology in agriculture, has been discussed with the technical personnel who are experts in the field, and what improvements should be made regarding the application. In the study, literature review was made, agricultural consultancy, smart agriculture and the use of digital technologies in agriculture were discussed. The Web Based Remote Agricultural Control and Consultancy Application designed in this study was developed with the Python programming language. The development and operation of the application are presented in the form of screenshots. In the research, user opinions of the application were collected through a form consisting of 4 questions to measure demographic information, a qualitative question consisting of 7 main titles, and 28 sub-titles to measure the opinions of technical personnel about the application, which was prepared by taking expert opinions. The data obtained from the research users were analyzed with the Nvivo 12 program. As a result of the analysis, it was concluded that the development of web-based agricultural control, consultancy application for technical personnel is appropriate, the interface design should be improved, and it will contribute positively to the dissemination of technology use in agriculture.

Keywords: Agriculture 4.0, smart farm, web-based consultancy, information systems

1. Introduction

In our age, it has become inevitable to show itself in the fields of agricultural education, extension and production with the rapidly developing scientific, and technological opportunities. As a result of the progress and developments in internet technologies, web-based agricultural services have gained widespread popularity through the public and private sectors. The share of the developments in the agricultural sector in the delivery of the developments in the agricultural sector to the public, and the farmers without worrying about time, space is quite high, and its importance is increasing day by day. The data formed as a result of the intensive use of information technologies in every field has been transformed into information thanks to the advancing technological opportunities, and the agricultural sector has taken its share of this information.

It is a fact that more production will be needed in the near future. In order to provide this production, it is necessary to increase the efficiency obtained from the unit area [1]. With the introduction of digital agricultural software, it is necessary to ensure the effective use of irrigation water, soil, and agricultural input components. Thanks to software that can calculate evaporation by processing instant climate, soil and product data, wireless signals sent to the manufacturer's mobile phone or automation system and appropriate sensors, it is calculated that agriculture can be done with 80% less use of water used in agriculture [2]

Digital soil maps, remote sensing, and GPS guidance are critical tools for modern farmers. Big data for precision agriculture increase yield and productivity. These high-tech tools often benefit large farms that can invest heavily in technology [3]. Especially Big Data and the Internet of Things (IoT) are the ways to minimize the dependence on climatic conditions in crop cultivation. Thus, minimizing the impact of the human factor will allow GPS tracking, digital platforms where agricultural products are marketed, and artificial intelligence to come into play [4]. Minimizing resource costs in the agricultural production process will increase the efficiency and competitiveness of agricultural production, and sustainable development [5].

Active use of digital technologies in agriculture creates a new segment of agriculture called "digital agriculture". Digital agriculture is the technological foundation of

* Corresponding author.
Email: fatihcagataybaz@osmaniye.edu.tr

European Mechanical Science (2022), 6(2): 152-160
https://doi.org/10.26701/ems.1111182
Received: April 29, 2022 — Accepted: June 15, 2022

the agriculture of the future. Digital agriculture enables the creation of high-yield agriculture that can meet the increasing needs of the population with more economical use of limited resources. Effective control and use of the expenditure of funds allocated for the implementation of the production process, system control of the production process continues from the beginning of production to the delivery consumer.

It ensures that digitalized agricultural producers are supported in terms of production processes, that women and young people are equipped with the right information, and that agricultural inputs are made at rates that support sustainable production. In this way, maximum production and income are obtained, and as a result of the correct and effective use of resources by improving production methods in agriculture, more production is realized with less input [6,7,8]. Components of smart agriculture; includes basic systems such as global positioning systems, geographic, information systems, variable rate input application and remote sensing [9]. Information systems and portals developed for distance education have opened up new areas with the development of technology, making it necessary to design programs that will meet the different needs, and demands of people [6,10,11]. One of these needs is a web-based agricultural consultancy, and early diagnosis warning system in the field of agriculture. In this sense, there are many studies conducted in the field [12,13,14].

The aim of this research is to minimize the time, space constraints in accessing the information and consultancy services required in agricultural production with the help of the portal developed by using internet technologies, and to make this access permanent. Thanks to the developed web application, it is to add a different dimension to the technical support that all stakeholders involved in agricultural production need in the face of negative situations in production activities. With the application, it is aimed to easily monitor, control the steps that farmers, and agricultural consultants need to follow throughout the agricultural production process. It is aimed to follow the recommended irrigation, fertilization, and spraying prescriptions related to production by means of field photographs uploaded to the system at regular intervals. It is thought that following the recommended recipe throughout the production process will provide convenience for both the producer and the agricultural consultant. Thus, after a planned, programmed, well-controlled production period, a process that will be profitable for the producer, and the consumer with minimum loss, and maximum gain will be completed.

With the Internet of Things, sensors, autonomous devices, wireless communication, cloud computing, big data analytics, etc. Agricultural production values measured can provide greater productivity gains, and more information while reducing costs, thanks to the combination of various technologies such as Combined with machine learning algorithms, this information can help make better decisions and improve production-related product quality [15]. In this sense, techno-city and incubation centers of universities can transform scientific knowledge into initiatives, and create an ecosystem focused on digital agriculture [16].

The interest in smart agriculture, web-based remote support platforms is increasing day by day, and it is important for public and private sector institutions to use these platforms outside of traditional agricultural practices. It is important that such practices become widespread, especially in disadvantaged segments where access to agricultural consultancy is lacking. In the researches, the application of the opportunities created with Industry 4.0 in the agricultural field also significantly reduces the agricultural input costs, increases the profitability rate significantly, and provides significant convenience in accessing quality, clean and safe food. In this sense, the study is important.

The system used in this research was applied to 10 technical personnel working in Adana Provincial Directorate of Agriculture in Turkey. The server has been adjusted so that the system can serve 10 technical personnel. The data and evaluations obtained as a result of the survey carried out in the research are limited to the personnel who have agricultural consultancy authority.

2. Materials and Methods

An application has been developed for use in agriculture in the study. The developed application is designed to solve the early diagnosis problems of the producers in agriculture and to meet the needs of the personnel working in this field. With the designed application, interviews were held with technical personnel who are experts in their fields, about the widespread use of agricultural technologies and technology in agriculture within the Agriculture 4.0 approach. It has been revealed what improvements should be made regarding the application.

Designing the Application: The application, which consists of two different interfaces, namely Farmer and Technical Personnel, has been developed on the web platform. The reason for choosing the web platform for the development of the application is to enable users to access the application independent of time and place. In addition, during the design phase of the application, users can use phones, tablets, etc. In order to provide access from different devices, responsive design has been taken into account, which allows the web page to be shaped according to the device entered when accessed from different devices. Thus, users will be able to access the application from any device.

During the development of the application, Software Life Cycle steps were followed. In addition, a survey study was conducted for user testing in this research. The working

group of the research consists of 10 technical personnel (engineers, technicians, etc.) working in Adana Provincial Directorate of Agriculture and Forestry.

The developed application is designed according to the work flow diagrams below. Screenshots of the application developed for the study are presented below.

Algorithm Code (For Manufacturers):

1- Beginning
2- Please Upload Photo with Location(message)
3- Photograph
4- Is the Photo Uploaded Correctly?
5- Step 6 if Installed Properly
If not installed, repeat step 3
6- Please Enter Note? (Message)
7- Finish

Algorithm Code (For Technical Staff):

1- Beginning
2- Photograph
3- Is the declared product and the product in the photo the same?
4- If "No", step 6,
If "Yes" continue from step 5
5- Your prescription has been created? (Message)
6- Finish

Application: Technical personnel open the photo and message from the manufacturer, check the location (parcel) of the uploaded photos, and confirm whether the declared product is the same as the disease or harmful product. If the product in the parcel and the declared product are the same, the necessary information, namely the recipe, is sent to the producer via the system via message. If the products do not match, the manufacturer is asked to either correct the statement or upload the correct photo of the product in the parcel.

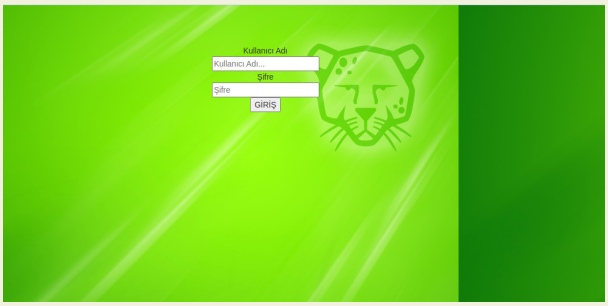

Figure 1. Login page for technical staff and manufacturers.

The login page consists of username and password fields and a login button. The login page is shown in Figure 1.

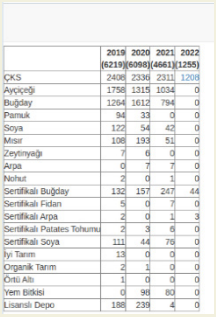

	2019 (6219)	2020 (6098)	2021 (4661)	2022 (1255)
ÇKS	2408	2336	2311	1208
Ayçiçeği	1758	1315	1034	0
Buğday	1264	1612	794	0
Pamuk	94	33	0	0
Soya	122	54	42	0
Mısır	108	193	51	0
Zeytinyağı	7	6	0	0
Arpa	0	7	7	0
Nohut	2	0	1	0
Sertifikalı Buğday	132	157	247	44
Sertifikalı Fidan	5	0	7	0
Sertifikalı Arpa	2	0	1	3
Sertifikalı Patates Tohumu	2	3	6	0
Sertifikalı Soya	111	44	76	0
İyi Tarım	13	0	0	0
Organik Tarım	2	1	0	0
Örtü Altı	1	0	0	0
Yem Bitkisi	0	98	80	0
Lisanslı Depo	188	239	4	0

Figure 2. Homepage for technical personnel.

Homepage is the page where the navigation menu is located. The home page view is given in Figure 2. The homepage consists of applications, maps and detection menus accessible to technical personnel.

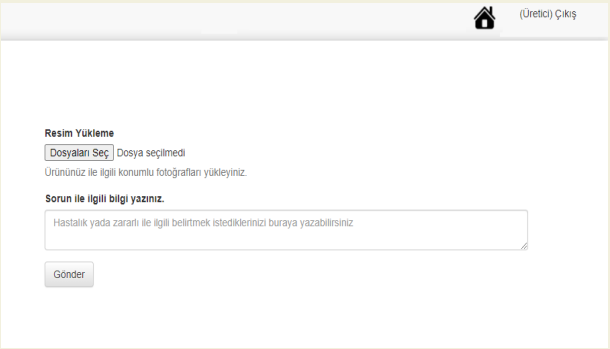

Figure 3. Homepage for manufacturers.

The "Homepage" view that manufacturers can access is given in Figure 3. Producers can upload photos related to the problematic area from the "Picture Upload" section and send their messages about the problem from the "Message" section.

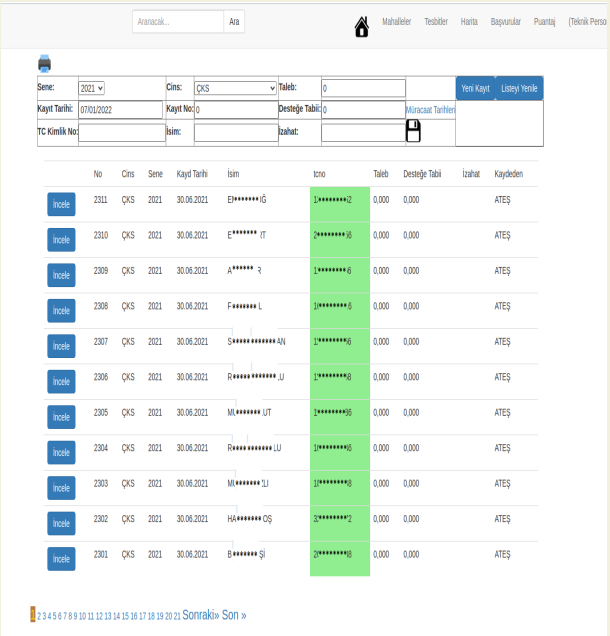

Figure 4. Reference list page.

The "Application List" page is given in Figure 4. The "Application List" page is the page where the applicant manufacturers are listed. This page contains basic information about the manufacturers such as name, identification number and year of application. When the "Review" button is pressed, detailed information about the application is accessed.

Figure 5. Detailed application list page.

The " Detailed Application List" page is given in Figure 5. The "Detailed Application List" page is the page where the applicant manufacturers are listed in detail. This page includes basic information about the manufacturers such as name, identification number and year of application, as well as product type and area information. When the product name is clicked in the "Product/Declaration/Detection" column, the photos related to the product subject to the complaint are accessed.

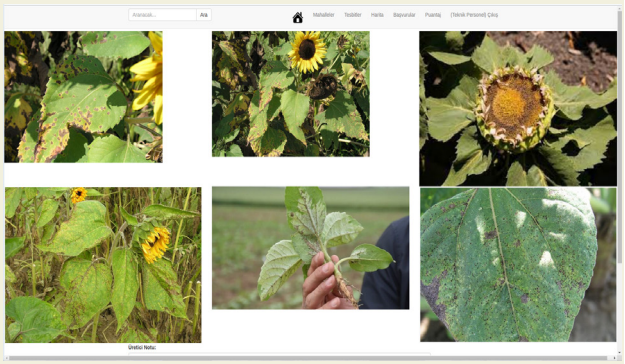

Figure 6. Product review page.

The "Product Review" page is given in Figure 6. The "Product Review" page is the page where the product photos uploaded by the manufacturers to the system are reviewed by the technical staff. By clicking on the positioned photos, necessary examinations are made, and information about the disease or pest is sent to the producers via message. In this example, the producer requests consultancy on sunflower diseases and pests.

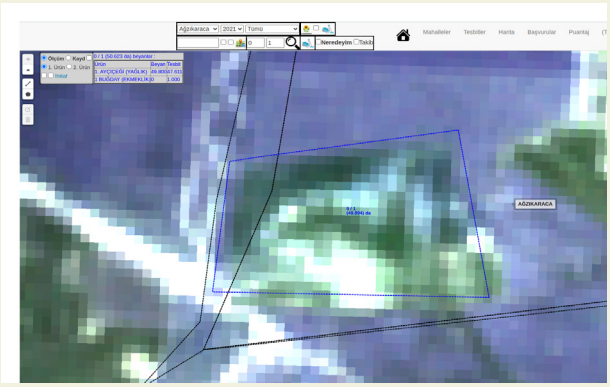

Figure 7. GIS Geographic Information System (GIS).

When you click on any photo, the parcel where the photo was taken and the declaration information about the parcel will appear on the Geographic Information System (GIS). When Figure 7 is examined, it is seen that the parcel where the photograph was taken is the immovable property with the number 0 block 1 parcel numbered in the Adana province İmamoğlu district, Ağzıkaraca Village, and the product planted and declared on the parcel from the map images is sunflower.

After the necessary examinations are made, the prescription that needs to be applied is sent as a message to the mobile phone numbers of the manufacturers registered in the system by the technical personnel.

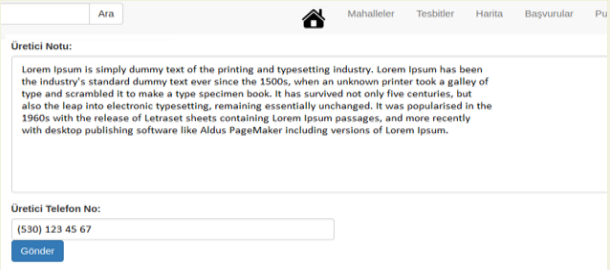

Figure 8. Message to manufacturers

Examples of maps with different dates used in the GIS module are shown in Figure 9, Figure 10, Figure 11, Figure 12, Figure 13, Figure 14, Figure 15 and Figure 16.

Examples of code used in the development of the application are shown in Figure 17, Figure 18, Figure 19, Figure 20, and Figure 21.

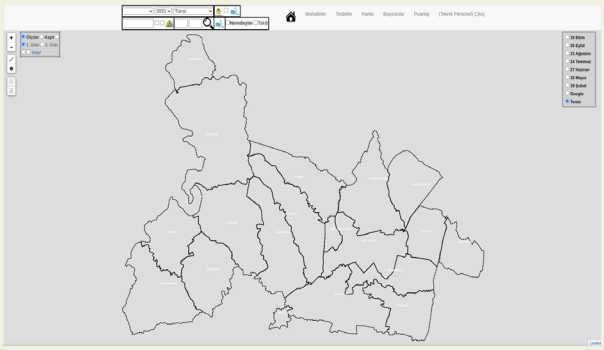

Figure 9. Map showing village boundaries

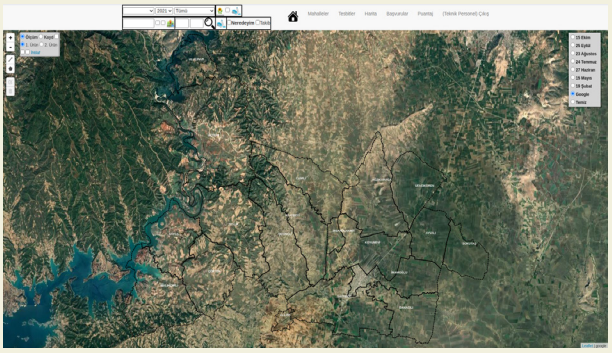

Figure 10. Google map

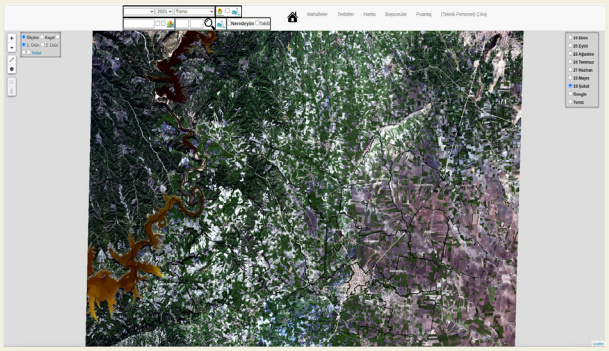

Figure 11. Infrared band image dated 19.02.2021

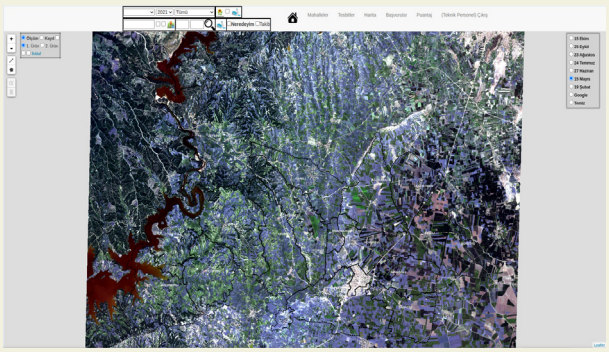

Figure 12. Infrared band image dated 15.05.2021

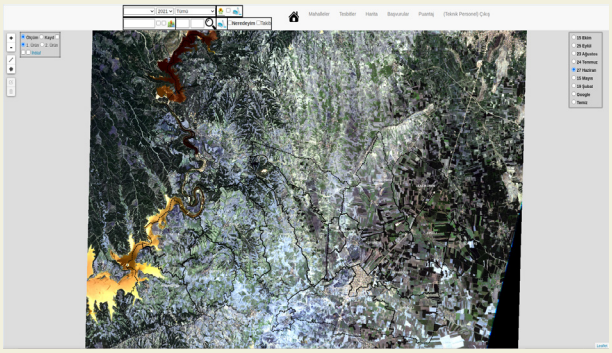

Figure 13. Infrared band image dated 27.06.2021

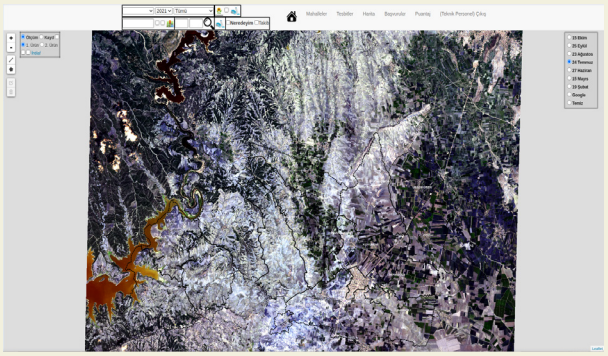

Figure 14. Infrared band image dated 27.07.2021

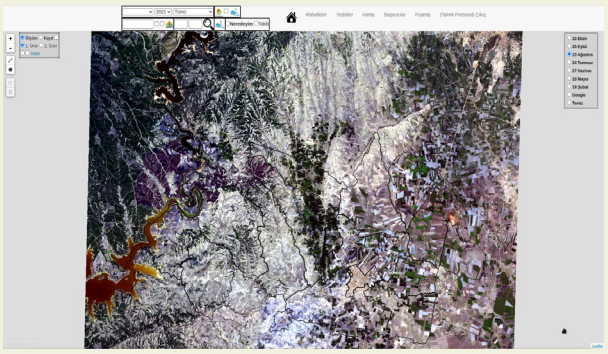

Figure 15. Infrared band image dated 25.09.2021

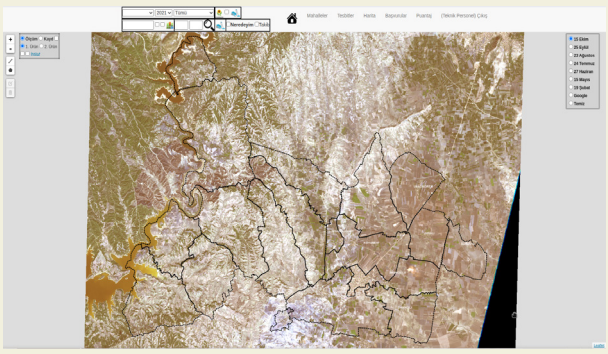

Figure 16. Infrared band image dated 15.10.2021

```
        <img src="/static/resim/goruntuler/ayicegi1.png" width="100%"
            height="100%" class="rounded float-left" alt="Responsive image">
    </div>
    <div class="container col-md-4">
    <div class="container col-md-4">
        <img src="/static/resim/goruntuler/ayicegi3.png" width="100%"
            height="100%" class="rounded float-left" alt="Responsive image">
    </div>
    <div class="container col-md-4">
        <img src="/static/resim/goruntuler/ayicegi4.png" width="100%"
            height="100%" class="rounded float-left" alt="Responsive image">
    </div>
    <div class="container col-md-4">
        <img src="/static/resim/goruntuler/ayicegi5.png" width="100%"
            height="100%" class="rounded float-left" alt="Responsive image">
    </div>
</div>
<form>
    <div class="container">
        <div class="form-row">
            <div class="form-group col-md-10">
                <label for="textarea"> Üretici Notu:</label>
                <textarea rows="10" cols="250" class="form-control" id="textarea"></textarea>
            </div>
        </div>
        <div class="form-row">
            <div class="form-group col-md-5">
                <label for="text">Üretici Telefon No:</label> <input type="text"
                    class="form-control" id="text"></input>
```

Figure 17. HTML codes used to display images

```
                {
            ip='http://78.187.108.183:81/cgi-bin/qgis_mapserv.fcgi';
            mapi="/home/burak/hifz/tesbits.qgs";
            layer=jq('input:radio[name=suret]:checked').val();
            }
        {% else %}
            ip='http://192.168.1.97:8080/geoserver/tesbits/wms';
            if (document.getElementById("id_sene").value!=6)
            {
        ip='http://192.168.1.97:81/cgi-bin/qgis_mapserv.fcgi';
        mapi="/home/burak/hifz/tesbits.qgs";
        layer=jq('input:radio[name=suret]:checked').val();
        }
        {% endif %}

        uydu  = L.tileLayer.wms(ip,{
        layers: layer,
        map: mapi,
        format: 'image/png',
        transparent : true
                },
                {
            buffer:0,
            singleTile:true,
            ratio:1,
            transitionEffect:"resize"
```

Figure 18. Codes with which maps are displayed

```
if sualci:
    sualci=sualci.upper()
    liste=Defter.objects.filter(
        Q(isim__icontains=sualci.upper().strip())|
        Q(tcno__icontains=sualci.strip())|
        Q(kaydno__icontains=sualci.strip())
        #Q(izahat__icontains=sualci)
        ).filter(sene=cri_sene).distinct()

paginator = Paginator(liste, 11) # Show 2 contacts per page
page_liste = paginator.get_page(page)
context = {}
context["netice"]=netice
context["form"]=form
context["liste"] = page_liste
return render(request, 'defter/liste.html', context)
```

Figure 19. Codes where references are listed

Preparation of Research Questions and Collection of Data: Qualitative interview questions were developed by the researcher to measure the views of technical personnel on the practice. These questions, developed by the researcher, were arranged by experts in the field. Experts in the field consist of 6 people who work as faculty members in the field of management information systems. According to the answers from the experts, some of the questions were removed, some of them were corrected, and some of them were changed in the form. The process of collecting the data used in the research was carried out in the form of sending the interview form consisting of demographic and qualitative questions, prepared by the researcher via Google Forms, to the technical personnel and the technical personnel responding to the form. The opinions of the technical personnel regarding the application used in the study were collected. Within the scope of this study, interview forms with ten technical personnel who are experts in their fields were recorded, and the data obtained from the interviews were organized in detail.

```
from GPSPhoto import gpsphoto
# Get the data from image file and return a dictionary
data = gpsphoto.getGPSData('/path/to/image.jpg')
rawData = gpsphoto.getRawData('/path/to/image.jpg')

# Print out just GPS Data of interest
for tag in data.keys():
    print "%s: %s" % (tag, data[tag])

# Print out raw GPS Data for debugging
for tag in rawData.keys():
    print "%s: %s" % (tag, rawData[tag])

# Create a GPSPhoto Object
photo = gpsphoto.GPSPhoto()
photo = gpsphoto.GPSPhoto("/path/to/photo.jpg")

# Create GPSInfo Data Object
info = gpsphoto.GPSInfo((35.104860, -106.628915))
info = gpsphoto.GPSInfo((35.104860, -106.628915), \
          timeStamp='1970:01:01 09:05:05')
info = gpsphoto.GPSInfo((35.104860, -106.628915), \
          alt=10, timeStamp='1970:01:01 09:05:05')

# Modify GPS Data
photo.modGPSData(info, '/path/to/newFile.jpg')

# Strip GPS Data
photo.stripData('/path/to/newFile.jpg')
```

Figure 20. Codes for obtaining location information in photos

```
import requests

hedefNumara=uretici_telNo// SMS Göndermek istediğiniz üreticinin telefon numarası
text=mesaj_kutusu// SMS yollayacağınız mesaj
sunucu=mesaj_sunucusu// SMS yollamak için üye olunan servis

r=requests.post(mesaj_sunucusu,{'phone':hedefNumara,'message':text,'key':'sunucu'} //sunucu'a veri gönderme

if r.json()['success']==True://mesaj hedef numaraya iletildiyse'gönderildi' ekrana yazdır

print('Mesaj Gönderildi')

else:
    print('gönderilemedi') // iletilmediyse 'gönderilemedi' yazdır
```

Figure 21. Codes that send messages to manufacturers

The obtained data were arranged in sets and analyzed. The data of the participants were arranged statistically. The verbal data obtained were processed in the Nvivo 12 program as codes and categories. The coded data were categorized according to the main question titles and detailed according to the sub-questions. Findings regarding the views of the participants on the remote agricultural consultancy web application were revealed by performing the analysis of the coded data.

3. Results

In this study, the data obtained were analyzed, and the findings were analyzed in six parts. The findings are shown in tables with visual support. Within the scope of this study, interview forms with ten technical personnel who are experts in their fields were recorded, and the data obtained from the interviews were organized in detail. Obtained findings and comments are given in tables. While the answers given by the users to the questions were given directly, codes such as User 1 and User 2 were written at

the beginning of the answers in order to be clear by which user the answers were given.

Demographic Findings: The findings obtained from the demographic questions of gender, age, marital status, education level, total length of service obtained as a result of the research are given below.

Gender: The distribution of the academic staff participating in the research by gender was analyzed, and the results are shown in Table 1.

Table 1. Distribution of participants by gender

User Gender	n	f
Female	3	%30
Male	7	%70
Total	**10**	**100**

As a result of the analysis, it was concluded that 3 (30%) of the participants were female and 7 (70%) were male.

Age: The age distribution of the participants participating in the study was analyzed, and the results are shown in Table 2.

Table 2. Distribution of participants by age

Age Ranges (Years)	n	f
Between 25-35	3	%30
Between 36-45	2	%20
Between 46-55	3	%30
Between 56-65	2	%20
Total	**10**	**100**

As a result of the analysis, 3 (30%) of the participants were between the ages of 25-35, 2 (20%) were between the ages of 36-45, 3 (30%) were between the ages of 46-55, and 2 of them were between the ages of 56-65.

Educational Status: The distribution of the participants participating in the study according to their educational status was analyzed, and the results are shown in Table 3.

Table 3. Distribution of participants by educational status

User Education Status	n	f
Associate degree graduate	1	%10
Bachelor' s degree	7	%70
Post Graduate	2	%20
Total	10	100

As a result of the analysis, it was concluded that 1 (10%) of the participants had an associate degree, 2 (20%) had a post degree, and 7 (70%) had a bachelor' s degree.

Professional Experience: The distribution of the participants in the study according to their total professional experience period was analyzed and the results are given in Table 4.

Table 4. Distribution of participants by length of service

Professional Experience (Years)	n	f
Between 5-15	5	%50
Between 16-25	1	%10
Between 26-35	2	%20
Between 36-45	2	%20
Total	10	100

In the distribution of the participants in the study according to their total professional working period, it was concluded that 1 of them was between 16-25 years, 2 of them were between 26-35 years, 2 of them were between 36-45 years, 5 of them were between 5-15 years.

Findings Regarding Themes, Categories and Codes of the Research: Codes were created from the data created from the answers received from the participants, and categories were created based on the codes. In the preliminary analysis of the data obtained from the interviews, seven basic categories were created in accordance with the interview questions.

When the answers given to the first category "Interface" were examined, the users stated that the interface design of the application was user-friendly, but they also stated that the color variety of the design should be increased, more agricultural themes should be included, and warning texts about page transitions should be included. They also stated that visuality would affect their working performance.

When the answers given to the second category, "Usability on Different Devices" examined, users state that the application can be used on different devices and operating systems without installation, that the platform-independent nature of the application is a great advantage. They stated that this has been exceeded.

When the answers are given to the third category, "Content Sufficiency" are examined, the users informed that the application should be enriched in terms of content, that the visual elements should be related to plant production, that the texts should be of changeable size, etc. They stated that the content should be reviewed with such criticisms.

When the answers are given to the fourth category "Technical Competence" are examined, the users say that when the application is examined from a technical point of view, the application performs its function in terms of the complete operation of the menus and buttons, the resolution time of the errors, the ease of installation, resolution, sound, and other technical features. The system team is open to feedback, it needs improvement in resolution, it is easy to enter the application because it does not require installation, audio warnings should be added to the sys-

tem, etc. They stated that the system should be strengthened technically with such criticisms.

When the answers are given to the fifth category "Guidance of Users" were examined, the users stated that the application may be sufficient for the technical personnel in terms of guidance, that the farmers might have difficulties, and that the system should be promoted with preliminary information or training, especially for the farmers.

When the answers are given to the sixth category "Openness to Development" are examined, the users stated that the application is suitable for openness to development, it is suitable for software additions when necessary, it is suitable for increasing the number of users, it can adapt to current conditions, and it is appropriate to increase the system capacity with additional hardware support.

4. Discussion

Within the scope of this study, a Web-based interactive Agricultural Consulting Site was designed in the context of Remote Sensing, Geographic Information Systems (GIS), and Precision Agriculture Applications by synthesizing the traditional Agricultural Consulting and Agriculture 4.0 approaches in the literature. In addition, GIS controls included in the module providing consultancy services and audits for agricultural planting determinations will also be provided.

Agriculture 4.0 can combine various applications to meet different needs. Smart agriculture mostly uses internet technology. Various sensors placed on the equipment or in the field provide data to a platform (cloud-based) that allows the creation of an information system for users (agrisupply specialists, farmers, consultants, researchers, etc.). In this sense, sensors embedded in machines that use artificial intelligence to detect weeds to be targeted for local destruction can be given as an example.

It is aimed to evaluate the design prepared in the research by the farmers and technical personnel. For this purpose, questionnaires and qualitative interviews were conducted with the participants.

In the study, the views of 10 technical personnel working in Adana Provincial Directorate of Agriculture and Forestry in Turkey on web-based remote agricultural struggle and consultancy application design were measured by qualitative data analysis method. Demographic findings and the findings obtained from the answers to the questions directed to the technical personnel are included, and suggestions are presented for these findings.

As a result of the study, it was realized that the system that was tried to be developed was functional, but that appropriate visuals and themes should be included in the design phase. In addition, it has been concluded that the web agricultural consultancy application to be designed should have an explanatory content for users and beneficiaries, serve with a user-friendly interface, and there are deficiencies in in-app guidance and these should be eliminated. Another result that emerged from the data analysis was that the technical personnel and manufacturers, who will be included in the system for the first time, can use the application more efficiently after certain promotional activities.

In data analysis, it is stated that visual themes will affect the working efficiency, so it is necessary to use colorful and eye-catching themes that do not tire the eyes; however, it was understood in the analysis of user responses that attention should be paid to its compatibility with agricultural elements. When the answers about the use of the application on different mobile (tablet, smart phone) and fixed devices (pc, laptop) or different operating systems are analyzed, it is seen that the users do not have difficulty in accessing and using the application, the system is compatible with different devices and operating systems, and therefore the developed it has been understood that the use of the system by manufacturers, and technical personnel will easily become widespread.

In the content analysis of the user responses on the technical competence and openness to development of the system, the fact that the system does not require installation from a technical point of view is an important feature, but it has deficiencies in terms of sound, image and menu layouts; It has been concluded that there is no limitation in the number of users, that the adaptation to new technologies can be achieved easily by increasing the hardware capacity, thus making it available for use at the national and international level.

The use of information and communication technologies in digital agriculture should be expanded. Sustainable financing resources should be found in the supply and use of telephone, computer, internet, and other broadcasting tools. It should not be overlooked that the consultants who are trained and encouraged in the use of information technologies in broadcasting will contribute to the formation of an information society in rural areas.

5. Conclusion

It can be suggested that future research should be carried out in a way that covers the wider research population and sample. It may be suggested to develop systems that will enable the provision of agricultural consultancy services through artificial intelligence-supported applications, supporting the digitalization approach in smart agriculture and agriculture. In future studies, it is recommended that researchers from the field of surveying engineering work together while developing web-based remote agricultural applications.

References

[1] Arıkan, H. (2019). İha ile tarımda sürdürülebilirlik ve hassas

uygulamaları ile ayçiçeği hassas gübreleme. M.Sc. Thesis, İstanbul Technical University Institute of Informatics, Turkey.

[2] Oğuz, İ. (2021). Softtech Teknoloji Raporu 2021. Available online with updates at https://softtech.com.tr/2021-softtech-teknoloji-raporu/

[3] Deichmann, U., A. Goyal., D. Mishra. (2016). Will digital technologies transform agriculture in developing countries? Policy Research Working Paper. 7669-22.

[4] Ogorodnikov, E., G. Zaloznaya, J. Singaeva, A. Bart., E. Dmitrieva. (2020). Digital technologies in the agricultural sector of the Russian Federation. E3S Web of Conferences. 175:1-10.

[5] Vorotnikov, I. L., N. V. Ukolava, S. V. Monakhov, J. A. Shikhanova., V. V. Neyfeld. (2020). Economic aspects of the development of the "Digital Agriculture" system. Scientific Papers Series Management, Economic Engineering in Agriculture and Rural Development. 20:633-637.

[6] Boyacı, M., Ö. Yıldız. (2010). Tarım danışmanlarının bilişim ve iletişim teknolojilerini kullanma eğilimleri. Türkiye IX. Tarım Ekonomisi Kongresi. 580-587.

[7] Erdem, İ. (2017). Endüstri 4.0 ve tarım 4.0 çerçevesinde Türkiye ekonomisinin büyümesinde imalat sanayi ve tarım sektörünün geleceği. M.Sc. Thesis, Nuh Naci Yazgan University Institute of Social Science, Turkey.

[8] Tarım Kredi Kooperatifleri. (2020). Tarım için dijital çözüm. Available online with updates at https://www.tarimkredi.org.tr/gundem/blog/tarim-icin-dijital-cozum

[9] Akıllı Tarım Platformu. (2019). Türkiye'de akıllı tarımın mevcut durum raporu. Available online with updates at http://www.akillitarim.org/tr/

[10] Çakmak, E. (2010). Tarımsal yayımı geliştirme projesi (targel) kapsamında tarım danışmanlığı sisteminin inceleme ve değerlendirilmesi: Tokat ili örneği. M.Sc. Thesis, Gaziosmanpaşa University Institute of Science, Turkey.

[11] Özçatalbaş, O., D. Bostan-Budak, İ. Boz., B. Karaturhan. (2010). Türkiye'de tarım danışmanlığı sisteminin geliştirilmesine yönelik önlemler. Ziraat Mühendisliği Teknik Kongre, Turkey. 2: 1-1

[12] Artık, A. (2012). Paydaş görüşlerinden hareketle Adana ilinde serbest tarım danışmanlığı sisteminin değerlendirilmesi. M.Sc. Thesis, Çukurova University Institute of Science, Turkey.

[13] Kara, F. (2012). Arazi toplulaştırma çalışmalarında yapay zekâ uygulamalarının kullanım olanakları: Amasya ili Gümüşhacıköy ilçesi, Keçiköy beldesi uygulaması. M.Sc. Thesis, Ondokuz Mayıs University Institute of Science, Turkey.

[14] Hayran, S., A. Gül. (2018). Mersin ilinde çiftçilerin tarımsal kredi kullanım kararlarını etkileyen faktörler. Journal of Iğdır University Natural and Applied Sciences. 8:271-277.

[15] Suárez-Campione, M. (2018). Analysis and possible improvements of the smarteye iot solution. M.Sc. Thesis, Universidad Politécnica De Madrid, Escuela Técnica Superior de Ingeniería de Sistemas Informáticos, Spain.

[16] Özdoğan, B., A. Gacar., H. Aktaş. (2017). Digital agriculture practices in the context of agriculture 4.0. Journal of Economics, Finance and Accounting. 4:184-191.